# Description of the intrinsic spin Hall effect via Korringa-Kohn-Rostoker density functional theory

---

Beschreibung des intrinsischen Spin-Hall-Effektes durch die Korringa-Kohn-Rostoker Dichtefunktionaltheorie

DISSERTATION

submitted for the degree of

Doctor rerum naturalium
Doktor der Naturwissenschaften

JUSTUS-LIEBIG-UNIVERSITAET GIESSEN
FACHBEREICH 07 - MATHEMATIK UND INFORMATIK, PHYSIK, GEOGRAPHIE

*submitted by:*
M. Sc. Alexander FABIAN

*Supervisor and First Reviewer:*
Prof. Dr. Christian HEILIGER
*Second Reviewer:*
Prof. Dr. Peter J. KLAR

November 2022

# Contents

古池や
蛙飛び込む
水の音


— 松尾芭蕉

# 1. Preface

## 1.1. Abstract

The first part of this thesis deals with the ab initio description of the spin Hall effect in the full-relativistic Korringa-Kohn-Rostoker (FR-KKR) density functional theory (DFT). A new approach to calculate the magnetization accumulation within the full quantum mechanical Keldysh formalism is compared to a semiclassical Boltzmann approach. Both methods rely on the same underlying FR-KKR framework. The comparison focuses on the odd-under-spatial-magnetization-reversal part of the surface magnetization accumulation that solely stems from the band structure properties at the Fermi surface. The comparison shows that both methods yield the same trend for a series of metals with a significant influence of spin-orbit coupling rendering the new Keldysh method a valid and credible candidate for the description of the surface accumulation driven by the spin Hall effect. Contrary to most theoretical approaches, which calculate the bulk property of spin conductivity, the thin-film nature and surface influences are considered here, making direct contact with experiments. When compared to a series of values obtained experimentally, both methods reproduce the trend for the spin Hall angle.

The second part of this thesis deals with interpreting the self-energy in the Büttiker scattering formalism (virtual terminal approach) established in the KKR. The relation between the self-energy $\Sigma$ and the relaxation time $\tau$ used in semiclassical approaches is studied. Understanding this relation plays an important role when comparing the results of the Keldysh formalism with virtual terminal scattering to the Boltzmann scattering description. In the *constant relaxation time approximation* (CRTA), the thermopower is independent of the relaxation time in the Boltzmann approach. This independence is valid for free electrons and Cu in the low scattering regime but fails for Pd completely. This failure is attributed to the complexity of the Fermi surface of Pd. Further, a sufficient resolution for the occurring scattering events is necessary for the virtual terminal approach to work. Based on these findings, the scalability of the approach is discussed as the introduction of scattering could make it possible to consider spin relaxation effects for the spin Hall effect.

The results of this cumulative thesis are published in Phys. Rev. B **104**, 054402, (2021) and Phys. Rev. B **105**, 165106, (2022).

## 1.2. Zusammenfassung

Der erste Teil dieser Thesis behandelt die Beschreibung des Spin-Hall-Effektes im Rahmen der voll relativistischen Erweiterung der Korringa-Kohn-Rostoker Dichtefunktionaltheorie. Ein neuer Ansatz um die Magnetisierungsakkumulation innerhalb des quantenmechanischen Keldysh-Formalismus zu berechnen wird mit einem semiklassischen Boltzmann-Ansatz verglichen. Beide Methoden basieren auf demselben zu Grunde liegenden FR-KKR Framework. Der Vergleich konzentriert sich auf den Teil der Akku-

mulation, der ungerade unter räumlicher Magnetisierungs-Inversion ist und alleine von den Bandstruktureigenschaften an der Fermi-Oberfläche verursacht wird. Ein Vergleich zeigt, dass beide Methoden einen ähnlichen Trend für eine Reihe von Metallen liefern, in denen die Spin-Bahn-Kopplung eine Rolle spielt. Dies macht die neue Keldysh-Methode zu einem glaubhaften Kandidaten zur Berechnung der Magnetisierungs-Akkumulation, die durch den Spin-Hall-Effekt verursacht wird. In diesem Ansatz werden außerdem im Gegensatz zu den meisten theoretischen Beschreibungen, die sich auf die Spin-Leitfähigkeit als Volumen-Eigenschaft konzentrieren, der Dünnfilmcharakter und die Oberflächeneinflüsse berücksichtigt. Dadurch ist es möglich, die Ergebnisse in direkter Weise mit dem Experiment in Verbindung zu setzen. Beim Vergleich mit einer experimentellen Reihe an Metallen zeigt sich, dass auch der Trend für den Spin-Hall-Winkel richtig wiedergegeben wird.

Der zweite Teil dieser Thesis behandelt die Frage, wie man die Selbstenergie im Rahmen des Büttiker-Streu-Verfahrens (Streuung mit virtuellen Terminals) verstehen muss, welches bereits in die KKR integriert wurde. Dazu wird die Beziehung der Selbstenergie $\Sigma$, die in diesem Verfahren genutzt wird, zur Streuzeit $\tau$, die in der Boltzmann-Theorie verwendet wird, untersucht. Innerhalb der *constant relaxation time approximation* (CRTA) der Boltzmann-Theorie is der Seebeck-Koeffizient unabhängig von der Streuzeit. Für ein System von freien Elektronen und Kupfer (Cu) gilt dies auch für die Streuung mit virtuellen Terminals im Grenzfall schwacher Streuung. Allerdings ist dies nicht mehr der Fall für Palladium (Pd). Der Schluss liegt nahe, dass dies mit der Komplexität der Fermi-Oberfläche zusammenhängt. Weiterhin wird untersucht, welche Einschränkungen bei Benutzung der Methode mit virtuellen Terminals vorliegt. So muss z.B. die Anzahl der Streuereignisse mittels einer ausreichenden Anzahl von virtuellen Terminals aufgelöst werden. Auf diesen Erkenntnissen basierend wird zum Abschluss noch die Skalierbarkeit dieses Ansatzes diskutiert, da die Berücksichtigung von Streuung die Möglichkeit eröffnet, Spin-Relaxations-Effekte im Rahmen des Spin-Hall-Effektes mitzuberücksichtigen.

Die Ergebnisse dieser kumulativen Thesis sind in PHYS. REV. B **104**, 054402, (2021) und PHYS. REV. B **105**, 165106, (2022) veröffentlicht.

# 2. Preface

## 2.1. Motivation

Today's electronic devices are shrinking in size at a relatively fast pace. Moore's law[1] predicted the doubling of density on integrated circuits every year [1]. At the current rate and the sizes achieved, quantum mechanical effects take more and more effect. Nevertheless, not only the charge degree of freedom that is commonly used in conventional electronics, but also the spin degree of freedom can be used. For example, in spintronics, the magnetic random access memory (MRAM) [2] is a promising technological application that enables one to use non-volatile memory for computer systems. More recent approaches that consider the quantum mechanical nature of the effects have to be found to facilitate the development of new applications and understand the fundamental principles. Such approaches, such as the already established Kubo formalism [3–7], are the logical next step to the most often used semi-classical approaches [8–12] as they can be used in scopes where the semi-classical approaches fail.

One aim of this work is the description of the spin Hall effect. When looked up in literature, the term spin Hall effect can refer to different quantities characteristic of the effect. For example, primarily theoretical works characterize the spin Hall effect by the transversal spin conductivity. This quantity is often used in conjunction with the longitudinal charge conductivity to obtain the value of the spin Hall angle from which the efficiency of charge-to-spin conversion is derived. While the spin conductivity is also derived from experiments, optical measurements, such as magneto-optical Kerr effect (MOKE) measurements, measure the spin accumulation directly but often lack a direct quantitative description. Additionally, the development of a method is feasible that integrates the description of effects on an equal footing with the underlying framework. The development will be done in this work using the non-equilibrium Green's function method, which integrates well with the full-relativistic framework of the Green's function based Korringa-Kohn-Rostoker (KKR) density functional theory (DFT). It is necessary to expand the capabilities of the KKR code, especially to combine contributions to the electronic density from the Fermi sea (equilibrium part) and the Fermi surface (non-equilibrium part) in the integration path of the complex energy contour. A side effect of this is that it becomes possible to calculate capacitor-like tunneling barriers. When the equilibrium density is deducted from the non-equilibrium density, the excess charge density and the applied bias voltage make it possible to obtain the capacitance of the tunneling barrier. Such a capacitance calculation was done for lithium (Li) in Ref. [13]. In analogy to the magnetoresistance, the aim was to calculate the capacitance of a ferromagnetic Fe tunneling barrier in a parallel and anti-parallel magnetic configuration to extend upon this approach. Some results of this approach will be shown in the appendix.

---

[1]Although discussions are going on about whether or not Moore's law is slowing down or, on the contrary, speeding up.

We characterize the spin Hall effect by the appearing surface magnetization. In order to classify the obtained results via the KKR approach, we compare them to values obtained by a semi-classical Boltzmann approach. To facilitate this comparison, we limit ourselves to odd-under-spatial-inversion magnetization contributions [12, 14, 15].

The results are published in Phys. Rev. B **104**, 054402, (2021) [16].

The second part of this work is the application of the scattering approach implemented in a previous work [17, 18]. The approach is based on the virtual terminal or Büttiker probes method by Büttiker[19], which introduces scattering into the KKR non-equilibrium Green's function approach.
Here again, to assess the comparability to the semi-classical Boltzmann approach, we separate contributions from scattering and the contact resistance, assess the identification of the self-energy $\Sigma$ to the scattering time $\tau$ and discuss the limits of the virtual terminal approach.

The results are published in Phys. Rev. B **105**, 165106, (2022) [20].

By introducing scattering via virtual terminals, it could become possible to calculate the contributions of the spin Hall effect with effects of spin relaxation and get a measure for the spin-diffusion lengths. However, as we have shown in the paper, care must be taken when interpreting the results obtained with the virtual terminal method. One main point here is that the self-energy $\Sigma$ is not directly to be identified with the scattering time $\tau$ for systems that possess a complex structure of the Fermi surface.
However, a promising feature of the approach is the scalability of the system, which could be achieved by simply scaling the self-energies to match the desired system size. With this, under certain conditions that meet the considerations described mainly in the second half of the paper, it should be possible to describe more realistic experimental structures.

# Commonly used Symbols

Calligraphic symbols, like $\mathcal{H}$, and carets - when a calligraphic version is not available - like $\hat{\mathbf{p}}$, denote operators.

The operator $\mathcal{G}$ and the function $G(\mathbf{r}, \mathbf{r}', z)$ are both called Green's function.

Underlined quantities represent matrices, like the matrix $\underline{A}$.

Bold faced quantities represent vectors, like the momentum vector $\mathbf{p}$. Normal type face characters represent a scalar value, a component or the absolute value of the corresponding vector and will be mentioned in the main text.

Quantities with a super script 0 or a circle on top, like $\left|\psi^0\right\rangle$ or $\mathring{G}$, generally mean they are quantities of a reference system.

Generally speaking, the conventions and notations mentioned here are overwritten in meaning when mentioned otherwise in the text.

| Symbol | Description |
|---|---|
| **General physical quantities** | |
| $H$ | Hamiltonian |
| $G$ | Green's function |
| $V$ | potential |
| $\mathbf{r}$ | position vector |
| $\mathbf{p}$ | momentum |
| $\mathbf{v}$ | velocity |
| $\mathbf{k}$ | wave vector |
| $n$ | electronic density |
| $\theta$ | temperature |
| $f(E, \mu, \theta)$ | Fermi-Dirac distribution |
| | |
| **Energies** | |
| $E$ | real energy |
| $z$ | complex energy |
| $E_F$ | Fermi energy |
| $\mu$ | chemical potential |
| $E_B$ | band bottom energy |
| $\Sigma$ | self-energy |
| $\Gamma$ | broadening function |
| | |
| **Transport quantities** | |
| $T$ | transmission function |
| $a$ | lattice parameter |
| $\sigma$ | conductivity |
| $\mathcal{E}$ | electric field |
| $S$ | Seebeck coefficient or thermopower |
| $\varphi$ | bias voltage |

**Times**

| | |
|---|---|
| $t$ | time |
| $\tau$ | scattering time |

**Natural constants**

| | |
|---|---|
| $e$ | electron charge |
| $m$ | electron mass |
| $M$ | core mass |
| $k_B$ | Boltzmann constant |
| $\mu_B$ | Bohr magneton |
| $c$ | speed of light |
| $h$ | Planck constant |
| $\hbar$ | reduced Planck constant $\hbar = \frac{h}{2\pi}$ |

**Mathematical functions**

| | |
|---|---|
| $j_\ell$ | spherical Bessel functions |
| $h_\ell^+$ | spherical Hankel functions |
| $\delta(x - x')$ | Dirac distribution |
| $\delta_{nn'}$ | Kronecker symbol |

# 3. Theory

Since this work is mainly concerned with non-equilibrium features, we start with the introduction of the non-equilibrium Green's function method. This is followed by the theory of scattering via virtual terminals and an application of a finite differences method (FDM). The chapter closes with the theory of the Boltzmann transport and an overview of the spin Hall effect. The basic principles of density functional theory (DFT) formulated in the Korringa-Kohn-Rostoker (KKR) formalism are given in the appendices A.1, A.2, and A.3.

## 3.1. Non-Equilibrium Steady State Features

Within the Green's function approach to KKR it is convenient to expand the formalism to a steady state non-equilibrium mode via the introduction of the non-equilibrium Green's function method. For the non-equilibrium formalism, it is necessary to partition the space in a particular manner. This partitioning of space is shown in Fig. 3.1. We will refer to it as the transport geometry from now on. To describe electrons traveling from left to right, it is convenient to have a source and a drain on the left and right side of the system from which the electrons can enter the system from an equilibrium state and leave and relax to equilibrium again. These are called left (L) and right (R) lead. We introduce a center region (C) between the source and drain, where all the interesting physics can occur. This partitioning approach has proven to work well [21, 22].
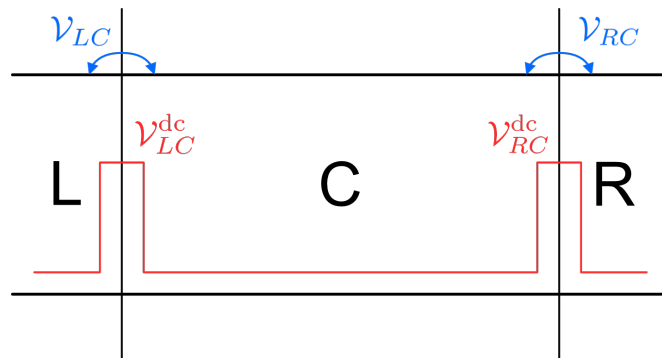


Figure 3.1.: Partitioning of space in the transport geometry. The isolated system is coupled via $\mathcal{V}_{LC/RC}$ (shown in blue). In KKR, not the solution for the isolated system is known, but the solution for the coupled system is. To obtain the solution for the isolated system, the system has to be decoupled by a decoupling potential (shown in red). Figure after [22].

The three regions of the decoupled system can now be described by a partitioned Hamiltonian $\mathcal{H}_{\mathrm{DC}}$, where each region is isolated from one another [23]:

$$\mathcal{H}_{\mathrm{dc}} = \begin{pmatrix} \mathcal{H}_L & 0 & 0 \\ 0 & \mathcal{H}_C & 0 \\ 0 & 0 & \mathcal{H}_R \end{pmatrix}. \tag{3.1}$$

The coupling of the regions is then realized by a suitable coupling potential [23]

$$\mathcal{V}_c = \begin{pmatrix} 0 & \mathcal{V}_{LC} & 0 \\ \mathcal{V}_{CL} & 0 & \mathcal{V}_{CR} \\ 0 & \mathcal{V}_{RC} & 0 \end{pmatrix}. \tag{3.2}$$

The coupling potential is indicated in blue in Fig. 3.1. The resulting Hamiltonian $\mathcal{H} = \mathcal{H}_{dc} + \mathcal{V}_c$ is used to find the Green's function $\mathcal{G} = (E\mathcal{I} - \mathcal{H})^{-1}$, where $E$ is the energy and $\mathcal{I}$ the identity operator, which means

$$\begin{pmatrix} \mathcal{G}_{LL} & \mathcal{G}_{LC} & \mathcal{G}_{LR} \\ \mathcal{G}_{CL} & \mathcal{G}_{CC} & \mathcal{G}_{CR} \\ \mathcal{G}_{RL} & \mathcal{G}_{RC} & \mathcal{G}_{RR} \end{pmatrix} \begin{pmatrix} E\mathcal{I} - \mathcal{H}_L & -\mathcal{V}_{LC} & 0 \\ -\mathcal{V}_{CL} & E\mathcal{I} - \mathcal{H}_C & -\mathcal{V}_{CR} \\ 0 & -\mathcal{V}_{RC} & E\mathcal{I} - \mathcal{H}_R \end{pmatrix} = \begin{pmatrix} \mathcal{I} & 0 & 0 \\ 0 & \mathcal{I} & 0 \\ 0 & 0 & \mathcal{I} \end{pmatrix}. \tag{3.3}$$

From this equation, we get three conditional equations, that define the center Green's function $\mathcal{G}_{CC}$ as [17, 23]

$$\mathcal{G}_{CL}(E\mathcal{I} - \mathcal{H}_L) - \mathcal{G}_{CC}\mathcal{V}_{CL} = 0 \tag{3.4}$$

$$-\mathcal{G}_{CL}\mathcal{V}_{LC} + \mathcal{G}_{CC}(E\mathcal{I} - \mathcal{H}_C) - \mathcal{G}_{CR}\mathcal{V}_{RC} = \mathcal{I} \tag{3.5}$$

$$-\mathcal{G}_{CC}\mathcal{V}_{CR} + \mathcal{G}_{CR}(E\mathcal{I} - \mathcal{H}_R) = 0. \tag{3.6}$$

The Green's function in the center region $G_{CC}$ is then evaluated in terms of the (lead) self-energies $\Sigma_L$ and $\Sigma_R$ as

$$\mathcal{G}_{CC} = (E\mathcal{I} - \mathcal{H}_C - \Sigma_L - \Sigma_R). \tag{3.7}$$

The infinite Hamiltonian has now been truncated to a finite one where the self-energies describe the coupling of the center region to the leads [24]. The self-energies $\Sigma_L$ and $\Sigma_R$ of the leads have to be determined via the surface Green's functions $\tilde{\mathcal{G}}_L$ and $\tilde{\mathcal{G}}_R$, respectively, such that the total self-energy $\Sigma_l$ caused by the leads reads

$$\Sigma_l = \Sigma_L + \Sigma_R = \mathcal{V}_{CL}\tilde{\mathcal{G}}_L\mathcal{V}_{LC} + \mathcal{V}_{CR}\tilde{\mathcal{G}}_R\mathcal{V}_{RC}. \tag{3.8}$$

Here, the elements $\tilde{\mathcal{G}}_L$ and $\tilde{\mathcal{G}}_R$ of the Green's function from the isolated Hamiltonian have to be used, which are given by

$$\mathcal{G}_{\mathrm{dc}} = (E\mathcal{I} - \mathcal{H}_{\mathrm{dc}})^{-1} = \begin{pmatrix} \tilde{\mathcal{G}}_L & 0 & 0 \\ 0 & \tilde{\mathcal{G}}_C & 0 \\ 0 & 0 & \tilde{\mathcal{G}}_R \end{pmatrix}. \tag{3.9}$$

Actually, in the KKR, the coupled Green's function is known by means of the decimation technique [25, 26], sometimes referred to as Sancho-Rubio method [27, 28]. To decouple the system, a decoupling potential is introduced [23]. This decoupling potential is shown in red in Fig. 3.1. Under the assumption of a high decoupling potential $\mathcal{V}_{LC}^{dc}$ and $\mathcal{V}_{RC}^{dc}$

and under the assumption of non-interacting leads [22], that is, if the leads are separated and the self-energy can be written as a sum of the self-energy from the left and right lead, the self-energies are given by [23]

$$\Sigma_{L/R} = \mathcal{V}_{L/R}^{dc} \tilde{\mathcal{G}}_{dc} \mathcal{V}_{L/R}^{dc}. \tag{3.10}$$

Because the reference potential is already highly repulsive, it can be used as a decoupling potential (see also Appendix A.3.5). To obtain the necessary surface Green's functions, the decimation technique is employed on the reference potential. Note that a banded matrix is needed for the decimation technique to work. This banded matrix structure is enabled by the semi-infinite leads and the screening introduced in the screened KKR. Further details of the representation in the KKR basis can be found in Refs. [17, 22, 23].

### 3.1.1. Non-Equilibrium Electron Density

To calculate the expression for the non-equilibrium density, we need the Green's function from the center region

$$\mathcal{G}_{CC}(z) = (z\mathcal{I} - \mathcal{H}_C - \Sigma_l)^{-1} \tag{3.11}$$

$$\mathcal{G}_{CC}^{\dagger}(z) = (z^*\mathcal{I} - \mathcal{H}_C - \Sigma_l^{\dagger})^{-1}. \tag{3.12}$$

Subtracting the inverse Green's functions from one another, we obtain a useful relation in terms of the lead self-energies

$$\left(\mathcal{G}_{CC}^{\dagger}\right)^{-1} - \mathcal{G}_{CC}^{-1} = -2i \operatorname{Im} z \, \mathcal{I} + \Sigma_l - \Sigma_l^{\dagger}. \tag{3.13}$$

The electron density is defined in Eq. A.58. Expansion and use of the above relation grants us an expression for the non-equilibrium density operator [18]

$$\hat{n}_C = \frac{i}{2\pi}(\mathcal{G}_{CC} - \mathcal{G}_{CC}^{\dagger}) \tag{3.14}$$

$$= \frac{i}{2\pi}\mathcal{G}_{CC}((\mathcal{G}_{CC}^{\dagger})^{-1} - \mathcal{G}_{CC}^{-1})\mathcal{G}_{CC}^{\dagger} \tag{3.15}$$

$$= \frac{1}{2\pi}\mathcal{G}_{CC}\Gamma\mathcal{G}_{CC}^{\dagger} + \frac{1}{\pi}\operatorname{Im} z\mathcal{G}_{CC}\mathcal{G}_{CC}^{\dagger}, \tag{3.16}$$

where the broadening function $i\Gamma = \Sigma^{\dagger} - \Sigma$ is introduced. When integrating this equation over the energy to obtain the local electron density, the left part introduces a distribution function, which stems from the left and right leads as $\Gamma_{L/R}$ only exists on the left and right side. This distribution function is a simple Fermi-Dirac distribution as the leads are in equilibrium. The second term introduces a non-equilibrium distribution function from the center region, which is not known *a priori*. Therefore, it becomes difficult to use the complex energy contour for integration, and we have to restrict ourselves to real energy values so that the second term vanishes. Integrating alongside the real axis, however, is computationally very demanding, as the structure of the Green's function involves the usage of many energy and **k**-points. A solution to this issue is to use a combined energy contour, where the equilibrium parts of the density are calculated within the conventional equilibrium formalism and only the non-equilibrium part is calculated alongside the real axis.

### 3.1.2. Equilibrium Contours

To compute the space-resolved electron density, the Green's function has to be integrated over the energy. According to $\mathcal{G} = (z\mathcal{I} - \mathcal{H})^{-1}$, the Green's function has poles at the eigenenergies of the Hamiltonian on the real axis. These poles make it necessary to use a dense energy mesh around them. Instead of integrating over the sharp poles, by introducing complex energies, a broadening of these poles of the Green's function in the complex plane can be achieved. Due to this broadening, fewer energy points can be used. Formally, the integrand of the density is multiplied with a Fermi-Dirac distribution at $\theta = 0$ K since only states up to the Fermi-Energy have to be considered. This distribution also introduces the so-called Matsubara poles, which for $\theta = 0$ K lie infinitely dense as we will see. It is, therefore, convenient to introduce a technical temperature that only affects the electrons but not the cores, that is, no phonons are created. The contributions below and above the Fermi energy should cancel out such that this technical temperature has no additional effect.

The commonly used contour is of a regular shape, which is depicted in Fig. 3.2. The path goes up in the complex plane and then from left to right up to the Fermi energy. From there, it would normally go down again. Due to the Fermi-Dirac distribution function

$$f(z, \mu, \theta) = \frac{1}{\exp\left(\frac{z-\mu}{k_B\theta}\right) + 1},\tag{3.17}$$

where $z$ is the complex energy, $\mu$ the chemical potential, and $\theta$ the temperature, starting to vanish at real parts of the energy above the Fermi energy, instead of returning to the real axis, it is possible to continue the contour in complex infinity, effectively closing it. The Fermi distribution exhibits poles in the complex energy plane at [29]

$$\tilde{z}_j = \mu - i\pi(2j-1)k_B\theta.\tag{3.18}$$

These residues have to be accounted for when using Cauchy's residue theorem. Finally, a corrected version of the density has to be calculated, which after incorporating the Fermi-Dirac function reads [30]

$$n(\mathbf{r}) = -\frac{2}{\pi}\,\mathrm{Im}\left(\int_{E_B}^{z_n} G(\mathbf{r},\mathbf{r},z)\mathrm{d}z + \frac{\pi^2}{6}(k_B\theta)^2 G'(z_n) + 2\pi i k_B\theta\sum_j G(\mathbf{r},\mathbf{r},\tilde{z}_j)\right),\tag{3.19}$$

where $N$ is the number of Matsubara poles enclosed by the contour, $G'(z_n)$ the derivative of the Green's function with respect to energy at $z_n$, and $z_N = \mu - i\pi N k_B\theta$ is a point between the $N$-th and $(N+1)$-th Matsubara pole. Actually, the second part of the equation containing the derivative $G'(z_n)$ is very small within the considered applications and premises in Ref. [30] and, therefore, can be neglected. This contour is used for self-consistent calculations for bulk materials.

Another way to calculate the density is via a semi-circular contour and a vanishing technical temperature, which is depicted in Fig. 3.3. The contour starts from band bottom $E_B$ and then describes a semi-circle in the upper half of the complex plane before it returns to the real axis at the Fermi energy $E_F$ with the radius $r_E = \frac{E_F - E_B}{2}$. Because of the vanishing temperature, no poles have to be accounted for. Another advantage is that from there, it is possible to continue a second, different contour,
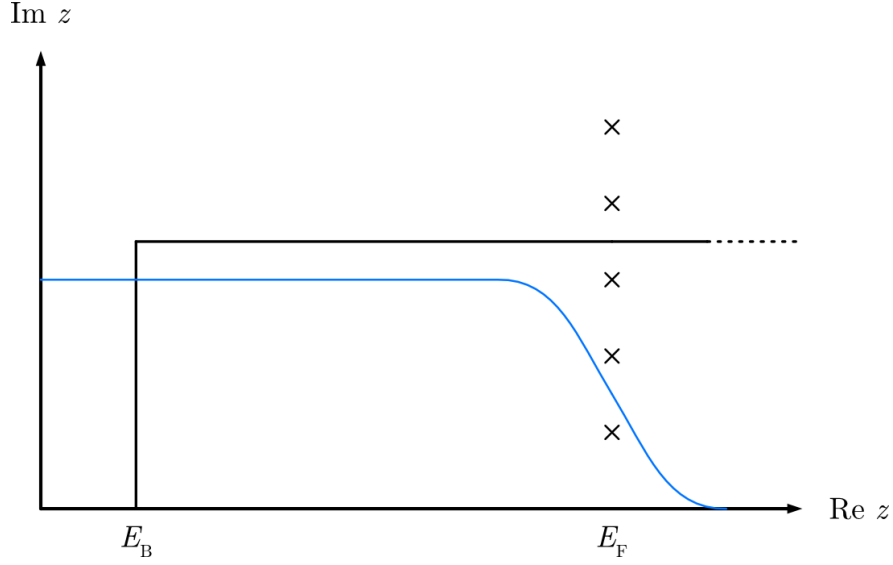
Figure 3.2.: Rectangular-shaped contour, which is "closed" in complex infinity. The blue line shows the Fermi Dirac distribution for a temperature $T > 0$. The dots in the contour indicate that the distribution function has vanished enough to make no contributions anymore.

which will be actually done for the combination of the equilibrium and non-equilibrium densities.

Instead of closing the contour right away to the real axis, the contour can be closed similarly to the rectangular contour [13, 31]. This introduces the technical temperature from before again. However, as we want to continue the semicircular contour at the real axis to calculate the non-equilibrium parts, this broadening due to the technical temperature introduces an overlapping [13] between the two contours, which results in double counting of contributions. To avoid this effect, it is easier to close the semicircle on the real axis and continue from there.

The semi-circular contour is used for self-consistent calculations in transport geometry in this work since it is similar to the combined contour in its conversion behavior, which will be described next.

### 3.1.3. Combined Energy Contour

The expression for the electronic density can be reformulated in terms of the broadening functions or self-energies of the leads in the transport geometry. This yields the left and right non-equilibrium densities $n_{L/R} = \frac{1}{2\pi} G \Gamma_{L/R} G^{\dagger}$, respectively [17, 22, 24]. The complete electron density of the valence states can be rewritten in terms of this left and right electron density [13]: Let $\mu_L$ and $\mu_R$ be the respective chemical potentials of the left and right lead, respectively. If $\mu_L = \mu_R \equiv \mu$ holds we get for $n$

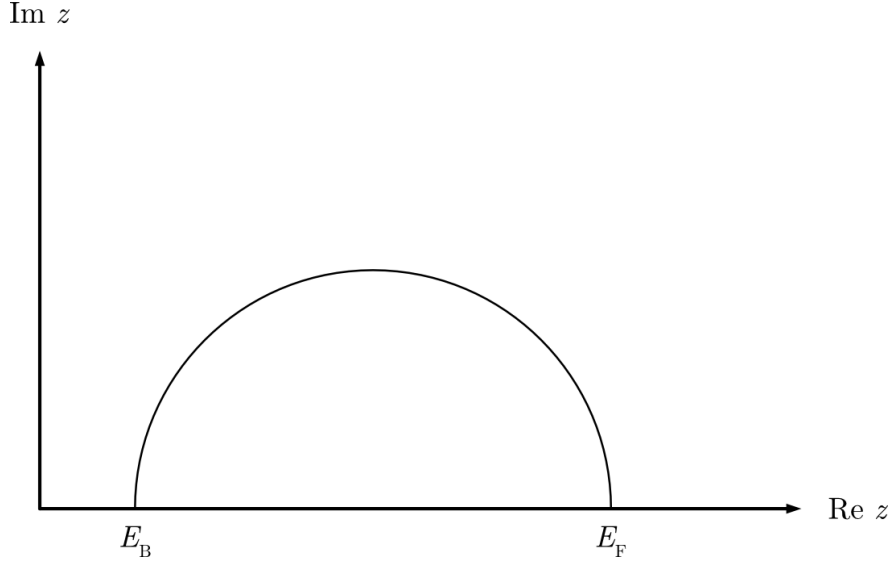$$n = \int (n_L(E) + n_R(E)) f(E - \mu) \, \mathrm{d}E. \tag{3.20}$$

Figure 3.3.: Semicircular contour in the upper complex plane.

Now, for $\mu_L \neq \mu_R$ and assuming $\mu_R < \mu_L$ we get [13]

$$n = \int n_L(E)f(E - \mu_L) + n_R(E)f(E - \mu_R) \, \mathrm{d}E \tag{3.21}$$

$$= \int n_L(E)(f(E - \mu_R) + f(E - \mu_L) - f(E - \mu_R)) + n_R(E)f(E - \mu_R) \, \mathrm{d}E \tag{3.22}$$

$$= \int (n_L(E) + n_R(E))f(E - \mu_R) + n_L(E)(f(E - \mu_L) - f(E - \mu_R)) \, \mathrm{d}E. \tag{3.23}$$

This means we can split the integral into an equilibrium part and a non-equilibrium part. The first part can be calculated within the equilibrium formalism and the semicircular contour in the complex plane

$$n_{\text{EQ}} = -\frac{1}{\pi} \operatorname{Im} \oint_{E_B}^{\mu_<} G(\mathbf{r}, \mathbf{r}; z) \mathrm{d}z \tag{3.24}$$

and a non-equilibrium part in between the applied bias window

$$n_{\text{NEQ}} = \frac{1}{2\pi} \int_{\mu_<}^{\mu_>} G\Gamma_\iota G^\dagger \mathrm{d}E, \qquad \iota = \begin{cases} L & \text{for } \mu_< = \mu_R \\ R & \text{for } \mu_< = \mu_L \end{cases}. \tag{3.25}$$

Here the notation $\mu_< = \min(\mu_R, \mu_L)$ and $\mu_> = \max(\mu_R, \mu_L)$ is used, as this works for biases applied in both directions. Due to this splitting, it is possible to use the computationally efficient way in the complex plane and only apply the real-axis way to the quite small bias window. The contour is shown in Fig. 3.4. From the band bottom up to $\mu_<$, the conventional equilibrium mechanism is used. In the window of applied bias, which is from $[\mu_<, \mu_>]$, the non-equilibrium formalism is employed.

### 3.1.4. Landauer-Büttiker Formula

In the Landauer-Büttiker model, the idea is that the conductance is mainly determined by transmission and reflection probabilities $T$ and $R = 1 - T$, respectively. The linear
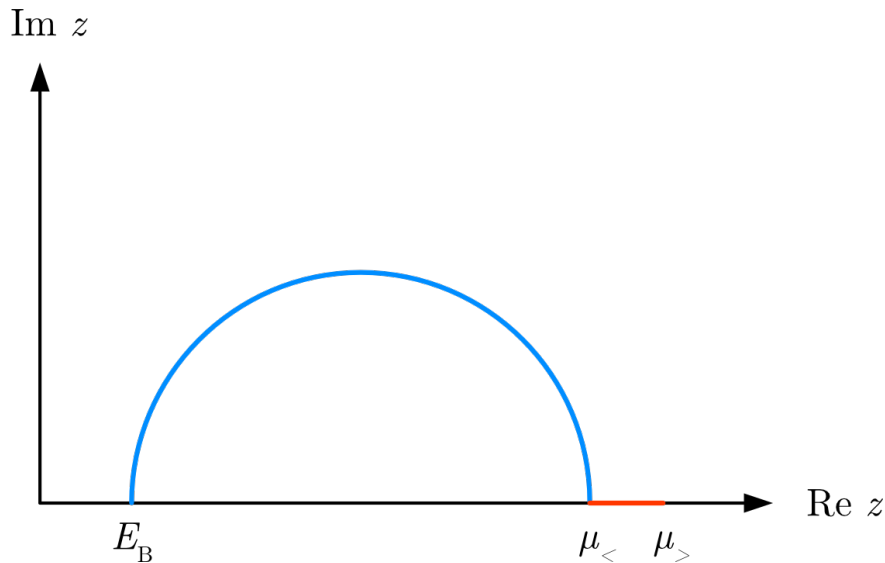
Figure 3.4.: Combined contour consisting of a semi-circular contour for the equilibrium density (blue) and a straight line near the real axis for the non-equilibrium part (red).

response method yields for the conductance $G = \frac{e^2}{h}T$, so although the transmission can be perfect, still the conductance is only a finite value. This is due to the fact that the latter expression refers to the contact resistance. There are only certain modes in the center region, which can contribute to the transport. Not all of the electrons from the equilibrium leads can go into the center region due to this restriction [32].

Let us further define the following coordinate system. Let $z$ be the direction of transport. Then $x$ and $y$ will be the directions in the plane perpendicular to the transport direction. The current entering from the left and going to the right side is determined via [32]

$$I_{L \to R} = \frac{e}{2\pi} \int_0^\infty T_{LR}(k_z) v_L(k_z) f_L(k_z) \, \mathrm{d}k_z \qquad (3.26)$$

with $k_z > 0$ since right-going electrons from the left side are considered, $v_L(k_z)$ the velocity of an electron from the left side, and $f_L(k_z)$ the distribution function. This integral can be evaluated to an integration over energy, since the relation $v(k_z) = \frac{1}{\hbar} \frac{\partial E}{\partial k_z}$ holds [32]:

$$I_{L \to R} = \frac{e}{h} \int_{E_L}^\infty T_{LR}(E) f_L(E) \, \mathrm{d}E, \qquad (3.27)$$

where $E_{L/R}$ are the conduction band bottom energies on the left and right side, respectively. Similar, one finds [32]

$$I_{R \to L} = \frac{e}{h} \int_{E_R}^\infty T_{RL}(E) f_R(E) \, \mathrm{d}E. \qquad (3.28)$$

Taking time reversal symmetry into account, which means that $T_{LR} = T_{RL}$, this means for the resulting current [32]

$$I = I_{L \to R} - I_{R \to L} = \frac{e}{h} \int_{-\infty}^\infty T(E) \left( f_L(E) - f_R(E) \right) \, \mathrm{d}E. \qquad (3.29)$$

where $f_L$ and $f_R$ are the equilibrium distribution functions for the left and right side, respectively.

If a voltage $\varphi$ is applied, that is, let's assume $\mu_L \to \mu_L + e\varphi$ and $\mu_R \to \mu_R$, then this formula modifies to [32]

$$I(\varphi) = \frac{e}{h} \int_{-\infty}^{\infty} T(E, \varphi)(f_L(E - e\varphi) - f_R(E)) \, \mathrm{d}E, \tag{3.30}$$

For vanishing bias $\varphi \to 0$, the conductance is found as

$$\lim_{\varphi \to 0} I = \lim_{\varphi \to 0} \frac{e}{h} \int_{-\infty}^{\infty} T(E, \varphi)(f_L(E - e\varphi) - f_R(E)) \, \mathrm{d}E \tag{3.31}$$

$$= \frac{e}{h} T(E_F) e\varphi = G\Delta\varphi \tag{3.32}$$

$$\Rightarrow G = \frac{e^2}{h} T(E_F). \tag{3.33}$$

### 3.1.5. Transmission Function

As we already have seen, the knowledge of the transmission function of the electrons is vital. From the Green's functions and the self energies, it is possible to calculate the transmission function in $\mathbf{k}_\parallel = (k_x, k_y)$ space, that is, the in-plane Brillouin zone. Since the translational invariance in transport geometry is broken, $k_z$ is no longer a good quantum number. Hence the transmission function is resolved in $\mathbf{k}_\parallel$, that is $k_x$ and $k_y$ resolved. The $\mathbf{k}_\parallel$ dependent transmission function can be calculated via

$$T_{LR}(E, \mathbf{k}_\parallel) = \mathrm{Tr}\left[\underline{\Gamma}_L(E, \mathbf{k}_\parallel)\underline{G}(E, \mathbf{k}_\parallel)\underline{\Gamma}_R(E, \mathbf{k}_\parallel)\underline{G}^\dagger(E, \mathbf{k}_\parallel)\right]. \tag{3.34}$$

To obtain the resulting integrated transmission function $T_{LR}(E)$, $T_{LR}(E, \mathbf{k}_\parallel)$ has to be integrated over the in-plane Brillouin zone.

The transmission function obtained here only accounts for coherent scattering as it occurs, for example, in a tunneling barrier. In the case of a bulk conductor, the coherent part is equivalent to the quantum mechanical contact resistance. It can be seen as a measure of how many channels in $\mathbf{k}_\parallel$ space are available for electrons coming from a free electron gas in the leads. Whether such a channel is available will add to the resistance. As the resistance is mainly determined from the type of contact, it is independent of the length of the system[1].

### 3.1.6. Multiple Scattering – Virtual Terminals

While the transmission function described before only accounts for the coherent parts, it is also possible to include phase breaking or incoherent scattering via so-called virtual terminals or Büttiker probes. The virtual terminals are placed throughout the scattering region. At each virtual terminal electrons can enter and leave the system changing their phase. In this way, phase-breaking scattering events can be realized. The scattering potential at site $\alpha$ is normally described by a complex self-energy $\bar{\Sigma}_\alpha$. For phonon scattering only the negative imaginary part $\Sigma_\alpha = -\mathrm{Im}\,\bar{\Sigma}_\alpha$ is relevant. Each virtual terminal is assigned with self-energy $\Sigma_\alpha = -\mathrm{Im}\,\bar{\Sigma}_\alpha$. From this self energy, the

---

[1]Unless the system is small enough to allow for direct tunneling from left to right lead. However, this case usually is not considered in the derivation of the NEGF formulae.

broadening $\underline{\Gamma}_\alpha = i\left(\bar{\Sigma}_\alpha \underline{I}_\alpha - \bar{\Sigma}_\alpha^\dagger \underline{I}_\alpha\right) = -2\,\mathrm{Im}\,\bar{\Sigma}_\alpha \underline{I}_\alpha) = 2\Sigma_\alpha \underline{I}_\alpha$ can be calculated. The matrix $\underline{I}_\alpha$ is 1 only for one site index $\alpha$ and 0 elsewhere. Using the broadening function, the $\mathbf{k}_\parallel$ resolved transmission

$$T_{\alpha\beta}(E, \mathbf{k}_\parallel) = \mathrm{Tr}\left[\underline{\Gamma}_\alpha \underline{G}(E, \mathbf{k}_\parallel)\underline{\Gamma}_\beta \underline{G}^\dagger(E, \mathbf{k}_\parallel)\right] \tag{3.35}$$

from terminal $\alpha$ to terminal $\beta$ can be calculated. Integrating all contributions over the 2D Brillouin zone, one obtains $T_{\alpha\beta}(E)$. Together with the direct transmission from left (L) to right (R), the effective transmission is evaluated by [17, 33]

$$T_{\mathrm{eff}}(E) = T_{LR}(E) + \sum_{\alpha \in \mathcal{S}} \frac{T_{L\alpha}(E)T_{\alpha R}(E)}{S_\alpha(E)} + \sum_{\alpha,\beta \in \mathcal{S}}^{\beta \neq \alpha} \frac{T_{L\alpha}(E)T_{\alpha\beta}(E)T_{\beta R}(E)}{S_\alpha(E)S_\beta(E)} + \dots \tag{3.36}$$

This accounts for the multiple scattering routes that could, in principle, be taken. The sum

$$S_\alpha(E) = T_{L\alpha}(E) + T_{\alpha R}(E) + \sum_{\beta \in \mathcal{S}}^{\beta \neq \alpha} T_{\alpha\beta}(E) \tag{3.37}$$

renormalizes the probability measure. On the one hand, $T_{LR}$ is determined by the lead material via the broadenings $\Gamma_{L/R}$. On the other hand, $T_{LR}(E)$ is determined by the center Green's function, which in turn is determined by the whole potential including all additional complex self-energies $\bar{\Sigma}_i$ on the atomic positions. Therefore, $T_{LR}(E)$ is different from the pure ballistic transmission function when no scattering occurs. The series is infinite, but since each element gets smaller, it eventually converges. It can be shown in a strict mathematical way that the series possesses a limit similar to the geometrical series[2]. The limit is achieved by [18]

$$T_{\mathrm{eff}}(E) = T_{LR}(E) + \mathbf{T}_L(E)\left(1 - \underline{\bar{T}}(E)\right)^{-1}\bar{\mathbf{T}}_R(E), \tag{3.38}$$

where for simplification the vector and matrix notations $\mathbf{T}_L = \{T_{L\alpha}\}_{\alpha \in \mathcal{S}}$, $\bar{\mathbf{T}}_R = \{T_{\alpha R}/S_\alpha\}_{\alpha \in \mathcal{S}}^T$ and $\underline{\bar{T}} = \{T_{\alpha\beta}/S_\alpha\}_{\alpha,\beta \in \mathcal{S}}$ with $T_{\alpha\alpha} = 0$ are used, respectively.
By first summing up the $\mathbf{k}_\parallel$ dependent $T_{\alpha\beta}(E)$, we allow energy-conserving $\mathbf{k}$ scattering. Other conservation rules are possible by using different summations. Also, a reconstruction of $T_{\mathrm{eff}}(E, \mathbf{k}_\parallel)$ by projection on the left and right states is possible. Both possibilities are not in the scope of this work. In order to distinguish contributions from different effects and in order to facilitate the comparison to semi-classical methods like the Boltzmann formalism, it is convenient to split the transmission function. The resistance of the whole system $R_{\mathrm{eff}}$ can be viewed as a series circuit of the contact resistance $R_c$ and the resistance due to scattering $R_S$. Consequently, it can be written as the sum

$$R_{\mathrm{eff}} = R_c + R_S. \tag{3.39}$$

The resistance is anti-proportional to the transmission function, from which it follows that:

$$\frac{1}{T_{\mathrm{eff}}(E)} = \frac{1}{T_c(E)} + \frac{1}{T_S(E)}. \tag{3.40}$$

---

[2]For a proof, see Ref. [18]

Here, $T_{\text{eff}}(E)$ is the effective transmission function, $T_c(E)$ is the transmission function, which results purely from the quantum mechanical contact of the leads to the scattering region, and $T_S(E)$ is the contribution exclusively due to scattering. This separation of contributions was not part of the preceding main work [17, 18], but proves to be useful for comparisons of the virtual terminal approach with the Boltzmann formalism, as the latter only possesses contributions due to scattering and no contributions from the quantum mechanical contact resistance.

### 3.1.7. Transport Moments

Several electronic transport quantities can be derived from the transmission function. To conveniently express them, the notation in terms of moments $L_n$, $n \in \mathbb{N}_0$ is useful. The moments $L_n$ are defined as [34]

$$L_n = \frac{2}{h} \int (E - \mu)^n \left( -\frac{\partial f(e, \mu, \theta)}{\partial E} \right) T(E) \, \mathrm{d}E. \tag{3.41}$$

With these moments, we can define the electronic charge conductivity as [35]

$$\sigma = e^2 L_0 \tag{3.42}$$

the Seebeck coefficient[3] $S$ as [35]

$$S = \frac{1}{e\theta} \frac{L_1}{L_0} \tag{3.43}$$

and the electronic heat conductivity $\kappa_e$ as [35]

$$\kappa_e = \frac{1}{\theta} \left( L_2 - \frac{L_1^2}{L_0} \right). \tag{3.44}$$

Depending on which part of the transmission is used, the resulting moments due to that part can be calculated. We will restrict ourselves in this work to the Seebeck coefficient $S$ due to scattering contributions $T_S(E)$ alone.

## 3.2. Finite Differences Method (FDM)

In the finite differences method (FDM) space is discretized onto a lattice [24].
The Hamiltonian in one dimension is

$$\mathcal{H} = \frac{\hat{p}^2}{2m} + \mathcal{V}(\hat{x}). \tag{3.45}$$

On the lattice with discrete points $x = ja$, where $j \in \mathbb{N}$, and $a$ is the lattice parameter, the operator $H$ on a test function $f$ works as [24]

$$[Hf]_{x=ja} = \left[ -\frac{\hbar^2}{2m} \frac{\mathrm{d}^2 f}{\mathrm{d}x^2} \right]_{x=ja} + V_j f_j \tag{3.46}$$

---

[3]The Seebeck coefficient is often referred to as thermopower in literature. However, it is a proportionality constant between the temperature difference and the resulting voltage, not a power unit in the physical sense. Therefore, we will continue to call it *Seebeck coefficient* for the theory part. We will call it thermopower in PHYS. REV. B **105**, 165106, (2022).

with $f_j \to f(x = ja)$ and $V_j \to V(x = ja)$.

The first derivative is taken at a point, which lies between two points of the lattice since this will prove useful for taking the second derivative [24]:

$$\left[\frac{\mathrm{d}f}{\mathrm{d}x}\right]_{x=(j+\frac{1}{2})a} = \frac{f_{j+1} - f_j}{a}. \tag{3.47}$$

Consequently, the second derivative is then found to be evaluated at an actual lattice point [24]:

$$\left[\frac{\mathrm{d}^2 f}{\mathrm{d}x^2}\right]_{x=ja} = \frac{1}{a}\left(\left[\frac{\mathrm{d}f}{\mathrm{d}x}\right]_{x=(j+\frac{1}{2})a} - \left[\frac{\mathrm{d}f}{\mathrm{d}x}\right]_{x=(j-\frac{1}{2})a}\right) \tag{3.48}$$

$$= \frac{f_{j+1} - 2f_j + f_{j-1}}{a^2}. \tag{3.49}$$

With this, the Hamiltonian on a discrete lattice is found as

$$H = \begin{cases} V_i + 2t & i = j \\ -t & i - j = \pm 1 \\ 0 & \text{else} \end{cases}, \tag{3.50}$$

where $t = \frac{\hbar^2}{2ma^2}$. $\underline{H}$ reads in matrix representation

$$\underline{H} = \begin{pmatrix} \ddots & \vdots & \vdots & \vdots & \vdots & \vdots & \iddots \\ \dots & V_{-2} + 2t & -t & 0 & 0 & 0 & \dots \\ \dots & -t & V_{-1} + 2t & -t & 0 & 0 & \dots \\ \dots & 0 & -t & V_0 + 2t & -t & 0 & \dots \\ \dots & 0 & 0 & -t & V_1 + 2t & -t & \dots \\ \dots & 0 & 0 & 0 & -t & V_2 + 2t & \dots \\ \iddots & \vdots & \vdots & \vdots & \vdots & \vdots & \ddots \end{pmatrix}. \tag{3.51}$$

The Hamiltonian takes the form of a tight binding Hamiltonian [24]. Because of its tridiagonal form, the infinite dimension of the matrix does not pose a problem. It can be truncated the same way as it is done for the non-equilibrium formalism in terms of self-energies. The self-energies for a thin wire with confining potential in $y$ direction is given by [24]

$$\Sigma(i,j) = -t \sum_{m \in p} \chi_m(p_i) e^{ik_m a} \chi_m(p_j), \tag{3.52}$$

where $\chi_m$ are the transversal modes of the finite conductor, $k_m$ is the wave vector of that mode, and $p_i$, $i \in \mathbb{N}$ is a point in the lead. From the discretized Hamiltonian we can derive some useful relations in lattice representation. If the Hamiltonian $\underline{H}$ acts on a plane wave $\psi_k(x) = e^{ikz}$ in $z$ direction, we obtain the energy dispersion

$$E = V_0 + \frac{\hbar^2 k^2}{2m} \tag{3.53}$$

on the discrete lattice as

$$E = V_0 + 2t(1 - \cos(ka)). \tag{3.54}$$

Since we want to obtain an FDM model for three dimensions, we have to consider the $x$ and $y$ direction separately. If there is no confining potential, we can use the lattice Fourier transformation [36]

$$A_i(q) = \sum_j e^{iq(x_i - x_j)} A_{ij}. \tag{3.55}$$

Since the Hamiltonian in 1D has a tight binding form that only considers nearest neighbors, we restrict ourselves to the nearest neighbors on the cubic lattice in the 3D case. First, we Fourier transform the $x$ direction:

$$H_i(k_x, y_i z_i, y_j z_j) = \sum_{x_j} e^{ik_x(x_i - x_j)} H(x_i y_i z_i, x_j y_j z_j) \tag{3.56}$$

$$= (-te^{-ik_x a} - te^{ik_x a} + 6t)\delta_{y_i y_j}\delta_{z_i z_j}$$
$$\quad - t\left(\delta_{y_i, y_j}\delta_{z_j, z_{i\pm1}} + \delta_{y_j, y_{i\pm1}}\delta_{z_j, z_i}\right) \tag{3.57}$$

$$= (-2t\cos k_x a + 6t)\delta_{y_i y_j}\delta_{z_i z_j}$$
$$\quad - t\left(\delta_{y_i, y_j}\delta_{z_j, z_{i\pm1}} + \delta_{y_j, y_{i\pm1}}\delta_{z_j, z_i}\right). \tag{3.58}$$

In the same way, the $y$-direction gets Fourier-transformed:

$$H_i(k_x, k_y, z_i, z_j) = \sum_{y_j} e^{ik_y(y_i - y_j)} H(k_x, y_i z_i, y_j z_j) \tag{3.59}$$

$$= (-2t\cos k_x a + -2t\cos k_y a + 6t)\delta_{z_i z_j} - t\delta_{z_j, z_{i\pm1}}. \tag{3.60}$$

The discretized and Fourier-transformed Hamiltonian then reads (the $d$ here stands for a fully discretized version)

$$H^d(k_x, k_y, z_i, z_j) = \begin{cases} 2t + 2t(1 - \cos(k_x a)) + 2t(1 - \cos(k_y a)) & z_i = z_j \\ -t & z_i, z_j \in \text{NN} \\ 0 & \text{else} \end{cases}. \tag{3.61}$$

When we compare Eq. 3.53 and Eq. 3.54, we already see that the dispersion for the discrete lattice can be re-translated to continuous space for the Fourier transformed directions[4], thus we can obtain a Hamiltonian with Fourier-transformed $x$ and $y$-directions in nearest neighbor approximation:

$$H^d \to H = \begin{cases} 2t + \frac{\hbar^2}{2m}(k_x^2 + k_y^2) & z_i = z_j \\ -t & z_i, z_j \in \text{NN} \\ 0 & \text{else} \end{cases}. \tag{3.62}$$

To obtain the matrix representation of the Green's function, the matrix $\underline{M}$ has to be inverted:

$$\underline{G} = \underline{M}^{-1} = (E\mathbb{1} - \underline{H} - \underline{\Sigma})^{-1}. \tag{3.63}$$

---

[4]This is possible here, as we only considered nearest neighbors.

with $\underline{\Sigma} = \Sigma_L \underline{I}_1 + \Sigma_R \underline{I}_n$. Again, here the matrix $\underline{I}_n$ is 1 only for one site index $n$ and 0 elsewhere. The final matrix to invert looks like

$$\underline{M} = \begin{pmatrix} E_{\text{eff}} - 2t - \Sigma_L & t & 0 & \cdots & 0 \\ t & E_{\text{eff}} - 2t & t & \cdots & 0 \\ \vdots & \vdots & \ddots & \vdots & \vdots \\ 0 & \cdots & t & E_{\text{eff}} - 2t & t \\ 0 & \cdots & 0 & t & E_{\text{eff}} - 2t - \Sigma_R \end{pmatrix}. \tag{3.64}$$

Here, we introduced the effective energy $E_{\text{eff}}(k_x, k_y) = E - \frac{\hbar^2}{2m}(k_x^2 + k_y^2)$. This means that the remaining problem is reduced to an effective 1D problem. The definition of the self energies for the effective 1D case of in-plane unconfined, free electrons with only one mode is given by

$$\Sigma_L = \Sigma_R = -t e^{ika}. \tag{3.65}$$

With this, the contact transmission function can be calculated.

To introduce scattering, also the self-energy for the scattering $\Sigma_S$ has to be added to the overall self-energy

$$\underline{\Sigma} = \Sigma_L \underline{I}_1 + \Sigma_R \underline{I}_n + \Sigma_S \mathbb{1}. \tag{3.66}$$

Consequently, the matrix $\underline{M}$ and the resulting Green's function now contain the information about the scattering. From the resulting Green's function $G$, the necessary transmission functions $T_{L\alpha}(E, \mathbf{k}_\parallel; \Sigma)$, $T_{\alpha R}(E, \mathbf{k}_\parallel; \Sigma)$, and $T_{\alpha\beta}(E, \mathbf{k}_\parallel; \Sigma)$ can be calculated at each $\mathbf{k}_\parallel$-point according to Eq. 3.35. The indices $\alpha$ and $\beta$ then refer to the lattice points where virtual terminals are placed. For energy conserving scattering, the effective transmission $T_{\text{eff}}(E, \mathbf{k}_\parallel; \Sigma)$ is computed via Eq. 3.36 at each $\mathbf{k}_\parallel$-point and then integrated over the Brillouin zone to obtain $T_{\text{eff}}(E; \Sigma)$. The scattering part $T_S(E; \Sigma)$ is then calculated the same way from Eq. 3.40.

It might seem counterintuitive at first that the self-energy due to scattering is not scaled according to the lattice parameter. We use a constant scattering potential barrier, so the discretization is the same at each lattice point. Also, the Green's function matrix scales according to the lattice parameter, which is then finally considered in the transmission formula since it is proportional to the scattering self-energy and the Green's function.

## 3.3. Boltzmann transport

Despite its classical origin, the Boltzmann equation is widely used today and has proven to yield sound results even for quantum mechanical systems. As a well established method with a variety of computable transport quantities it provides a reliable way to compare results of different approaches to it [8–12].

The Boltzmann transport equation reads [37]

$$\begin{aligned} \frac{\mathrm{d}f(\mathbf{k}, \mathbf{r}, t)}{\mathrm{d}t} &= \frac{\partial f(\mathbf{k}, \mathbf{r}, t)}{\partial t} + \frac{\partial f(\mathbf{k}, \mathbf{r}, t)}{\partial \mathbf{r}} \frac{\mathrm{d}\mathbf{r}}{\mathrm{d}t} + \frac{\partial f(\mathbf{k}, \mathbf{r}, t)}{\partial \mathbf{k}} \frac{\mathrm{d}\mathbf{k}}{\mathrm{d}t} \\ &= \sum_{\mathbf{k}'} -P_{\mathbf{k}\mathbf{k}'} f(\mathbf{k}, \mathbf{r}, t)(1 - f(\mathbf{k}', \mathbf{r}, t)) + P_{\mathbf{k}'\mathbf{k}} f(\mathbf{k}', \mathbf{r}, t)(1 - f(\mathbf{k}, \mathbf{r}, t)). \end{aligned} \tag{3.67}$$

Here, $f(\mathbf{k}, \mathbf{r}, t)$ is the distribution function in the phase space, and $P_{\mathbf{k}\mathbf{k}'}$ the transition probability rate from state $\mathbf{k}$ to $\mathbf{k}'$. Very often, this is not the form that is solved, as

it is a complicated integro-differential equation. Instead, a linearized version of it is solved. The linearized version of this equation for a homogenous system reads [38–40]

$$\dot{\mathbf{k}}\nabla_{\mathbf{k}}f_n^0(\mathbf{k}) = \sum_{\mathbf{k}'n'}\left(g_{n'}(\mathbf{k}')P_{\mathbf{k}\mathbf{k}'}^{nn'} - g_n(\mathbf{k})P_{\mathbf{k}'\mathbf{k}}^{n'n}\right) \tag{3.68}$$

where the ansatz

$$f_n(\mathbf{k}) = f_n^0(\mathbf{k}) + g_n(\mathbf{k}) \tag{3.69}$$

was made. Here, $f_n^0(\mathbf{k})$ is the equilibrium distribution function, and $g_n(\mathbf{k})$ a small difference from the equilibrium distribution function to the resulting distribution function $f_n(\mathbf{k})$. The distribution $f_n(\mathbf{k})$ here is now only dependent on $\mathbf{k}$ with an index $n$ for each band.

Note, that the microscopic reversibilty is not valid when spin-orbit interaction is present [38], that is $P_{\mathbf{k}\mathbf{k}'}^{nn'} \neq P_{\mathbf{k}'\mathbf{k}}^{n'n}$. The perturbation is caused by small fields and thus, only corrections linear in the electric field are necessary. Hence, the non-equilibrium distribution function is not far from equilibrium and can be written this way. A sufficient ansatz for $g_n(\mathbf{k})$ can be justified by the following idea [10]: When the field is turned off, the distribution must return to equilibrium after a characteristic time $\tau$, which means that $g_n(\mathbf{k})$ decays to 0

$$-\frac{\partial g_n(\mathbf{k})}{\partial t} = \frac{g_n(\mathbf{k})}{\tau}. \tag{3.70}$$

With this, we can make the ansatz linear in the applied electric field $\boldsymbol{\mathcal{E}}$ [12]

$$g_n(\mathbf{k}) = e\frac{\partial f^0(\epsilon(\mathbf{k}))}{\partial \epsilon(\mathbf{k})}\boldsymbol{\Lambda}_n(\mathbf{k}) \cdot \boldsymbol{\mathcal{E}}. \tag{3.71}$$

Here, $\epsilon(\mathbf{k})$ is the band dispersion. The vector mean free path $\boldsymbol{\Lambda}_n(\mathbf{k})$ is determined via the self-consistent equation [12, 38]

$$\boldsymbol{\Lambda}_n(\mathbf{k}) = \tau_n(\mathbf{k})\left(\mathbf{v}_n(\mathbf{k}) + \sum_{\mathbf{k}',n'}P_{\mathbf{k}\mathbf{k}'}^{nn'}\boldsymbol{\Lambda}_n(\mathbf{k}')\right). \tag{3.72}$$

Here, $\mathbf{v}_n(\mathbf{k})$ is the group velocity of band $n$, and the characteristic time $\tau_n(\mathbf{k})$ can be interpreted as the time between two scattering events, therefore it will be called scattering time[5]. The second part, $\sum_{\mathbf{k}',n'}P_{\mathbf{k}\mathbf{k}'}^{nn'}\boldsymbol{\Lambda}_n(\mathbf{k}')$, is the so-called scattering in-term which describes the skew or Mott scattering within the spin Hall effect [38].

The scattering time $\tau$ is calculated via the transition rates [12, 38]

$$\frac{1}{\tau(\mathbf{k})_n} = \sum_{\mathbf{k}',n'}P_{\mathbf{k}'\mathbf{k}}^{nn'}. \tag{3.73}$$

With the knowledge of the vector mean free path $\boldsymbol{\Lambda}_n(\mathbf{k})$, the charge conductivity tensor $\underline{\sigma}$ can be calculated as an integral over the Fermi surface [8, 38] in the form of an response tensor for $\mathbf{j} = \underline{\sigma}\boldsymbol{\mathcal{E}}$ as

$$\underline{\sigma} = \frac{e^2}{\hbar}\frac{1}{(2\pi)^3}\sum_n\iint_{\epsilon(\mathbf{k})=E_F}\frac{\mathrm{d}S_n}{|\mathbf{v}_n(\mathbf{k})|}\mathbf{v}_n(\mathbf{k}) \circ \boldsymbol{\Lambda}_n(\mathbf{k}), \tag{3.74}$$

---

[5]Sometimes $\tau$ is also called relaxation time

where $\mathrm{d}S_n$ is an infinitesimal element of the Fermi surface. In analogy, many different quantities, such as spin conductivity, spin accumulation, spin torque, and spin flux can be calculated. The spin accumulation response reads [12]

$$\underline{\chi} = \frac{e\mu_B}{\hbar} \frac{1}{(2\pi)^3} \sum_n \iint_{\epsilon(\mathbf{k})=E_F} \frac{\mathrm{d}S_n}{|\mathbf{v}_n(\mathbf{k})|} \langle \mathbf{s}_n \rangle (\mathbf{k}) \circ \boldsymbol{\Lambda}_n(\mathbf{k}), \tag{3.75}$$

where $\langle \mathbf{s}_n \rangle$ is the expectation value of the spin operator, and the spin conductivity reads [38]

$$\underline{\sigma}^s = \frac{e^2}{\hbar} \frac{1}{(2\pi)^3} \sum_n \iint_{\epsilon(\mathbf{k})=E_F} \frac{\mathrm{d}S_n}{|\mathbf{v}_n(\mathbf{k})|} \langle s_{z,n} \rangle (\mathbf{k}) \mathbf{v}_n(\mathbf{k}) \circ \boldsymbol{\Lambda}_n(\mathbf{k}), , \tag{3.76}$$

where $\langle s_{z,n} \rangle$ is the expectation value of the $z$ component of the spin operator.

### 3.3.1. Relation to moments

From the generalized transport coefficients [37, 41]

$$\underline{L}_n = \frac{2e}{V} \sum_{\mathbf{k}} \tau_{\mathbf{k}} \mathbf{v}_{\mathbf{k}} \circ \mathbf{v}_{\mathbf{k}} \, (\epsilon(\mathbf{k}) - \mu)^n \left( -\frac{\partial f}{\partial \epsilon}(\mathbf{k}) \right) \tag{3.77}$$

within the Boltzmann formalism, we see that $\underline{\sigma} = e\underline{L}_0 \sim \tau_{\mathbf{k}}$.

Restricting the discussion to only the diagonal elements, especially for the transport direction $z$, and applying the constant scattering time relation $\tau(\mathbf{k}) \equiv \tau$, it follows that the Seebeck coefficient $S = -\frac{1}{e\theta} \frac{L_1}{L_0}$ is independent of the scattering time $\tau$.

## 3.4. Spin Hall Effect

### 3.4.1. Introduction

The spin Hall effect is one of several Hall-type effects of the Hall effect family [42–46]. As in other types of Hall effects, the spin Hall effect generates a transversal spin current when a longitudinal charge current is applied [47–54]. This pure spin current divides the two different spin species to either side of a thin film of a material and a spin accumulation on the surface can be observed. The accumulation was first observed by Kato et. al. [55] and Wunderlich et. al. [56] in semiconductor systems. The resulting spin current to the surface can be injected into a device to make use of the pure spin current generated by spin Hall effect [57, 58]. The inverse effect can be used to detect pure spin currents in non-local measurement geometries [59–61]. Another application is the use in magnetic switching junctions, where the accumulation can induce the switching of a magnetic layer by spin-transfer torque [62, 63]. The application of spin torque, which relies on the spin accumulation at the sample interface has attracted vast interest recently [12, 14, 15, 64, 65].

While an applied magnetic field is necessary for the Hall effect to work, the spin Hall effect arises from the intrinsic spin-orbit coupling of the material or spin-dependent scattering caused by impurities or disorder. Most commonly, the contributions of the spin Hall effect are divided into two contributions, the intrinsic [66–69] and the extrinsic contribution [70–72].

In semi-classical theory, the intrinsic spin Hall effect is described via the Berry curvature [68, 73, 74] and the extrinsic spin Hall effect via a Boltzmann equation incorporating the vertex corrections (scattering-in term) [38, 75, 76]. In a full quantum mechanical approach, the Kubo or Kubo-Streda (Kubo-Bastin) formalism has been used to consider the intrinsic mechanism [6, 7], while extrinsic mechanisms were considered via the coherent potential approximation (CPA) [5].

However, most theoretical studies consider only the spin conductivity in a bulk system [77–79], but ignore the influence of surfaces completely. Often DFT studies rely on semi-classical approaches like the Boltzmann approach. Quantum mechanical studies based on the non-equilibrium Green's function formalism exist, but they mostly just use model Hamiltonians like the Rashba model Hamiltonian [80–83]. Up to now, there are no fully quantum mechanical approaches that treat the intrinsic effect in the framework of density functional theory within the Keldysh Green's function approach.

### 3.4.2. Contributions to the Spin Hall Effect

#### Intrinsic

The intrinsic contribution, that was described in Ref. [73] for the anomalous Hall effect first, is caused by the spin-orbit coupling in the crystal, without contributions from impurities, but only from the band structure, more precisely interband effects [66, 69, 73, 84], of the perfect crystal. The contribution is caused by an additional velocity contribution, which is called the anomalous velocity. The full velocity reads

$$\mathbf{v}(\mathbf{k}) = \frac{1}{\hbar}\frac{\partial E(\mathbf{k})}{\partial \mathbf{k}} + \frac{e}{\hbar}\mathcal{E} \times \mathbf{\Omega}(\mathbf{k}), \tag{3.78}$$

where the second part is the anomalous velocity and $\mathbf{\Omega}(\mathbf{k})$ is the Berry curvature. This velocity appears naturally in the full-quantum mechanical Kubo formalism as off-site elements in the velocity tensor [85]. In the Boltzmann formalism, this velocity contribution has to be reintroduced via the Berry curvature, which ultimately considers inter-band contributions [84, 85] that were neglected during the derivation of formulas in the Boltzmann approach [86]. The Berry curvature appears as a consequence of not considering every band but a sub-set of bands only for the wave packet of the electron [86]. In the picture of the Berry curvature, a magnetic monopole-like term in $\mathbf{k}$-space appears at so-called diabolic points where random band crossings occur [86]. This monopole can be seen as a pictorial description of the effects of spin-orbit coupling. In the Keldysh method used in the full-relativistic KKR approach, only contributions from the band structure arise. The information about the band structure and the resulting electronic charge and magnetization densities is completely contained in the Green's function. The Berry curvature, therefore, is not to be considered explicitly as the contributions arise naturally.

#### Extrinsic

The extrinsic contribution is caused by contributions from two mechanisms, the skew [71] or Mott scattering [87, 88] and the side jump scattering [89].

The process of skew scattering is mediated by spin-dependent scattering. Based on the direction of spin of the electron, it gets scattered to either direction transverse to its direction of motion [69], which leads to an accumulation on the surface of the sample.

|  | $\propto \tau^0 \;/\; \propto n_0^0$ | $\propto \tau^1 \;/\; \propto n_0^{-1}$ |
|---|---|---|
| no impurities | intrinsic | – |
| impurities | side jump (extr./intr.) | skew (extr.) |
|  | skew (intr.) |  |

Table 3.1.: Distinction of contributions to the spin Hall effect after Refs. [69, 85].

The skew scattering contribution is included via vertex corrections in the Boltzmann equation, which are included via the scattering-in term [38].

The side jump scattering at a magnetic impurity causes the center of an incoming wave packet to be displaced transversely to the direction of motion [69].

This displacement is included in the Boltzmann Eq. 3.68 via a displacement term $\delta \mathbf{r}_{\mathbf{k'k}}$ and adds another contribution to the velocity [85], such that it reads [39, 84]

$$\mathbf{v}(\mathbf{k}) = \frac{1}{\hbar}\frac{\partial E(\mathbf{k})}{\partial \mathbf{k}} + \frac{e}{\hbar}\mathcal{E} \times \mathbf{\Omega}(\mathbf{k}) + \sum_{\mathbf{k'}} P_{\mathbf{k'k}}\delta\mathbf{r}_{\mathbf{k'k}}. \tag{3.79}$$

The Keldysh method within the full-relativistic KKR formalism employed in this work does not account for any contributions arising from disorder or scattering at impurities. Impurities would have to be considered explicitly, however, the implementational details are not clear yet. To consider the effects of temperature, such as phonon scattering, the virtual terminal method introduced in Sec. 3.1.6 can be used. To include the virtual terminals in the full-relativistic Keldysh approach, new contributions to the electronic density and the magnetic density arising from each virtual terminal must be accounted for. Such contributions are of the form[6] $n \propto G\Gamma_\alpha G^\dagger$, where $\Gamma_\alpha$ is the broadening function at virtual terminal $\alpha$. The detailed form in the full-relativistic case remains to be evaluated.

**Distinction due to $\tau$**

Instead of dividing the contributions into intrinsic and extrinsic, the distinction can be made by the dependence on the transport lifetime $\tau$ [69] and subsequently the impurity concentration $n_0$ [85]. The contribution due to skew scattering is proportional to $\tau^1$. The intrinsic and the side jump contributions are proportional to $\tau^0$, that is, they are independent of $\tau$ [69]. The side jump contribution can be split into two contributions. The extrinsic one in which the non-spin-orbit coupled part of the wave packet scatters at the spin-orbit-coupled disorder and the intrinsic part in which the spin-orbit coupled part of the wave packet scatters at the scalar potential of the impurity without spin-orbit coupling. However, both contributions depend on the crystal and the impurity [69]. Then there is also a part of the skew scattering, which is similar to the side jump scattering and is proportional to $n_0^0$, that is, a constant, therefore termed intrinsic skew scattering contribution [85]. The different contributions are summarized in Tab. 3.1.

### 3.4.3. Experimental Detection and Theoretical Description

Experimentally, the spin Hall effect can be detected optically via the magneto-optical Kerr effect (MOKE) or electronically via non-local measurements. The samples used

---

[6]Written here not in the mathematically strict exact form.

are not bulk-like materials but rather thin films in various Hall-like geometries and bi-layer systems [12, 14, 15, 64, 65]. Additionally, in bi-layer systems it is difficult to distinguish between the different origins of contributions [90, 91]. The NM-FM interface of different magnetic materials can significantly influence the resulting magnetization at the surface. The main important fact is the finite size of the sample and the interfaces. Further, the effect is sometimes detected indirectly by the inverse spin Hall effect or by fitting the magnetization profile obtained by MOKE via spin diffusion theory to extract the desired quantities [55, 92, 93].

On the other hand, in most of the theoretical treatments, the spin Hall effect is described in terms of the spin conductivity $\sigma_s$, which is calculated from bulk systems [77–79]. Thus, effects of surfaces or interfaces are not included, which makes a comparison between theory and experiment all the more difficult. There are works implementing ab initio theory based on the semi-classical Boltzmann description for bilayer systems [12] and works implementing the full-quantum mechanical approach to a model Hamiltonian [82, 83]. This work goes a step further by using the full-quantum mechanical non-equilibrium Green's function approach with the ab initio Korringa-Kohn-Rostoker method.

An easy-to-overlook point is the comparison of values between different experiments. Due to the different methods like injection of spins, different materials or thicknesses in conjunction with the system under consideration, and different amounts of impurities in the samples, the results for the spin Hall angle or spin Hall conductivity may differ significantly. This can be seen in a compilation of Ref. [69].

This makes the comparison of especially intrinsic values achieved in this work difficult. We, therefore, rely on the comparison with one experiment only and the trends between the elements therein since the absolute values might differ strongly. The experimental results chosen here are from [94].

### 3.4.4. Fermi Sea and Fermi Surface Term

When evaluating the Kubo-Bastin formula [15, 64] for example for the torkance $t_{\mu\nu}$,

$$t_{\mu\nu} = -\frac{\hbar}{4\pi} \int_{-\infty}^{\infty} dE \frac{df(E,\mu,\theta)}{dE} \text{Tr} \left\langle \hat{T}_\mu (G^+ - G^-) \hat{j}_\nu G^- - \hat{T}_\mu G^+ \hat{j}_\nu (G^+ - G^-) \right\rangle \quad (3.80)$$

$$+ \frac{\hbar}{4\pi} \int_{-\infty}^{\infty} dE f(E) \text{Tr} \left\langle \left( \hat{T}_\mu G^+ \hat{j}_\nu \frac{dG^+}{dE} - \hat{T}_\mu \frac{dG^+}{dE} \hat{j}_\nu G^+ \right) \right. \quad (3.81)$$

$$\left. - \left( \hat{T}_\mu G^- \hat{j}_\nu \frac{dG^-}{dE} - \hat{T}_\mu \frac{dG^-}{dE} \hat{j}_\nu G^- \right) \right\rangle$$

$$= t_{\mu\nu}^I + t_{\mu\nu}^{II}, \quad (3.82)$$

where $\mu$, $\nu$ are indices of the full torkance tensor $\underline{t}$, $f(E,\mu,\theta)$ is the Fermi-Dirac distribution, $G^{+/-}$ is the retarded and advanced Green's function, respectively, $\hat{T}_\mu$ is the $\mu$-th component of the torque operator, and $\hat{j}_\mu$ is the $\mu$-th component of the electric current density operator, it becomes apparent that there are two contributions. Here, $t_{\mu\nu}^I$ originates from the Fermi surface only and $t_{\mu\nu}^{II}$ originate from the occupied valence states, that is the Fermi sea [15]. The torkance can also be split into an even and odd under magnetization reversal part. In this case, the odd part of the torkance is caused exclusively by the Fermi surface terms. The even part is caused by both, Fermi surface and Fermi sea terms [15].

Similarly, to this differentiation, in this work we focus on the odd under magnetization reversal part of the spin accumulation, which is caused by the Fermi surface term. This facilitates the comparison between the Keldysh and Boltzmann results done here.

In principle, the inclusion of Fermi sea terms should work by using the full Keldysh contour, that is the full semicircular contour in equilibrium formalism as well as energy points in the according bias window evaluated via the non-equilibrium formalism.

For fcc Pt, the contributions from the Fermi sea proved to be zero and only Fermi surface contributions exist in the one-shot calculations. However, after doing a full self-consistency for the complete Keldysh contour in transport geometry and consequently shifting the potentials, naturally, contributions from the equilibrium contour part and the non-equilibrium contour part will occur. This is further discussed in Appendix D

### 3.4.5. Spin Hall Effect in KKR

The spin Hall effect in the KKR described here is based on the steady-state Keldysh formalism in the full-relativistic framework. We consider here contributions that are caused by the band structure but not from effects of disorder or impurities. To evaluate the applicability of the method we employ here, we calculate the Fermi surface driven contribution and compare it to a semi-classical Boltzmann approach. In principle, a fully self-consistent cycle is possible with the combined contour in Sec. 3.1.2 and the full density after Eq. 3.84 is calculated. After self-consistency is achieved, the magnetic moment or accumulation is calculated via Eq. 3.85.

One short note should be given here. While in the Boltzmann approach the origin of contributions to the spin Hall effect can be traced to their physical origin as a result of the physically graphic description, the fully quantum mechanical approaches like the Kubo- or Keldysh formalism often "hide the physical origin of elementary microscopic processes" [85].

### 3.4.6. Spin accumulation

To calculate the contributions to the $i$-th magnetization density component $m_i(\mathbf{r})$, where $i = x, y, z$, from the non-equilibrium part, the magnetization density has to be evaluated within the full-relativistic formalism as (similar to Eq. 3.25 and Eq. A.108)

$$m_i^{\mathrm{NEQ}}(\mathbf{r}) = \frac{\mu_{\mathrm{B}}}{2\pi} \int_{\mu_<}^{\mu_>} \langle\mathbf{r}| \mathrm{Tr}\Big(G\Gamma_\iota G^\dagger \underline{\beta}\,\underline{\Xi}_i\Big) |\mathbf{r}\rangle \ \mathrm{d}E, \qquad (3.83)$$

where $\mu_< = \min(\mu_R, \mu_L)$ and $\mu_> = \max(\mu_R, \mu_L)$, $\mu_{L/R}$ the left and right chemical potential respectively, $\underline{\beta}$ is defined in Eq. A.100 and $\underline{\Xi}_i$ from Eq. A.97. To make a full self-consistent cycle, the complete full-relativistic density has to be used:

$$\begin{aligned} n(\mathbf{r}) = &- \frac{\mu_{\mathrm{B}}}{\pi} \, \mathrm{Im} \oint_{E_B}^{\mu_<} \langle\mathbf{r}| \mathrm{Tr}\left(G(z)\mathbb{1}_4\right) |\mathbf{r}\rangle \ \mathrm{d}z \\ &+ \frac{\mu_{\mathrm{B}}}{2\pi} \int_{\mu_<}^{\mu_>} \langle\mathbf{r}| \mathrm{Tr}\left(G(E)\Gamma_\iota G(E)^\dagger \mathbb{1}_4\right) |\mathbf{r}\rangle \ \mathrm{d}E. \end{aligned} \qquad (3.84)$$

With this, it is possible to calculate the contributions of the intrinsic spin Hall effect to the accumulation self consistently as

$$
m_i(\mathbf{r}) = -\frac{\mu_B}{\pi} \operatorname{Im} \oint_{E_B}^{\mu_<} \langle \mathbf{r}| \operatorname{Tr}\big(G(z)\underline{\beta}\underline{\Xi}_i\big) |\mathbf{r}\rangle \ \mathrm{d}z
$$
$$
+ \frac{\mu_B}{2\pi} \int_{\mu_<}^{\mu_>} \langle \mathbf{r}| \operatorname{Tr}\Big(G(E)\Gamma_\iota G(E)^\dagger \underline{\beta}\underline{\Xi}_i\Big) |\mathbf{r}\rangle \ \mathrm{d}E. \tag{3.85}
$$

Exemplary results are given in Appendix D for a thin slab of Pt.

The results shown in PHYS. REV. B **104**, 054402, (2021) are calculated only at the Fermi surface, for which Eq. 3.85 reduces to

$$
m_i(\mathbf{r}) = \frac{\mu_B}{2\pi} \langle \mathbf{r}| \left(G(E_F)\Gamma_\iota G(E_F)^\dagger \underline{\beta}\underline{\Xi}_i\right) |\mathbf{r}\rangle \, e\varphi. \tag{3.86}
$$

From this, the accumulation can be calculated via Eq. A.109.
The calculations in PHYS. REV. B **104**, 054402, (2021) are not done self-consistently in the non-equilibrium formalism. The potential used here stems from equilibrium self-consistent supercell calculations.

# 4. Results

## 4.1. Publication Phys. Rev. B 104, 054402, (2021)

The spin Hall effect has gained a lot of interest because of its ability to convert charge to spin current and vice versa. Especially, the spin accumulation has drawn the attention to it since the spin-orbit torque is significantly influenced by the spin accumulation and spin currents through normal metal ferromagnet interfaces [12, 14, 15, 64, 65]. The challenging point here lies in the fact that many works calculate the spin conductivity of a bulk material [77–79], but the experimental reality comprises surfaces and spin accumulations. Therefore, the first goal was here to obtain a description of the spin accumulation for a series of metals that is closer to the experimental reality in terms of the thin film nature of actual samples. The second goal was to employ a full quantum mechanical method in the framework of the KKR density functional theory to go a step beyond the semi-classical Boltzmann theory [12] and model systems [82, 83]. To assess the validity of the results, we compared the Keldysh values with the Boltzmann values. For comparing the Keldysh and Boltzmann values, we took the odd under spatial magnetization reversal component of the accumulation evaluated at the Fermi surface. We found a remarkable agreement between the two methods as well as with the experiment for the general trend within a series of metals. The two methods differ in thicker thin-film structures especially for systems with complex Fermi surfaces. This is discussed in the Supplemental Information in Appenidx B.
The work is a first step, which can be expanded upon in the future to include effects of impurities, even under magnetization reversal contributions or effects of spin relaxation within phase-breaking scattering.

The manuscript was written by me and edited by all co-authors. The calculation of the Keldysh values for the spin accumulation and of the finite current density originating from the contact resistance were carried out by me. The Boltzmann calculations for the spin accumulation were carried out by Hugo Rossignol, Ming-Hung Wu, and Martin Gradhand. To calculate all contributions from the Fermi sea and the Fermi surface, the self-consistent cycle in the KKR code was expanded after Ref. [13] by me. However, this expansion was not used in this publication to facilitate the comparison between Boltzmann and Keldysh formalism. Results of the full self-consistent cycle are shown in Appendix D for a Pt thin film exemplary.

The article is reprinted with permission from

# Spin accumulation from nonequilibrium first principles methods

Alexander Fabian,[*] Michael Czerner, and Christian Heiliger

*Institute for Theoretical Physics, Justus Liebig University Giessen, Heinrich-Buff-Ring 16, 35392 Giessen, Germany*
*and Center for Materials Research (LaMa), Justus Liebig University Giessen, Heinrich-Buff-Ring 16, 35392 Giessen, Germany*

Hugo Rossignol and Ming-Hung Wu

*HH Wills Physics Laboratory, University of Bristol, Tyndall Avenue, Bristol BS8 1TL, United Kingdom*

Martin Gradhand

*HH Wills Physics Laboratory, University of Bristol, Tyndall Avenue, Bristol BS8 1TL, United Kingdom*
*and Institute of Physics, Johannes Gutenberg University Mainz, 55099 Mainz, Germany*

For the technologically relevant spin Hall effect, most theoretical approaches rely on the evaluation of the spin-conductivity tensor. In contrast, for most experimental configurations the generation of spin accumulation at interfaces and surfaces is the relevant quantity. Here, we directly calculate the accumulation of spins due to the spin Hall effect at the surface of a thin metallic layer, making quantitative predictions for different materials. Two distinct limits are considered, both relying on a fully relativistic Korringa-Kohn-Rostoker density functional theory method. In the semiclassical approach, we use the Boltzmann transport formalism and compare it directly with a fully quantum mechanical nonequilibrium Keldysh formalism. Restricting the calculations to the spin-Hall-induced, odd-in-spatial-inversion, contribution in the limit of the relaxation time approximation, we find good agreement between the two methods, where deviations can be attributed to the complexity of Fermi surfaces. Finally, we compare our results with experimental values of the spin accumulation at surfaces as well as the Hall angle and find good agreement for the trend across the considered elements.

## I. INTRODUCTION

The spin Hall effect was first proposed in 1971 by Dyakonov and Perel [1]. Only after Hirsch [2] re-established the concept in 1999 was it experimentally observed directly in semiconductors by Kato *et al.* [3] and Wunderlich *et al.* [4]. The spin Hall effect enables the generation of spin current in nonmagnetic materials by passing an electric current through a system opening the route to various applications in spintronics [5–12]. Importantly, the inverse effect, generating a charge current from a spin current, or in fact a spin accumulation, gives a tool to detect spin currents electronically [13–15].

The origin of the effect is commonly divided into two contributions, the intrinsic [16–19] and the extrinsic mechanism. While the first derives from the intrinsic spin-orbit coupling of the pure material, the latter is mediated via spin-orbit coupling at an impurity site. For the extrinsic process, the skew or Mott scattering dominates in the dilute limit [20,21], and the side jump [22] scales similarly to the intrinsic mechanism with the sample resistivity.

One can approach the spin Hall effect theoretically typically via semiclassical or fully quantum mechanical approaches. In the case of the semiclassical theory, the intrinsic mechanism is recast in terms of the Berry cur-

vature [18,23,24], and the extrinsic, almost exclusively the skew scattering mechanism, is considered via a Boltzmann equation incorporating the vertex corrections (scattering-in term) [25–27]. On the other hand, the Kubo or Kubo-Streda (Kubo-Bastin) formalism has been used to consider the intrinsic mechanism [28,29], or in combination with the coherent potential approximation the extrinsic mechanisms were included on an equal footing [30]. However, all approaches have in common that they almost exclusively calculate the spin Hall conductivity in a periodic crystal [31–33], giving no direct access to the spin accumulation at surfaces or interfaces. In contrast, most experimental configurations will rely on the accumulation at interfaces and surfaces exploiting spin diffusion equations in order to extract the spin Hall conductivity [3,34,35]. However, the induced spin accumulation has attracted renewed interest as the technologically relevant spin-orbit torque often relies on spin accumulation at, as well as spin currents through, normal metal ferromagnet interfaces [36–40]. Experimentally, it is incredibly difficult to distinguish the various contributions, rendering it a challenge to optimize spin-orbit materials and the corresponding bilayer systems [41,42].

In this paper, we directly calculate the spin accumulation induced at the surfaces of metallic thin films when a charge current is passed through the sample. We focus on the contributions with the same symmetry as the spin Hall effect, namely, the spin accumulation which is odd under spatial

---

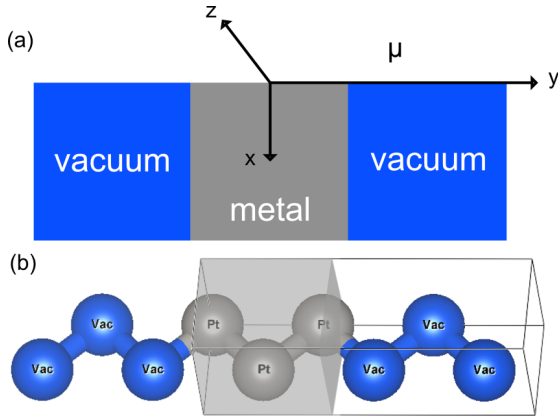[*]Alexander.Fabian@physik.uni-giessen.de

FIG. 1. (a) Schematic drawing of the slab systems for the Keldysh formalism. The atomic index counts the atoms along the $y$ direction. (b) Actual unit cell for fcc Pt. For the Keldysh formalism the box indicates the supercell. For the Boltzmann formalism the vacuum is extended into the semi-infinite half-spaces on both sides of the slab (not shown).

inversion [36–38], showing equal and opposite spin accumulations at the two surfaces of the thin metallic film. For that reason, we deliberately omit the even-under-spatial-inversion part of the accumulation. This will allow us to make contact with experimental observations and theoretical predictions of the spin Hall effect in more realistic geometries. The system is shown in Fig. 1(a), where a charge current is driven in the $z$ direction, the spin is pointing along $x$, and the accumulation is calculated in the $y$ direction perpendicular to the plane of the thin film. As the atomic configuration is preserving inversion symmetry and we focus on the contributions from the clean system, it is the Fermi-surface-driven and odd-under-spatial-inversions contribution [36,37], which is linear in the applied longitudinal current, for which we make quantitative predictions in a series of metallic systems. On the one hand, we go beyond the semiclassical approach [38] previously applied to bilayer systems using a fully quantum mechanical Keldysh formalism based on nonequilibrium Green's functions. On the other hand, we apply this formalism to real materials in a fully *ab initio* density functional theory (DFT) framework going a step further than earlier works on the spin accumulation in nonequilibrium description which were restricted to a model Hamiltonian [43,44]. To validate our method, we compare it with a semiclassical approach relying on the Boltzmann formalism.

After a brief introduction of both methods we will present exemplary results and compare the induced spin accumulation with experimental findings. Furthermore, we will analyze the common trends across the elements with respect to the charge-to-spin-current conversion efficiency.

## II. THEORY

The electronic structure is calculated via a fully relativistic Korringa-Kohn-Rostoker (KKR) density functional theory method [45]. Both band structure methods, for the semiclassical approach [46,47] and the Keldysh formalism [48–50], have been introduced earlier. Here, we only highlight the

adjustments and relevant expressions used to express the steady-state magnetization density.

### A. Keldysh formalism

For the Keldysh formalism the system is divided into three parts, the left (L), center (C), and right (R) regions. The left and right parts work as semi-infinite leads in equilibrium with the same Fermi levels $E_F$. Their influence on the center region is accounted for by the corresponding self-energies $\Sigma_{L/R}$. When applying a bias voltage, the levels of the chemical potential change to $\eta_{>/<} = E_F \pm \frac{e\Delta\varphi}{2}$ accordingly. In the range of $[\eta_<, \eta_>]$ the fully relativistic electron density and magnetization density are calculated as [45]

$$\rho(\vec{r}) = \frac{1}{2\pi} \int_{\eta_<}^{\eta_>} \langle \vec{r} | \text{Tr}[G(E)\Gamma(E)G^{\dagger}(E)] | \vec{r} \rangle \, dE, \quad (1)$$

$$m^{(i)}(\vec{r}) = \frac{\mu_B}{2\pi} \int_{\eta_<}^{\eta_>} \langle \vec{r} | \text{Tr}[\beta \varsigma_i G(E)\Gamma(E)G^{\dagger}(E)] | \vec{r} \rangle \, dE, \quad (2)$$

respectively. Here, $G(E)$ is the Green's function of the center area, and $\Gamma = i[\Sigma(E) - \Sigma^{\dagger}(E)]$ is the broadening function, where $\Sigma(E) = \Sigma_L(E) + \Sigma_R(E)$,

$$\beta = \begin{pmatrix} I_2 & 0 \\ 0 & -I_2 \end{pmatrix}, \quad \varsigma_i = \begin{pmatrix} \sigma_i & 0 \\ 0 & \sigma_i \end{pmatrix},$$

$I_2$ is the $2 \times 2$ unity matrix, and $\sigma_i$ are the Pauli spin matrices with $i \in \{x, y, z\}$. In the so-called one-shot calculations, only the magnetization at the Fermi level is considered for vanishing bias voltage, which is

$$m_i(\vec{r}) = \frac{\mu_B}{2\pi} \text{Tr}[\beta \varsigma_i G(E_F)\Gamma(E_F)G^{\dagger}(E_F)] e\Delta\varphi.$$

Finally, the magnetic moment due to spin accumulation $a_x(\mu)$ is evaluated by integrating $m_x(\vec{r})$ over the volume $V_\mu$ of the atomic sphere at atomic index $\mu$:

$$a_x(\mu) = \int_{V_\mu} m_x(\vec{r}) \, dV. \quad (3)$$

The current density is calculated via the Landauer-Büttiker formula in the case of a vanishing bias voltage [51]

$$j_z = \frac{e^2}{A\hbar} T(E_F)\Delta\varphi \quad (4)$$

assuming that the transmission $T(E) = \text{Tr}[\Gamma_L G \Gamma_R G^{\dagger}]$ is nearly constant in the range of $\Delta E = e\Delta\varphi$. Here, $A$ is the area of the supercell in the $x$ and $y$ directions.

### B. Boltzmann formalism

Within the Boltzmann formalism the spin accumulation is expressed as a Fermi surface integral [38]. For two-dimensional (2D) systems the spin accumulation is expressed as [52]

$$\vec{a} = \underline{\chi}_\mu \cdot \vec{E} = -\frac{e\mu_B}{\hbar} \frac{V}{d(2\pi)^2} \int_{E_F} \frac{dl}{|\vec{v}_{\vec{k}}|} (\vec{s}_{\vec{k}}(\mu) \circ \tau_{\vec{k}} \vec{v}_{\vec{k}}) \cdot \vec{E}, \quad (5)$$

where $V$ is the volume of the cell, $d$ is the thickness of the film, $v_{\vec{k}}$ is the group velocity at $\vec{k}$, $\vec{s}_{\vec{k}}$ is the expectation value of the spin operator, and $\vec{E}$ is the applied electric field.

Because of degenerate states, the spin operator exhibits off-diagonal elements. A gauge transformation is applied, such that these off-diagonal elements vanish. The current density is given by

$$\vec{j} = \underline{\sigma} \cdot \vec{E} = -\frac{e^2}{\hbar} \frac{1}{d(2\pi)^2} \int_{E_F} \frac{dl}{|\vec{v}_{\vec{k}}|} (\vec{v}_{\vec{k}} \circ \tau_{\vec{k}} \vec{v}_{\vec{k}}) \cdot \vec{E}. \quad (6)$$

Importantly, both scale linearly with the relaxation time. In the chosen geometry, $\vec{j} = j\vec{e}_z$ and $\vec{E} = E_z\vec{e}_z$, and by using the relaxation time approximation $\tau_{\vec{k}} = \tau$, the relevant expressions can be simplified as

$$a_x(\mu) = \chi_{xz} E_z = \frac{e}{\hbar} \frac{\mu_B V \tau E_z}{d(2\pi)^2} \int_{E_F} \frac{dl}{|\vec{v}_{\vec{k}}|} s_{x,\vec{k}}(\mu) v_{z,\vec{k}} \quad (7)$$

and

$$j_z = \frac{e^2}{\hbar} \frac{\tau E_z}{d(2\pi)^2} \int_{E_F} \frac{v_{z,\vec{k}} v_{z,\vec{k}}}{|\vec{v}_{\vec{k}}|} dl = \frac{e^2}{\hbar} \frac{\tau E_z}{d(2\pi)^2} \langle v_z^2 \rangle. \quad (8)$$

This maneuver will allow us to remove the direct dependence of the spin accumulation on the relaxation time $\tau E_z$, replacing it with the current density

$$\frac{a_x(\mu)}{\mu_B} = \frac{j_z}{e} \frac{V}{\langle v_z^2 \rangle} \int_{E_F} \frac{dl}{|\vec{v}_{\vec{k}}|} s_{x,\vec{k}}(\mu) v_{z,\vec{k}}. \quad (9)$$

Thus the spin accumulation will scale linearly with the current density, which, in turn, can be calculated within the Keldysh formalism. This will allow for direct mapping between the two methods.

### C. Computational details

For the Keldysh formalism the starting point consists of self-consistently calculated equilibrium potentials, which are obtained in a supercell approach including atomic spheres and vacuum spheres to form the thin film geometry. For the transport calculations, the supercell is connected to semi-infinite leads from the left and right sides along the transport direction (z direction). The corresponding cells are schematically shown in Fig. 1. In the following, a one-step nonequilibrium Keldysh formalism at the Fermi energy is used to find the steady-state densities from these potentials. The applied

voltage is chosen to be reasonably small at $\Delta\varphi = 10^{-4}$ Ry/$e$, in order to agree with the approximation of vanishing applied electric field in the linear response regime as assumed in the Boltzmann approach.

For the Boltzmann formalism the construction is based on a slab calculation with semi-infinite vacuum attached perpendicular to the film. After obtaining the self-consistent potentials, the Fermi surface parameters such as the $\vec{k}$-resolved band velocities and spin expectation values are calculated to find the spin accumulation according to Eq. (9). Given the linear scaling of the spin accumulation with the current density in the Boltzmann formalism, we insert the current density found within the Keldysh approach to facilitate direct comparison.

Within the Landauer-Büttiker approach the finite conductance stems from a contact resistance at the interfaces of the leads. This contact resistance is also often referred to as Sharvin resistance [53]. Naturally, it does not depend on the length of the transport system; rather, it depends only on the number of available transport channels. In contrast, for the Boltzmann approach the contact resistance is ignored, and the whole resistance originates from scattering in the volume. In our comparison we adjust $j$ such that it fits the Sharvin resistance of the Landauer-Büttiker approach. As such, the mechanism for the finite currents is different in both approaches; however, the resulting current density itself is the same, driving the spin accumulation at the surfaces. We do not account for any extrinsic mechanisms; rather, we only account for contributions to accumulation arising from the electronic structure of the clean crystal.

As we apply a bias in the $z$ direction, the only relevant element of the spin accumulation in the considered cubic systems is $a_x(\mu)$, and for convenience we are going to omit the index $x$ in the following. The axes of the coordinate systems are aligned parallel to the $\langle 100 \rangle$ axes of the crystals.

### III. RESULTS AND DISCUSSION

The resulting spin accumulation $a(\mu)$ as a function of the atomic position index $\mu$ is shown in Fig. 2 for the fcc (Cu, Pt) [Fig. 2(a)] and bcc (Ta, U) [Fig. 2(b)] systems comparing
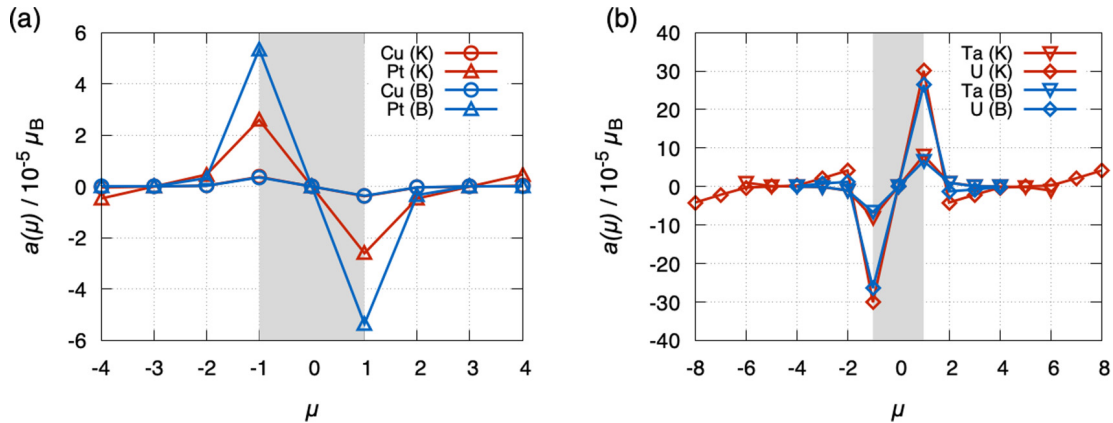


FIG. 2. Magnetic moment per atom for representative (a) fcc systems and (b) bcc systems. Blue refers to Keldysh (K) calculated values, and red refers to Boltzmann (B) calculated values. The thin film is highlighted in gray. Each line shows the same antisymmetric behavior. Note that in (a) the Keldysh and Boltzmann values for Cu overlap.

TABLE I. First extrema of the spin accumulation calculated by Boltzmann and Keldysh formalisms as well as the Keldysh current density for the small systems. Comparison between $a/j$ and spin Hall angle $\theta_{SH}^{exp}$ [54]. Intrinsic spin Hall conductivities from calculations are shown for reference.

| Element | $a(\mu = -1)$ $(10^{-6}\ \mu_B)$ | | $j$ $(10^{12}\ A/m^2)$ | $a/j$ $(10^{-17}\ \mu_B\ A^{-1}\ m^2)$ | | $\theta_{SH}^{exp}$ [54] (%) | $\sigma_{SH}^{theo}$ $[(\hbar/e)\ \Omega^{-1}\ cm^{-1}]$ |
|---|---|---|---|---|---|---|---|
| | Boltzmann | Keldysh | | Boltzmann | Keldysh | | |
| Cu (fcc) | 3.60 | 3.77 | 1.50 | 0.24 | 0.25 | 0.32 | |
| Ag (fcc) | 2.65 | 2.41 | 1.16 | 0.23 | 0.21 | 0.68 | |
| Au (fcc) | 17.62 | 16.33 | 1.33 | 1.32 | 1.23 | 8.4 | 400 [31] |
| Ta (bcc) | −66.19 | −80.99 | 1.17 | −5.66 | −6.92 | −7.1 | −142 [55] |
| Pd (fcc) | 31.33 | 10.10 | 1.12 | 2.80 | 0.90 | | 1400 [31] |
| Pt (fcc) | 53.53 | 25.99 | 1.79 | 2.99 | 1.45 | 10.00 | 2000 [17] |
| U (bcc) | −263.9 | −300.9 | 1.93 | −13.7 | −15.6 | | −402 [56] |

the Keldysh (K) and Boltzmann (B) formalisms, respectively. The position index is chosen such that the central atom of the film is labeled as 0. The general behavior is the same for all considered elements as well as between the two methods. This is largely enforced by symmetry since atoms $\mu = \pm 1$ have equal and opposite spin accumulation. For easier comparison we summarize the maximum spin accumulation $a(\mu = -1)$ for the various systems as well as the two methods in Table I. As expected, the spin accumulation increases with increasing atomic weight corresponding to enhanced spin-orbit coupling. While this is true in general, it is not correct in the details. The spin accumulation for Ag is smaller than that for Cu, and for Ta we find a surprisingly large spin accumulation. Such details would be difficult to predict from simplified models. Comparing the Boltzmann formalism with the Keldysh formalism, the agreement is perfect for the noble metals, with their simple Fermi surfaces, but starts to deviate for the more complex systems of Ta, Pd, Pt, and U. Nevertheless, the sign as well as the overall magnitude is still in remarkable agreement.

We believe this correlation between Fermi surface complexity (see Fig. S5 in the Supplemental Material [57]) and the agreement between the two methods not to be a numerical artifact. In the Keldysh formalism we only consider the ballistic transport, where each band contributes equally to the electronic transport. In contrast, the Boltzmann formalism relies on electron scattering, and the weighting in any Fermi surface integral will depend on the $\vec{k}$-dependent band velocity in the transport direction. For more complex structures the variations in the absolute value of the band velocity on the Fermi surface are much more pronounced (Ta, U, Pd, Pt) than for the simple metals Au, Ag, and Cu (see Fig. S5 in the Supplemental Material [57]). For elements with simple Fermi surfaces and subsequently the least-changing Fermi velocity, the results obtained within the Boltzmann formalism nevertheless match well.

So far we have considered rather thin layers with limited access to the decay length of the spin accumulation within the thin film. To investigate this point further, we consider three larger systems, Cu, Pt, and U, with nine layers of atoms (cf. Fig. 3 and also the Supplemental Material [57]). For Cu the decay of the spin accumulation is remarkably strong, happening within three layers, and is in excellent agreement between the two methods. In contrast, the decay appears to be much slower for Pt and even more so for U {see Fig. S3(c)

in the Supplemental Material [57]}, again consistent between the two methods.

In order to validate our results, we compare them with recent experiments where the spin accumulation of Pt thin films was directly measured by the magneto-optic Kerr effect (MOKE) [34]. In that experiment a strong thickness dependence was established with a value of $a/j = 5 \times 10^{-16}\ \mu_B\ A^{-1}\ m^2$ for samples with a thickness $t > 40$ nm. Extrapolating the experimental data Eq. (1) in Ref. [34] to the film thickness of $t = 0.39$ nm considered here yields a result of $a/j = 1.05 \times 10^{-17}\ \mu_B\ A^{-1}\ m^2$ in rather good agreement with our result of $a/j = 1.45 \times 10^{-17}\ \mu_B\ A^{-1}\ m^2$. While measurements of spin Hall angles and spin Hall conductivities are widely available, to our knowledge, such direct numerical measurements of the spin accumulation for other systems are very sparse. It is therefore difficult to compare the results from our methods directly with literature values. It appears natural to compare them with spin Hall conductivities or spin Hall angles predicted theoretically or measured experimentally. However, this holds multiple caveats. For example, theoretically predicted intrinsic conductivities are bulk calculations ignoring the fact that any spin accumulation will depend on the actual surface geometry and film thickness. While sign changes and overall magnitudes ought to be in agreement, significant variations are possible in the details. As summarized in Table I the signs are in agreement between
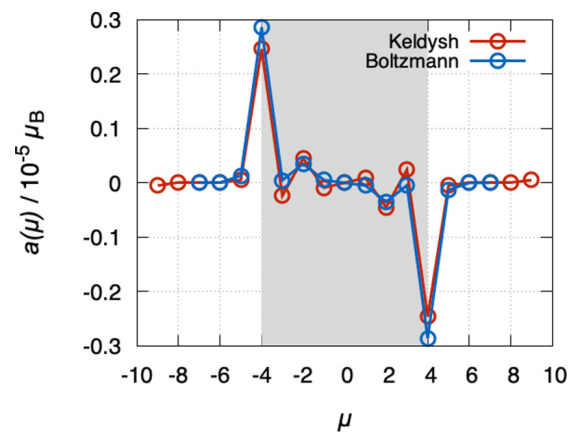


FIG. 3. Magnetization for a thin film of nine Cu atoms (highlighted in gray).

the spin accumulations and the intrinsic spin Hall conductivities, but the high spin accumulation for Ta and U cannot trivially be predicted from the conductivities. On the other hand, experimental results for the spin Hall angles tend to vary significantly over the various experimental techniques and sample preparations, which will often involve different nonmagnetic-ferromagnetic (NM-FM) interfaces [58] and varying degrees of extrinsic mechanisms contributing to the overall effect [59]. Consequently, any comparison should focus on one technique with similar sample preparation only. Choosing a spin pumping experiment in which most of the considered metals were investigated under similar conditions [54], the trend for $a/j$ and $\theta_{\text{SH}}^{\text{exp}}$ in Table I is quite consistent for systems with simpler Fermi surfaces (Cu, Ag, Au). Similarly, Ta, Au, and Pt show increasing spin Hall angles in the same order of magnitude, with a sign change occurring for Ta. This sign change cannot be trivially predicted for multibanded systems, since the spin-orbit coupling depends on the orbital and on the Fermi level [55].

tact with experiments, where instead of the conductivities derived from periodic crystals it is the spin accumulation at interfaces and surfaces as well as the spin current through interfaces which are the relevant driving mechanisms of, for example, magnetization reversal in ferromagnets. In this first and most important step we have established that the developed methodology reproduces the spin-Hall-induced spin accumulation in the thin metallic films well across different frameworks and in comparison to experiment. This will open up broad opportunities to explore the effect in more complex interfaces as well as under the influence of impurities, making even more direct contact with experimental realities. Incorporating inversion asymmetry and contributions even under spatial inversion symmetry [36,37] will give access to spin galvanic effects [60] while investigating the additional influence of impurities and the additional Mott scattering [39]. In all these cases, the full nonequilibrium description adds additional complexity with the possibility of finite bias across the sample geometry.

## IV. CONCLUSION

We extended existing theoretical frameworks to capture the spin-Hall-effect-induced spin accumulation in various metallic thin films via a fully nonequilibrium Keldysh formalism. We tested this new approach against a linearized Boltzmann approach as well as experimental findings and found remarkable agreement in all cases, reproducing all sign changes and predicting the same trends. Where the two theoretical approaches differ most is the atom-resolved spin accumulation in thicker films especially for systems with complex Fermi surfaces, whereas for Cu we find an excellent agreement. This methodology will enable us to make more direct con-

## ACKNOWLEDGMENTS

[1] M. I. Dyakonov and V. I. Perel, Phys. Lett. A **35**, 459 (1971).

[2] J. E. Hirsch, Phys. Rev. Lett. **83**, 1834 (1999).

[3] Y. K. Kato, R. C. Myers, A. C. Gossard, and D. D. Awschalom, Science **306**, 1910 (2004).

[4] J. Wunderlich, B. Kaestner, J. Sinova, and T. Jungwirth, Phys. Rev. Lett. **94**, 047204 (2005).

[5] S. Fukami, T. Anekawa, C. Zhang, and H. Ohno, Nat. Nanotechnol. **11**, 621 (2016).

[6] Y. V. Pershin, N. A. Sinitsyn, A. Kogan, A. Saxena, and D. L. Smith, Appl. Phys. Lett. **95**, 022114 (2009).

[7] A. Hoffmann, IEEE Trans. Magn. **49**, 5172 (2013).

[8] L. Liu, C.-F. Pai, Y. Li, H. W. Tseng, D. C. Ralph, and R. A. Buhrman, Science **336**, 555 (2012).

[9] Y. Kajiwara, K. Harii, S. Takahashi, J. Ohe, K. Uchida, M. Mizuguchi, H. Umezawa, H. Kawai, K. Ando, K. Takanashi, S. Maekawa, and E. Saitoh, Nature (London) **464**, 262 (2010).

[10] H. Nakayama, M. Althammer, Y.-T. Chen, K. Uchida, Y. Kajiwara, D. Kikuchi, T. Ohtani, S. Geprägs, M. Opel, S. Takahashi, R. Gross, G. E. W. Bauer, S. T. B. Goennenwein, and E. Saitoh, Phys. Rev. Lett. **110**, 206601 (2013).

[11] H. Wu, X. Zhang, C. H. Wan, B. S. Tao, L. Huang, W. J. Kong, and X. F. Han, Phys. Rev. B **94**, 174407 (2016).

[12] K. Ando, S. Takahashi, K. Harii, K. Sasage, J. Ieda, S. Maekawa, and E. Saitoh, Phys. Rev. Lett. **101**, 036601 (2008).

[13] S. O. Valenzuela and M. Tinkham, Nature (London) **442**, 176 (2006).

[14] H. Zhao, E. J. Loren, H. M. van Driel, and A. L. Smirl, Phys. Rev. Lett. **96**, 246601 (2006).

[15] E. Saitoh, M. Ueda, H. Miyajima, and G. Tatara, Appl. Phys. Lett. **88**, 182509 (2006).

[16] J. Sinova, D. Culcer, Q. Niu, N. A. Sinitsyn, T. Jungwirth, and A. H. MacDonald, Phys. Rev. Lett. **92**, 126603 (2004).

[17] G. Y. Guo, S. Murakami, T.-W. Chen, and N. Nagaosa, Phys. Rev. Lett. **100**, 096401 (2008).

[18] S. Murakami, Science **301**, 1348 (2003).

[19] J. Sinova, S. O. Valenzuela, J. Wunderlich, C. H. Back, and T. Jungwirth, Rev. Mod. Phys. **87**, 1213 (2015).

[20] J. Smit, Physica **21**, 877 (1955).

[21] J. Smit, Physica **24**, 39 (1958).

[22] L. Berger, Phys. Rev. B **2**, 4559 (1970).

[23] R. Karplus and J. M. Luttinger, Phys. Rev. **95**, 1154 (1954).

[24] T. Jungwirth, Q. Niu, and A. H. MacDonald, Phys. Rev. Lett. **88**, 207208 (2002).

[25] J. C. Swihart, W. H. Butler, G. M. Stocks, D. M. Nicholson, and R. C. Ward, Phys. Rev. Lett. **57**, 1181 (1986).

[26] P. Zahn, J. Binder, and I. Mertig, Phys. Rev. B **68**, 100403(R) (2003).

[27] M. Gradhand, D. V. Fedorov, P. Zahn, and I. Mertig, Phys. Rev. Lett. **104**, 186403 (2010).

[28] G. Y. Guo, Y. Yao, and Q. Niu, Phys. Rev. Lett. **94**, 226601 (2005).

[29] Y. Yao and Z. Fang, Phys. Rev. Lett. **95**, 156601 (2005).

[30] S. Lowitzer, M. Gradhand, D. Ködderitzsch, D. V. Fedorov, I. Mertig, and H. Ebert, Phys. Rev. Lett. **106**, 056601 (2011).

[31] G. Y. Guo, J. Appl. Phys. (Melville, NY) **105**, 07C701 (2009).

[32] X. Wang, J. R. Yates, I. Souza, and D. Vanderbilt, Phys. Rev. B **74**, 195118 (2006).

[33] Y. Yao, L. Kleinman, A. H. MacDonald, J. Sinova, T. Jungwirth, D.-s. Wang, E. Wang, and Q. Niu, Phys. Rev. Lett. **92**, 037204 (2004).

[34] C. Stamm, C. Murer, M. Berritta, J. Feng, M. Gabureac, P. M. Oppeneer, and P. Gambardella, Phys. Rev. Lett. **119**, 087203 (2017).

[35] S. Zhang, Phys. Rev. Lett. **85**, 393 (2000).

[36] F. Freimuth, S. Blügel, and Y. Mokrousov, Phys. Rev. B **90**, 174423 (2014).

[37] S. Wimmer, K. Chadova, M. Seemann, D. Ködderitzsch, and H. Ebert, Phys. Rev. B **94**, 054415 (2016).

[38] G. Géranton, B. Zimmermann, N. H. Long, P. Mavropoulos, S. Blügel, F. Freimuth, and Y. Mokrousov, Phys. Rev. B **93**, 224420 (2016).

[39] D. Ködderitzsch, K. Chadova, and H. Ebert, Phys. Rev. B **92**, 184415 (2015).

[40] A. Kosma, P. Rüßmann, S. Blügel, and P. Mavropoulos, Phys. Rev. B **102**, 144424 (2020).

[41] M. Yang, K. Cai, H. Ju, K. W. Edmonds, G. Yang, S. Liu, B. Li, B. Zhang, Y. Sheng, S. Wang, Y. Ji, and K. Wang, Sci. Rep. **6**, 20778 (2016).

[42] C. O. Avci, K. Garello, C. Nistor, S. Godey, B. Ballesteros, A. Mugarza, A. Barla, M. Valvidares, E. Pellegrin, A. Ghosh, I. M. Miron, O. Boulle, S. Auffret, G. Gaudin, and P. Gambardella, Phys. Rev. B **89**, 214419 (2014).

[43] B. K. Nikolić, S. Souma, L. P. Zârbo, and J. Sinova, Phys. Rev. Lett. **95**, 046601 (2005).

[44] B. K. Nikolic, L. P. Zarbo, and S. Souma, Phys. Rev. B **73**, 075303 (2006).

[45] *Electron Scattering in Solid Matter: A Theoretical and Computational Treatise*, edited by J. Zabloudil, Springer Series in Solid-State Sciences Vol. 147 (Springer, New York, 2005).

[46] M. Gradhand, M. Czerner, D. V. Fedorov, P. Zahn, B. Y. Yavorsky, L. Szunyogh, and I. Mertig, Phys. Rev. B **80**, 224413 (2009).

[47] M. Gradhand, D. V. Fedorov, P. Zahn, and I. Mertig, Phys. Rev. B **81**, 020403(R) (2010).

[48] C. Heiliger, M. Czerner, B. Y. Yavorsky, I. Mertig, and M. D. Stiles, J. Appl. Phys. (Melville, NY) **103**, 07A709 (2008).

[49] C. Franz, M. Czerner, and C. Heiliger, J. Phys.: Condens. Matter **25**, 425301 (2013).

[50] C. E. Mahr, M. Czerner, and C. Heiliger, Phys. Rev. B **96**, 165121 (2017).

[51] S. Datta, *Electronic Transport in Mesoscopic Systems* (Cambridge University Press, Cambridge, 1995).

[52] C. Herschbach, M. Gradhand, D. V. Fedorov, and I. Mertig, Phys. Rev. B **85**, 195133 (2012).

[53] Y. V. Sharvin, Zh. Eksp. Teor. Fiz. **48**, 984 (1965) [Sov. Phys. JETP **21**, 655 (1965)].

[54] H. L. Wang, C. H. Du, Y. Pu, R. Adur, P. C. Hammel, and F. Y. Yang, Phys. Rev. Lett. **112**, 197201 (2014).

[55] J. Qiao, J. Zhou, Z. Yuan, and W. Zhao, Phys. Rev. B **98**, 214402 (2018).

[56] M.-H. Wu, H. Rossignol, and M. Gradhand, Phys. Rev. B **101**, 224411 (2020).

[57] See Supplemental Material at http://link.aps.org/supplemental/10.1103/PhysRevB.104.054402 for an overview of accumulations of all the small systems as well as accumulations for the larger systems of Cu, Pt, and U. Furthermore, the Fermi surfaces with color encoded group velocities are shown for all systems.

[58] O. Gueckstock, L. Nádvorník, M. Gradhand, T. S. Seifert, G. Bierhance, R. Rouzegar, M. Wolf, M. Vafaee, J. Cramer, M. A. Syskaki, G. Woltersdorf, I. Mertig, G. Jakob, M. Kläui, and T. Kampfrath, Adv. Mater. (Weinheim) **33**, 2006281 (2021).

[59] E. Sagasta, Y. Omori, M. Isasa, M. Gradhand, L. E. Hueso, Y. C. Niimi, Y. Otani, and F. Casanova, Phys. Rev. B **94**, 060412(R) (2016).

[60] T. D. Skinner, K. Olejník, L. K. Cunningham, H. Kurebayashi, R. P. Campion, B. L. Gallagher, T. Jungwirth, and A. J. Ferguson, Nat. Commun. **6**, 6730 (2015).

## 4.2. Publication Phys. Rev. B 105, 165106, (2022)

Electronic transport at very small length scales plays an essential role in today's technical applications. Especially the shrinking sizes make a quantum mechanical approach in describing the occurring effects mandatory. Often semi-classical approaches are used that provide a nice physical interpretation of scattering processes. In this work, the main aim was to understand the relationship between the scattering time $\tau$ that is often used in semi-classical approaches to deliver a graphical and easy-to-interpret physical image and the self-energy $\Sigma$ that is often used in full quantum mechanical approaches as done in the virtual terminal method. Expanding upon Ref. [17], we research the dependency for the simple picture of a **k** independent scattering time $\tau$ with the self-energy $\Sigma$. On the premise that for a constant scattering time, the Seebeck coefficient is not dependent on the scattering time (in the Boltzmann picture), we compare whether this is the case too for the self-energy. We find that this is indeed the case for systems with Fermi surfaces of low complexity, that is, free electrons and Cu, but no longer for Pd with its complex Fermi surface. Because the expected linear scaling of the transmission function at the Fermi level with the scattering time fails in the strong scattering regime, we investigate the discretization effects of the scattering barrier within the more flexible finite difference model for free electrons. We find that in the strong scattering regime, the multiple scattering events between virtual terminals must be resolved with a sufficient number of virtual terminals. For the lower scattering regimes, we find that the number of virtual terminals can be condensed and represented by effective virtual terminals. The placement of virtual terminals inside the conductor makes no difference when enough multiple scattering events are considered. The findings suggest that it would be possible to calculate thicker thin films by scaling up the scattering strength via effective virtual terminals. Introducing the scattering formalism into the full-relativistic approach given in Phys. Rev. B **104**, 054402, (2021), could facilitate the calculation of finite spin-diffusion lengths and the consideration of effects at room temperature. New contributions to the spin accumulation due to scattering could be accounted for.

The manuscript was written by me, edited, and commented on by all co-authors. I implemented the FDM model of free electrons with virtual terminals in Python and expanded it for parallel running on the high-performance computing cluster. I contributed to the expansion of the one-dimensional model into three dimensions. Michael Czerner helped here especially with the lattice Fourier transformation. The virtual terminal approach has been already implemented into the KKR code during the Ph.D. work of Carsten Mahr [17, 18]. I carried out all calculations.

# First-principles scattering with Büttiker probes: The role of self-energies

Alexander Fabian,[1,2,*] Martin Gradhand,[3,4] Michael Czerner,[1,2] and Christian Heiliger[1,2]

[1]*Institute for Theoretical Physics, Justus-Liebig-University Giessen, Heinrich-Buff-Ring 16, 35392 Giessen, Germany*
[2]*Center for Materials Research (LaMa), Justus-Liebig-University Giessen, Heinrich-Buff-Ring 16, 35392 Giessen, Germany*
[3]*HH Wills Physics Laboratory, University of Bristol, Tyndall Avenue BS8 1TL, United Kingdom*
[4]*Institute of Physics, Johannes Gutenberg University Mainz, 55099 Mainz, Germany*

Understanding electronic transport properties is important for designing devices for applications. Many studies rely on the semiclassical Boltzmann approach within the relaxation time approximation. This method delivers a graphic physical picture of the scattering process, but in some cases it lacks full quantum-mechanical effects. Here, we use a non-equilibrium Green's function Korringa-Kohn-Rostoker (KKR) method with phase-breaking scattering via virtual Büttiker terminals as a fully quantum mechanical approach to transport phenomena. With this, we assess the validity of the relation of the self-energy $\Sigma$ to the scattering time $\tau$, often used in literature in the case of constant relaxation time approximation. We argue that the scattering time does not affect the thermopower in the Boltzmann approach and thus should take no effect either on the thermopower calculated via the Keldysh approach. We find a nearly linear relation for the transmission function $T_S(E_F, \Sigma)$ of free electrons and Cu with respect to $\frac{1}{\Sigma}$. However, we find that this is not the case for Pd. We attribute this to neighboring states contributing due to the additional broadening via the self-energy $\Sigma$. These findings suggest that a simple identification of scattering time and self-energy is not sufficient. Finally, we discuss the benefits and limits of the application of the virtual terminal approach.

## I. INTRODUCTION

In the past years, electronic devices have become significantly smaller. Further shrinking the sizes leads to quantum mechanical effects that dominate the transport properties [1–4]. There are several approaches from classical to fully quantum mechanical to characterize transport quantities. Scattering can be accounted for in each of these approaches and of course, the type of scattering has huge influences on the transport properties. While there are full quantum mechanical formalisms like the Kubo formalism [5–9] or the steady-state Keldysh [10–12] formalism, often semiclassical approaches are used to describe transport properties. The physical picture in these semiclassical approaches, mainly the Boltzmann formalism [13–17], is quite intricate since it enables an intuitive understanding in terms of scattering processes. One of the principal quantities for understanding this scattering picture is the scattering or relaxation time $\tau$, which gives the mean time between two scattering events.

Often, first-principle methods rely on the averaging over many configurations of lattice distortions or impurities to obtain semiclassical like features [18,19]. However, room temperature like features can also be established by introducing a dephasing mechanism by means of Büttiker probes (or virtual terminals) [20,21]. In our purely quantum-mechanical Keldysh approach including dephasing virtual terminals, it is not the scattering time, which is the primary determining quantity, but a broadening of the states given by the negative imaginary part $\Sigma$ of the complex self-energy $\overline{\Sigma}$, which is often directly related to the scattering time in angle-resolved photoemission spectroscopy (ARPES) experiments [22,23]. In such scenarios the scattering time is often identified with the lifetime of the state, $\tau_{\text{scat}} = \tau_{\text{life}} = \frac{\hbar}{2\Sigma}$ [24]. For ARPES experiments it was discussed that the single-particle lifetime can be related to the self-energy in this way, but that this single-particle lifetime differs from the lifetime of an excited photo-electron population [25]. The discrepancies were supported by experimental findings [26–28]. Hence, a simple identification of scattering time and self-energy seems nontrivial. However, even in a single-particle description, this simple relationship between lifetime and self-energy might fail.

In this paper, we test the relation of the scattering time and the scattering self-energy in a single-particle description but for real materials. We give an example where such a direct identification is questionable, even for simple, pure metals. This is shown by comparing the theory of the Boltzmann approach with results from a Keldysh non-equilibrium Green's function approach [11,29] in the framework of a Korringa-Kohn-Rostoker (KKR) [30] density functional theory (DFT), in which we use virtual terminals (also known as Büttiker probes) to describe incoherent elastic scattering [10]. We discuss the limit of applicability of virtual terminals by comparing the results of the KKR implementation with a simple finite differences method (FDM) for the case of free electrons [29].

*Alexander.Fabian@physik.uni-giessen.de

## II. THEORY

In order to evaluate transport properties, the following moments $L_n$ are used [31]:

$$L_n = \frac{2}{h} \int dE \int d\vec{k}_\parallel \, (E - \mu)^n \left( -\frac{\partial f(E, \mu, \theta)}{\partial E} \right) T(E, \vec{k}_\parallel), \tag{1}$$

where $h$ is Planck's constant, $E$ is the energy, $\mu$ is the chemical potential, $\theta$ the temperature, $f(E, \mu, \theta)$ is the Fermi-Dirac distribution, and $T(E, \vec{k}_\parallel)$ the $\vec{k}_\parallel = (k_x, k_y)$ dependent transmission function. Normally, these moments are written as tensors. Here, since we are looking at cubic systems only, we restrict ourselves to the $L_n = L_{n,zz}$ component of the full tensor $\underline{L_n}$. From these moments, the conductivity $\sigma$, thermopower $S$, and heat conductivity of the electrons $\kappa_e$ can be calculated as [32]

$$\sigma = e^2 L_0, \tag{2}$$

$$S = \frac{1}{e\theta} \frac{L_1}{L_0}, \tag{3}$$

and

$$\kappa_e = \frac{1}{\theta} \left( L_2 - \frac{L_1^2}{L_0} \right), \tag{4}$$

where $e$ is the electron charge.

### A. Keldysh formalism

In the Keldysh formalism, the general transmission function $T(E) = T_{\text{eff}}(E; \Sigma)$ is an effective transmission function, which results from contributions of different origins. The system is divided into three parts, left, center, and right, where the left and right sides serve as semi-infinite leads and the center region serves as scattering region. Certain scattering events can be realized in the Keldysh formalism by placing virtual terminals, which are also known as Büttiker probes [33], in the scattering region. The virtual terminals absorb and reemit electrons with different phases, thus simulating a phase-breaking scattering event [29,33]. Further details of the implementation are documented in our previous paper [10]. The necessary transmission functions are calculated for every possible terminal configuration via a coherent approach at each in-plane $\vec{k}_\parallel$ point as

$$T_{XY}(E, \vec{k}_\parallel) = \text{Tr}[\underline{\Gamma}_Y(E, \vec{k}_\parallel) \underline{G}(E, \vec{k}_\parallel) \underline{\Gamma}_X(E, \vec{k}_\parallel) \underline{G}^\dagger(E, \vec{k}_\parallel)], \tag{5}$$

where $X, Y \in \mathbf{S} \wedge \{L, R\}$ are virtual terminals or the contacting left (L) and right (R) terminals. $\mathbf{S}$ is the set of all virtual terminals in the scattering region. The matrix $\underline{\Gamma}_\alpha = i(\bar{\Sigma}_\alpha(E)\underline{L}_\alpha - \bar{\Sigma}_\alpha^*(E)\underline{L}_\alpha) = -2\text{Im}\bar{\Sigma}_\alpha\underline{L}_\alpha = 2\Sigma_\alpha\underline{L}_\alpha$ is the broadening function due to self-energy $\Sigma_\alpha$ at site $\alpha$. The matrix $\underline{L}_\alpha$ is 1 only for one site index $\alpha$ and 0 elsewhere. For $\alpha \in \mathbf{S}$, $\Sigma_\alpha$ is the broadening due to scattering. However, $\Sigma_L$ and $\Sigma_R$ describe the contact to the semi-infinite leads and are solely given by the lead material. The partial transmissions $T_{XY}(E, \vec{k}_\parallel)$ are integrated over the in-plane Brillouin zone to obtain $T_{XY}(E)$. From this $\vec{k}_\parallel$ integrated partial transmissions

between the terminals, the resulting effective transmission function $T_{\text{eff}}$ through the whole system can be calculated as

$$T_{\text{eff}}(E) = T_{\text{LR}}(E) + \sum_{\alpha \in \mathbf{S}} \frac{T_{L\alpha}(E) T_{\alpha R}(E)}{S_\alpha(E)}$$

$$+ \sum_{\alpha, \beta \in \mathbf{S}}^{\alpha \neq \beta} \frac{T_{L\alpha}(E) T_{\alpha\beta}(E) T_{\beta R}(E)}{S_\alpha(E) S_\beta(E)} + \dots . \tag{6}$$

Here, $S_\alpha = T_{L\alpha}(E) + T_{\alpha R}(E) + \sum_{\beta \in \mathbf{S}}^{\beta \neq \alpha} T_{\alpha\beta}(E)$, $\alpha \in \mathbf{S}$ is the renormalization sum of the probability measure. Note that all $T_{XY}(E)$ also depend on all $\Sigma_\alpha$ ($\alpha \in \mathbf{S}$), because the Green's function $G(E, \vec{k}_\parallel)$ depends on all $\Sigma_\alpha$ ($\alpha \in \mathbf{S}$). Thus, $T_{XY}(E)$ will change even when a $\Sigma_\alpha$ with $\alpha \neq X, Y$ will change. In the following we assume that $\Sigma_\alpha \equiv \Sigma \, \forall \alpha \in \mathbf{S}$. Consequently, we will write the effective transmission as a function of $E$ and $\Sigma$, that is $T_{\text{eff}}(E; \Sigma)$.

One has to be careful since, in the Keldysh formalism, the resistance arises not only from scattering but also from the system's contacts to the leads. This contact resistance $R_c$ is due to the contact of an ideal lead to a scattering region, where only a limited number of transport modes per area exist and contribute to the transport of an electron. The scattering part of the resistance $R_S$ is due to scattering alone. While $R_S$ naturally depends on the length of the system and on $\Sigma$, $R_c$ does not. $R_c$ solely depends on the type of the contact. Since the two types of resistances form a series circuit and since $R \propto T^{-1}$, the full transmission can be split up as

$$\frac{1}{T_{\text{eff}}(E, \Sigma)} = \frac{1}{T_c(E)} + \frac{1}{T_S(E, \Sigma)}. \tag{7}$$

Here, the contact transmission $T_c(E)$ is the transmission of a system without virtual terminals, and $T_S(E; \Sigma)$ is the contribution due to scattering. $T_c$ is a transmission function that contributes either 0 or 1 at each $\vec{k}$ point for each band and thus is a measure for the number of transport modes. The contribution due to scattering $T_S$ is a probability measure to what extent an electron can traverse the scattering region without being scattered. Thus it is not bounded between 0 and 1. $T_S$, therefore, can rise to infinity, if no scattering occurs, that is $T_S \to \infty$ if $\tau \to \infty$, as it takes infinitely long to scatter. In the Keldysh formalism, the additional contact resistance ensures that the effective transmission function does not rise to infinity.

As depicted schematically in Fig. 1, the influence of the contact resistance is the main contribution for small scattering self-energies $\Sigma$ (large $1/\Sigma$). The contact resistance limits the transmission function to a constant value. The scattering contribution is rising to infinity as one would expect for decreasing scattering. Increasing the scattering self-energy (reducing $1/\Sigma$), $T_S(E; \Sigma)$ and $T_{\text{eff}}(E; \Sigma)$ start to overlap and this leads to a decreasing contribution of the contact resistance in the reciprocal addition of Eq. (7). Thus in the limit of a very long scattering region or strong scattering, the behavior is of only Ohmic nature and the contact resistance does not contribute significantly. We use the term contact resistance for the resistance, which is due to the contact of semi-infinite leads that serve as an electronic reservoir in equilibrium to a scattering region. Here, we consider no contact resistance from surface roughness, etc., like it would be the case in
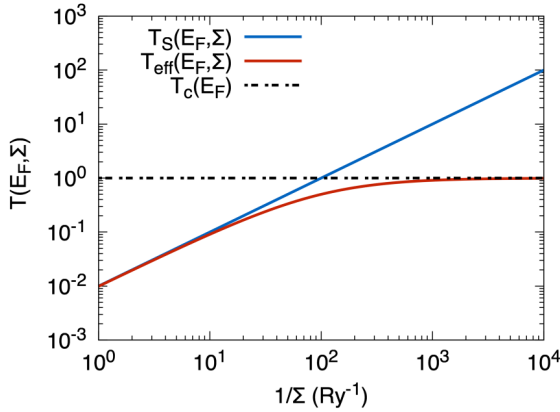
FIG. 1. Schematic depiction of the contributing transmission functions: contact transmission $T_c(E_F)$ (dashed, black), contributions due to scattering $T_S(E_F, \Sigma)$ (blue), and resulting effective transmission $T_{\text{eff}}(E_F, \Sigma)$ (red) via Eq. (7).

experiments. Unless stated otherwise, we consider only the contribution due to scattering $T_S(E; \Sigma)$ in the following as this is the quantity making contact with the Boltzmann approach.

### B. Boltzmann formalism

The Boltzmann transmission function contains contributions due to scattering only and no contribution from the contact resistance. The transmission function in the Boltzmann approach corresponds to $T(E, \vec{k}) = T_S(E, \vec{k}; \tau) = v_z^2(\vec{k})\tau_{\vec{k}}\delta(E - \epsilon(\vec{k}))$, where $v_z$ is the group velocity in transport direction, $\tau_{\vec{k}}$ the $\vec{k}$ dependent scattering time, $\delta(E - \epsilon(\vec{k}))$ is the Dirac delta distribution, and $\epsilon(\vec{k})$ is the electronic energy dispersion.

In the case of free electrons, mapping this transmission function onto the $\vec{k}_\parallel$ plane, which in accordance to Keldysh is equivalent to integrating the $k_z$ components, one arrives at $T_S(E, \vec{k}_\parallel; \tau) = \frac{2\sqrt{2}\tau}{\hbar\sqrt{m}}\sqrt{E - (\hbar^2/(2m))(k_x^2 + k_y^2)}$. Here, we consider the isotropic relaxation time approximation, where $\tau$ is independent of $\vec{k}$ [34–38]. Thus, the moments $L_n$ after Eq. (1) are proportional to $\tau$ and therefore $S$ is independent of $\tau$. That is $\frac{\partial S}{\partial \tau} = 0$, as seen by Eq. (3). Therefore, scattering has no effect on the thermopower in the Boltzmann approach. Consequently, the thermopower can be used as a theoretical test system of the relation between $\Sigma$ and $\tau$. Furthermore, if there is a direct relation such as $\tau \propto 1/\Sigma$, the thermopower should be independent of a $\vec{k}_\parallel$-independent self-energy within the Keldysh formalism. In other words, as long as the relation $\Sigma \propto 1/\tau$ holds, the transmission function $T_S(E; \Sigma)$ within the Keldysh approach should linearly depend on $1/\Sigma$, because in the Boltzmann approach the transmission function $T_S(E; \tau)$ is proportional to the relaxation time.

### C. Finite differences method

To compare the results obtained with our KKR-Keldysh formalism, we use a three-dimensional finite differences method (FDM) for the system of free electrons. Thereby, we can exclude possible numerical shortcomings in our implementation and more importantly, we can check the

applicability of the virtual terminals in KKR, as we are limited to one virtual terminal at each atom at maximum. In contrast, in FDM the number of virtual terminals is unbound.

For one dimension, the finite differences method (FDM) is described in Ref. [29]. We expand on this description to describe free electrons in three dimensions in an, in principle, exact manner. The Schrödinger equation for free electrons can be separated for each spatial dimension. The Hamiltonian is discretized in transport direction and Fourier transformed in the in-plane direction. The Fourier transformation yields corrections for the in-plane directions converting the three-dimensional problem to an effective one dimensional problem via an effective energy in $z$ direction (transport direction), that is $E_z = E - \frac{\hbar^2}{2m}(k_x^2 + k_y^2)$. The Greens function is calculated for the effective one-dimensional problem at the effective energy for each in-plane $\vec{k}_\parallel$ point in the circle described by $\frac{\hbar^2}{2m}(k_x^2 + k_y^2) \leqslant E$ and integrated over all $\vec{k}$ points. The transmission out of this range is zero. Further details calculating the transmission can be found in Ref. [10].

### III. COMPUTATIONAL DETAILS

For evaluation, we consider three different systems. The first system are free electrons serving as a simple model system. The transport parameters of the free electrons are calculated with the DFT-KKR-Keldysh formalism and compared to FDM-Keldysh formalism. As a second system we consider Cu within KKR, because the Fermi surface is very similar to that of free electrons. Finally, as a third system we consider Pd with a rather complex Fermi surface also in KKR.

The potential for the transport calculation in case of free electrons (fe) is a constant potential set to 0. The potentials for Cu and Pd are self-consistently calculated as bulk systems and then used in the transport geometry. Each system is calculated as fcc lattice, where the transport direction is the [001] direction. For the lattice constants we use $a_{\text{fe}} = a_{\text{Cu}} = 6.8311736a_B$, $a_{\text{Pd}} = 7.3524a_B$. Unless stated otherwise, each system has an effective length of $d = 25a_{lat}$, which means that 50 virtual terminals are placed inside the scattering region. Within the KKR method, the transport calculations are done with $400 \times 400$ $\vec{k}_\parallel$ points, $\ell_{\max} = 3$, and an energy broadening of 0.054 meV to ensure convergence of $T_S(E; \Sigma)$ to be better than 1%. In FDM we use 2000 lattice points and $400 \times 400$ $\vec{k}_\parallel$ points for the free electrons to ensure a convergence of $T_S(E; \Sigma)$ better than 1%

### IV. RESULTS AND DISCUSSION

#### A. KKR results

First in Fig. 2, we compare the thermopower of three different systems with increasing complexity of the Fermi surface, namely free electrons, copper (Cu), and palladium (Pd). We assume a $\vec{k}$ independent scattering time $\tau$ and thus use a $\vec{k}$ independent self-energy $\Sigma$ for the Keldysh formalism with virtual terminals. In this simple case of a constant scattering time approximation, the thermopower generally should show no dependence on $\tau$ following the direct linear scaling of the moments $L_0$ and $L_1$ with respect to $\tau$
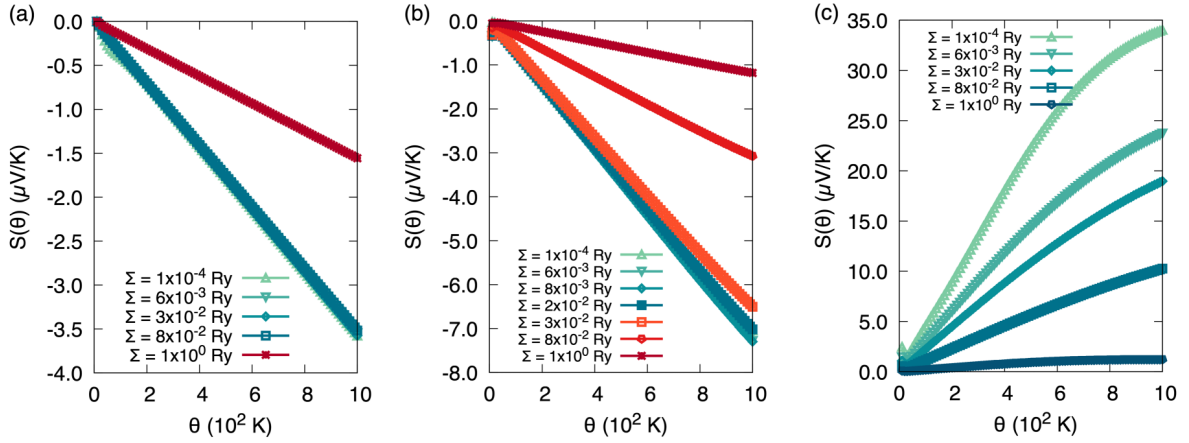
FIG. 2. Thermopower $S(\theta)$ as function of temperature $\theta$ for (a) free electrons, (b) Cu, and (c) Pd at different $\Sigma$ calculated with KKR. Note that in (a) and (b) the blue colored lines overlap.

when considering the Boltzmann theory. If the identification $\tau \propto 1/\Sigma$ is true, it should also give an independence of the thermopower on $\Sigma$ calculated within the KKR-Keldysh formalism.

### 1. KKR Thermopower

For free electrons, the thermopower, as a function of temperature $\theta$ at an arbitrarily chosen value of $E_F = E_1 = 0.75$ Ry, shows exactly this behavior, at least for $\Sigma$ roughly below $8 \times 10^{-2}$ Ry [see Fig. 2(a)]. For higher values of $\Sigma$, it starts to deviate (shown in red).

For Cu, shown in Fig. 2(b), the behavior of the thermopower is qualitatively the same as for free electrons. However, the deviation from the expected behavior is already stronger at smaller self-energies $\Sigma$ compared to free electrons. For Pd, shown in Fig. 2(c), the thermopower shows a distinct temperature dependence for each self-energy, which clearly deviates from the expectation within the relaxation time approximation. This result suggests that a simple identification of $\tau \propto 1/\Sigma$ is not suitable. To get a better understanding we compare the transmission function for these systems in terms of the self-energy. After the comparison of the transmission function, we also check the free electrons against the FDM and discuss the limits of the model in Sec. IV C.

### 2. KKR Transmission function

In Fig. 3(a) we show the $\vec{k}_{\parallel}$ integrated, energy-dependent transmission function $T_S(E; \Sigma)$ for different scattering self-energies $\Sigma$ at the Fermi energy for free electrons. At $E_F = E_1 = 0.75$ Ry we find a good linear behavior, especially for high values of $1/\Sigma$, i.e., in the low-scattering regime. This result suggests that for free electrons, the identification of $\tau$ with the energy broadening self-energy $\Sigma$ via $\tau = \frac{\hbar}{2\Sigma}$ is correct at least for small $\Sigma$ up to around $10^{-1}$ Ry. But even for free electrons $T_S(E; \Sigma)$ shows deviations from the linear behavior for small values of $1/\Sigma$, i.e., in the case of strong scattering.

This deviation from the linear behavior for large $\Sigma$ directly relates to the deviation of the thermopower in Fig. 2(a). We attribute the deviation in $T_S(E; \Sigma)$ to an insufficient discretiza-

tion of the scattering events. This will be discussed further in Sec. IV C by means of the FDM.

The same behavior of $T_S(E_F; \Sigma)$ can be observed for Cu in Fig. 3(b). Here, compared to $T_S(E_F; \Sigma)$ of free electrons, the deviation from the linear behavior starts at smaller self-energies already. Again, this deviation is in accordance with the deviation of the thermopower of Cu discussed before.

When considering Pd in Fig. 3(c). with a more complicated electronic structure and complex Fermi surface, the linear fitting of $T_S(E_F, \Sigma)$ in Fig. 3(c) becomes untenable suggesting, that the relationship $\tau \propto 1/\Sigma$ does not hold at all. Again, the complete deviation from the linear behavior is in accordance with the distinct behavior of the thermopower for each self-energy.

So far, we have used the constant scattering time approximation to assess the validity of the identification of $\Sigma = \frac{\hbar}{2\tau}$. For free electrons and Cu, this identification holds true if $\Sigma$ is small enough, but it is clearly not valid in the case of Pd. The fact that even for simple pure metals in combination with the simple approximation of a constant scattering time [20] the identification of the single-particle scattering time $\tau$ and self-energy $\Sigma$ fails, suggests that for systems with a more complex topology of the Fermi surface and a $\vec{k}$-dependent scattering time $\tau$, the identification of $\Sigma$ and $\tau$ becomes even more difficult. The main ingredient to the KKR-Keldysh approach is the retarded Green's function defined in the upper half of the complex plane in the limit of real energies. At the real energy axis it possesses poles at the eigenenergies of the eigenstates and each eigenstate is represented by a $\delta$-distribution on the real energy axis. Adding an imaginary part to the real energy causes these states to broaden into a Lorentzian shape. If we consider, as it is the case throughout this paper here, a purely imaginary self-energy of the same value at each atomic site, the real energy and the imaginary self-energy can be seen as a new complex energy, which causes the broadening of the states. This broadening of states, however, causes contributions from neighboring states (neighbors with respect to energy) to an existing state at one particular energy due to the overlap. Also for the transmission at one particular energy, the broadening can cause contributions from neighboring electronic states.
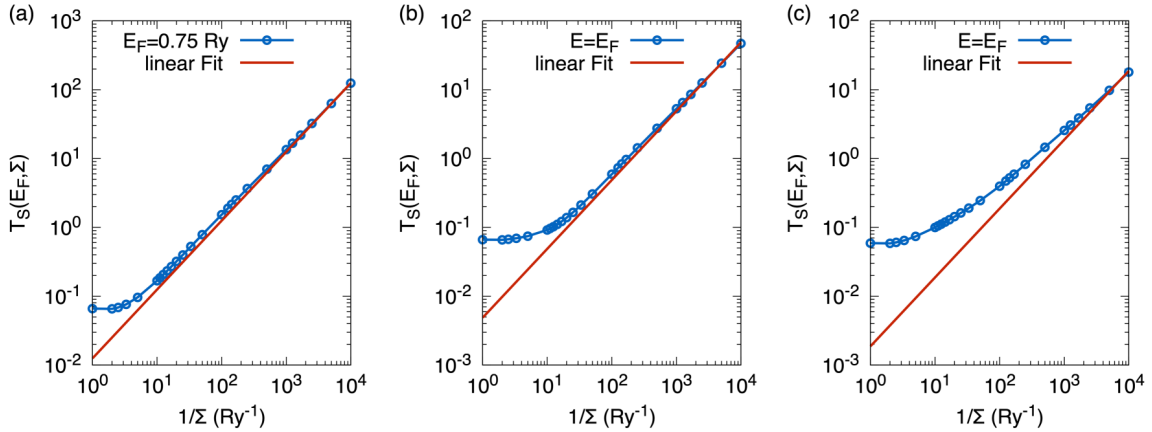
FIG. 3. $T_S(E_F, \Sigma)$ vs $1/\Sigma$ for (a) free electrons, (b) Cu, and (c) Pd in KKR with linear fits.

In the Boltzmann theory, the transport properties at one particular energy are determined solely by the band structure properties of the considered state, and no additional broadening of states is considered. This may cause inaccuracies when translating one quantity into the other and vice versa. Consequently, we attribute the deviations from the linear behavior of Pd to effects caused by the energy broadening.

**B. FDM results**

In order to test the numerical implementation of the KKR method, we compare it to the thermopower calculated via the FDM method in Fig. 4. We see a similar trend for the deviation of thermopower, namely a deviation of the thermopower for high self-energies. We will explain this deviation for high self-energies in Sec. IV C.

In the Boltzmann approach, considering free electrons, the $\vec{k}$-integrated $T_S(E; \tau)$ can be shown to be proportional to $\tau E^{3/2}$. The proportionality to $E^{3/2}$ holds true to some extent for the Keldysh version of $T_S(E; \Sigma)$. For comparison, $T_S(E; \Sigma)$ for free electrons is shown in Fig. 5 calculated with FDM and KKR. The transmission functions between the two methods match quite well. In Fig. 6 the $\vec{k}_\parallel$ integrated transmission $T_S(E_F; \Sigma)$ is shown for the FDM method for different scattering self-energies $\Sigma$. Comparing Fig. 6 with Fig. 3(a) we find for both methods, KKR and FDM, a good linear behavior,

especially for high values of $1/\Sigma$, i.e., less scattering events. The deviation from the linear behavior appears at smaller self-energies for a lower energy of $E_0 = 0.01$ Ry. While both methods give results that deviate from linear behavior in the strong scattering regime, the precise form is different [cf. Figs. 2(a) and 3(a)]. We discuss this in Sec. IV C. The different characteristic of the deviating thermopower in Figs. 2(a) and 4 are a direct consequence of different deviations of $T_S(E; \Sigma)$ in Figs. 3(a) and 6 in the strong scattering regime.

In the strong scattering regime, both methods overestimate $T_S(E; \Sigma)$ relative to the linear fit. We attribute this to low-energy contributions at the edge of the broadened $\vec{k}$-dependent transmission. Such a transmission is shown in Fig. 7. In Fig. 7(a) the contact transmission is shown for the first Brillouin zone. The values of $T_c(E_F, \vec{k}_\parallel)$ are restricted to 1 inside the circle defined by the Fermi energy and 0 outside this circle. The overlapping occurs due to back folding to the Brillouin zone. In Fig. 7(b), the scattering part of the transmission function $T_S(E_F, \vec{k}_\parallel)$ is shown. The smearing due to scattering at the edges is visible. In Fig. 8, $T_S(E_2; \Sigma)$ at $E_2 = 0.25$ Ry is shown for different integration radii in $\vec{k}_\parallel$ space. $T_S(E_2; \Sigma)$ is normalized to the result for $\Sigma = 10^{-4}$ Ry, as the overall area changes for each curve.
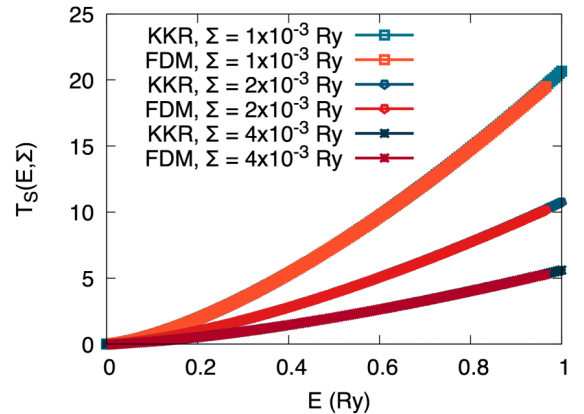


FIG. 4. Thermopower $S(\theta)$ as a function of temperature $\theta$ for free electrons calculated with FDM at different $\Sigma$.



FIG. 5. Scattering contribution to the transmission $T_S(E, \Sigma)$ for different self-energies $\Sigma$ for free electrons in KKR (blue) and FDM (red).
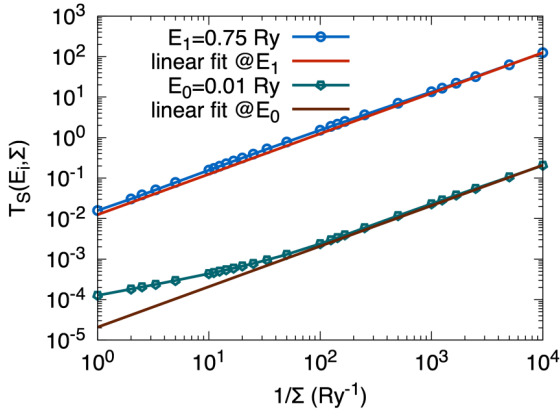
FIG. 6. $T_S(E_i, \Sigma)$, $i = 1, 2$, as function of $1/\Sigma$ for free electrons in FDM with linear fits at $E_0 = 0.01$ Ry and $E_1 = 0.75$ Ry.

At the $\Gamma$ point, the transmission function shows linear behavior. Integrating only 10% of the radius determined by $\sqrt{E}$, the behavior stays mostly linear. Integration up to 90% or more shows the deviation from the linear behavior. We attribute this deviation to edge parts of the transmission, where the effective energy for transport in $z$ direction becomes very small such that the discretization of scattering events through the virtual terminals is not sufficient. We elaborate more on this topic in the next section.

### C. Limits of the model

Since there are apparent deviations of $T_S(E; \Sigma)$ [see Figs. 3(a) and 6] from the linear behavior, we investigate this problem in terms of the number and placement of virtual terminals. For this we use the FDM model since it provides more freedom to test the placement of virtual terminals compared to the KKR method. In contrast to the continuous FDM or Boltzmann theory, within the KKR framework, the highest possible number of virtual terminals that can be placed in the scattering region is the number of atoms in the cell as the virtual terminals are placed at the atomic positions.

In the FDM model, the space in $z$ direction is discretized. The corresponding discretization parameter $a = d_z/(n-1)$
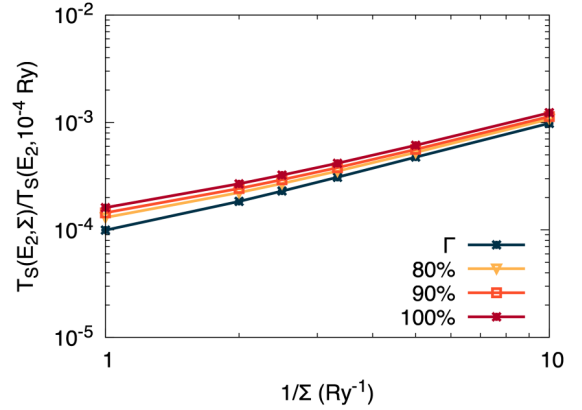


FIG. 8. Normalized transmission function $T_S(E_2; \Sigma)/T_S(E_2; 10^{-4}$ Ry) of free electrons calculated with FDM at $E_2 = 0.25$ Ry. $T_S(E_2, \Sigma)$ shows linear behavior at the $\Gamma$ point (blue). Integrating up to 80%, 90%, and 100% (warm colors) of the radius of the broadened transmission circle $\vec{k}_\parallel$ space shows overestimations from the expected linear behavior.

can be chosen arbitrarily small in principle and must be chosen reasonably small to achieve convergence for the effective transmission. On each of these $n$ discretized lattice points, it is possible to place a virtual terminal.

Figure 9 shows $\Delta T_S/T_S$ for $E_0 = 0.01$ Ry and $E_1 = 0.75$ Ry (blue, red), respectively, for different values of $\Sigma$. Starting from 2000 lattice points, a virtual terminal is located at every lattice point. To test the discretization of the scattering events, we reduce the number of virtual terminals. The placement is uniform such that a virtual terminal is added to every $i$th lattice point. To achieve the same total amount of scattering, the self-energy $\Sigma_i$ of the $i$th individual virtual terminal is scaled so that the sum $\sum_{i \in \mathbf{S}} \Sigma_i$ stays constant. The actual number of virtual terminals is shown on the $x$ axis.

With this test, it is possible to show that for a certain number of virtual terminals at a certain self-energy $\Sigma$, the obtained result for $T_S(E_i; \Sigma)$ deviates significantly from the value of $T_S(E_i; \Sigma)$ when it is discretized to the maximum at 2000 lattice points. The deviation increases as the number of virtual terminals decreases, going beyond 1% for less
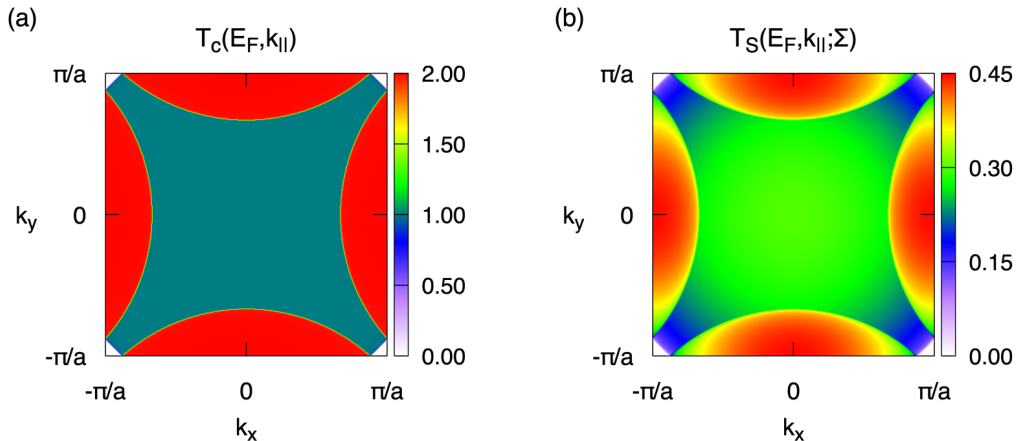


FIG. 7. $\vec{k}_\parallel$-dependent transmission function of free electrons calculated with KKR. (a) Contact transmission function and (b) scattering part of transmission $T_S(E_F, \vec{k}_\parallel, \Sigma)$ for $\Sigma = 3 \times 10^{-2}$ Ry.
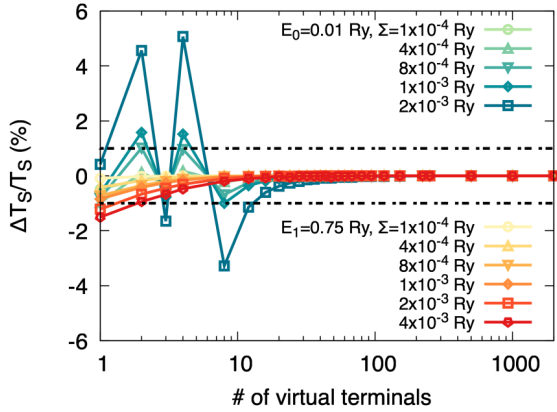
FIG. 9. Relative deviation of $T_S(E_i, \Sigma)$ vs number of virtual terminals for free electrons. As the number of virtual terminals inside the constant scattering region decreases, the distance between the virtual terminals increases. The single $\Sigma_i$ has to be scaled accordingly, to meet the condition $\sum_{i \in \mathbf{S}} \Sigma_i = \text{const}$.



FIG. 11. $T_S(E_F, \Sigma)$ vs $1/\Sigma$ for free electrons for different discretizations of the scattering potential barrier. The actually used self-energy $\Sigma'$ has to be scaled to meet the "effective" self-energy $\Sigma$.

than about 10 terminals for $E = 0.01\,\text{Ry}$. We attribute this to multiple-scattering effects with a very high number of scattering events that cannot be accounted for due to the lack of the necessary number of virtual terminals. Thus, the discretization to describe all scattering events is insufficient.

For larger $\Sigma$ or smaller $E$ this starts to happen for a higher number of virtual terminals, i.e., a finer discretization, as the number of scattering events, that should occur is antiproportional to the mean free path $\lambda = v\tau = \sqrt{2E/m}\,\hbar/(2\Sigma)$. Transferring this result to the KKR method implies that at very high self-energies, the discretization of the scattering events is not sufficient anymore. Thus, interatomic positions for virtual terminals would have to be utilized to overcome this deficiency.

To test whether this effect is related to the actual distance of virtual terminals, we randomly placed 20 virtual terminals in the transport cell. Figure 10 shows $\Delta T_S/T_S$ for different random distributions of virtual terminals. For larger self-energies, some distributions show larger deviations. The results suggest that virtual terminals can actually be placed randomly but yield the same result within 1% deviation as long as the



FIG. 10. Relative deviation of $T_S(E_i, \Sigma)$ for free electrons vs 20 different distributions of a constant number of 20 virtual terminals, which are placed randomly over the scattering region.

self-energy is small enough for the scattering events to be accounted for. This means that the effective strength of the scattering region is not determined by the region covered with virtual terminals but only by the overall strength of self-energies $\sum_{i \in \mathbf{S}} \Sigma_i$. The distance between the virtual terminals is not crucial since the transmission between two terminals $T_{\alpha\beta}$ is calculated coherently. With these restrictions in mind, a description of a macroscopic experimental thin film should be possible. The practical route is to calculate a microscopic, downsized version of the thin film. In order to account for the same scattering strength, the self-energies have to be scaled according to the length of the scattering region. Here it is crucial to introduce a sufficient number of virtual terminals to account for all necessary multiple scattering events.

Finally, let us explain the observed deviation of $T_S(E_F, \Sigma)$ for large self-energies in the KKR approach. In Fig. 11, $T_S(E_F, \Sigma)$ for the KKR method, where a virtual terminal is attributed to each atomic position, is compared to the FDM method with a changing number of virtual terminals. The FDM method for 2000 virtual terminals is considered as the exact converged result. Depending on the number of virtual terminals, $T_S(E_F; \Sigma)$ over- or underestimates the correct result in the strong scattering regime. Additionally, since the KKR uses different approximations than the FDM, e.g., atomic sphere potentials and expansion of functions in spherical harmonics with $\ell$ cutoffs, deviations are expected to occur, while not necessarily with the same numerical value.

## V. CONCLUSION

We calculated the thermopower $S(\theta)$ and the transmission function $T_S(E; \Sigma)$ for free electrons, Cu, and Pd with scattering events realized by virtual terminals. The thermopower $S(\theta)$ for the free electrons and Cu shows no dependence on the self-energy $\Sigma$, if it is below a specific value of $\Sigma$. This is directly related to the linear scaling of $T_S(E; \Sigma)$ with $1/\Sigma$ in that regime for the two systems. For free electrons, we can explain the deviations from the linear behavior in terms of insufficient discretization of scattering events. Further, we show that the distance between virtual terminals plays no

role, as long as enough scattering events are considered. For Pd, however, we find a nonlinear behavior in $T_S(E; \Sigma)$ even for small self-energies $\Sigma$ and a distinct behavior of the thermopower $S(\theta)$ for each self-energy $\Sigma$. This result suggests that $\tau$ may not be easily identified with $\hbar/(2\Sigma)$ for more complex Fermi surfaces. We conclude that even in the simple constant relaxation time approximation with $\vec{k}$-independent $\tau$ the identification of the scattering time with the lifetime associated with $\vec{k}$-independent $\Sigma$ is not true in general. For the case of a $\vec{k}$-dependent $\tau$ or the energy-dependent self-energy function $\Sigma(E)$ obtained from rigorous many-body treatment, this identification would become even more problematic. We have shown possible errors in the KKR approach when using virtual terminals to describe scattering, namely using too large self-energies, and low-energy contributions at the edge of the Fermi surface. These errors however, are very small when considering practical self-energies for Cu and Pd. For Cu, values for $\Sigma$ ranging from $7 \times 10^{-4} - 3.7 \times 10^{-3}$ Ry were calculated [39] in good agreement with the referenced experiment therein. For Pd, values ranging from $3.7 \times 10^{-4} - 1.1 \times 10^{-2}$ Ry were calculated depending on temperature and

surface state [40,41]. Considering the limits of the virtual terminal approach, it should be possible to calculate macroscopic thin films, which opens up the way to describe real experimental structures. As we have shown in an earlier paper [42] that it is possible to calculate the spin accumulation in clean systems within the Keldysh formalism, extending it to scattering via virtual terminals could make it possible to also calculate the spin diffusion length for such systems or to consider additional contributions to the accumulation.

### ACKNOWLEDGMENTS

[1] S. Datta and M. J. McLennan, Rep. Prog. Phys. **53**, 1003 (1990).

[2] T. J. Thornton, Rep. Prog. Phys. **58**, 311 (1995).

[3] M. P. Das and F. Green, J. Phys.: Condens. Matter **21**, 101001 (2009).

[4] L. L. Sohn, L. P. Kouwenhoven, and G. Schön (eds.), *Mesoscopic Electron Transport* (Springer Netherlands, Dordrecht, 1997).

[5] R. Kubo, J. Phys. Soc. Jpn. **12**, 570 (1957).

[6] T. Low, A. S. Rodin, A. Carvalho, Y. Jiang, H. Wang, F. Xia, and A. H. Castro Neto, Phys. Rev. B **90**, 075434 (2014).

[7] S. Lowitzer, M. Gradhand, D. Ködderitzsch, D. V. Fedorov, I. Mertig, and H. Ebert, Phys. Rev. Lett. **106**, 056601 (2011).

[8] G. Y. Guo, Y. Yao, and Q. Niu, Phys. Rev. Lett. **94**, 226601 (2005).

[9] Y. Yao and Z. Fang, Phys. Rev. Lett. **95**, 156601 (2005).

[10] C. E. Mahr, M. Czerner, and C. Heiliger, Phys. Rev. B **96**, 165121 (2017).

[11] C. Heiliger, M. Czerner, B. Y. Yavorsky, I. Mertig, and M. D. Stiles, J. Appl. Phys. **103**, 07A709 (2008).

[12] C. Franz, M. Czerner, and C. Heiliger, J. Phys.: Condens. Matter **25**, 425301 (2013).

[13] I. Mertig, Rep. Prog. Phys. **62**, 237 (1999).

[14] W. Li, Phys. Rev. B **92**, 075405 (2015).

[15] J. M. Ziman, *Principles of the Theory of Solids*, 2nd ed. (Cambridge University Press, Cambridge, 1972).

[16] C. Herschbach, M. Gradhand, D. V. Fedorov, and I. Mertig, Phys. Rev. B **85**, 195133 (2012).

[17] G. Géranton, B. Zimmermann, N. H. Long, P. Mavropoulos, S. Blügel, F. Freimuth, and Y. Mokrousov, Phys. Rev. B **93**, 224420 (2016).

[18] J. K. Glasbrenner, B. S. Pujari, and K. D. Belashchenko, Phys. Rev. B **89**, 174408 (2014).

[19] A. A. Starikov, Y. Liu, Z. Yuan, and P. J. Kelly, Phys. Rev. B **97**, 214415 (2018).

[20] R. Golizadeh-Mojarad and S. Datta, Phys. Rev. B **75**, 081301(R) (2007).

[21] C.-L. Chen, C.-R. Chang, and B. K. Nikolić, Phys. Rev. B **85**, 155414 (2012).

[22] M. Calandra and F. Mauri, Phys. Rev. B **76**, 205411 (2007).

[23] M. Sentef, A. F. Kemper, B. Moritz, J. K. Freericks, Z.-X. Shen, and T. P. Devereaux, Phys. Rev. X **3**, 041033 (2013).

[24] A. F. Kemper, O. Abdurazakov, and J. K. Freericks, Phys. Rev. X **8**, 041009 (2018).

[25] S.-L. Yang, J. A. Sobota, D. Leuenberger, Y. He, M. Hashimoto, D. H. Lu, H. Eisaki, P. S. Kirchmann, and Z.-X. Shen, Phys. Rev. Lett. **114**, 247001 (2015).

[26] K. Sugawara, T. Sato, S. Souma, T. Takahashi, and H. Suematsu, Phys. Rev. Lett. **98**, 036801 (2007).

[27] G. Moos, C. Gahl, R. Fasel, M. Wolf, and T. Hertel, Phys. Rev. Lett. **87**, 267402 (2001).

[28] I. Gierz, S. Link, U. Starke, and A. Cavalleri, Faraday Discuss. **171**, 311 (2014).

[29] S. Datta, *Electronic Transport in Mesoscopic Systems* (Cambridge University Press, Cambridge, 1995).

[30] J. Zabloudil, ed., *Electron Scattering in Solid Matter: A Theoretical and Computational Treatise*, Springer Series in Solid-State Sciences No. 147 (Springer, Berlin, 2005).

[31] M. Czerner and C. Heiliger, J. Appl. Phys. **111**, 07C511 (2012).

[32] Y. Ouyang and J. Guo, Appl. Phys. Lett. **94**, 263107 (2009).

[33] M. Büttiker, Phys. Rev. B **32**, 1846 (1985).

[34] D. I. Pikulin, C.-Y. Hou, and C. W. J. Beenakker, Phys. Rev. B **84**, 035133 (2011).

[35] M. Zebarjadi, S. E. Rezaei, M. S. Akhanda, and K. Esfarjani, Phys. Rev. B **103**, 144404 (2021).

[36] A. Hackl and S. Sachdev, Phys. Rev. B **79**, 235124 (2009).

[37] C. Zhang, S. Tewari, and S. Chakravarty, Phys. Rev. B **81**, 104517 (2010).

[38] L. Chaput, P. Pécheur, and H. Scherrer, Phys. Rev. B **75**, 045116 (2007).

[39] M. Xu, J.-Y. Yang, S. Zhang, and L. Liu, Phys. Rev. B **96**, 115154 (2017).

[40] I. Y. Sklyadneva, A. Leonardo, P. M. Echenique, S. V. Eremeev, and E. V. Chulkov, J. Phys.: Condens. Matter **18**, 7923 (2006).

[41] I. Y. Sklyadneva, R. Heid, V. M. Silkin, A. Melzer, K. P. Bohnen, P. M. Echenique, T. Fauster, and E. V. Chulkov, Phys. Rev. B **80**, 045429 (2009).

[42] A. Fabian, M. Czerner, C. Heiliger, H. Rossignol, M.-H. Wu, and M. Gradhand, Phys. Rev. B **104**, 054402 (2021).

# 5. Conclusion and Outlook

Finally, we will review the obtained results of this work and give a short outlook for future work.

The first part described the spin Hall effect and how to obtain it within the framework of KKR. The approach shows reasonable results when compared with a semi-classical Boltzmann approach. This includes both the similar trend for different metallic systems between the Keldysh and the Boltzmann method as well as the reproduction of the sign changes in accumulation.

The approach considers the finite size of the sample and the surface or interface, respectively, and opens the possibility of investigating more complex interfacial structures. Further, the possibility of explicitly adding an external bias voltage brings this approach nearer to the experimental reality. However, we only considered the magnetization parts from the Fermi surface, which are odd under spatial inversion.

The second part deals with the identification of the self-energy $\Sigma$ and the scattering time $\tau$. It was shown that this identification is not as simple as it seems. Instead, the identification holds some caveats and can be made only for systems with simple Fermi surfaces. Moreover, we found that the discretization of scattering events plays an important role in achieving a converged result. If the discretization is too rough, the necessary multiple scattering events get overlooked, resulting in a jumping behavior of the transmission function. However, if there are enough virtual terminals to consider all the events, the placement of the scatterer becomes arbitrary.

Especially, the implementation of the full self-consistent cycle has raised further possibilities to expand upon. These include:

1. The magneto capacitance of a Fe-Vac-Fe tunnel barrier

2. An in-depth analysis of the self-consistent spin Hall effect

3. The $\mathbf{k}$ space implementation of the Kerker screening for potential mixing

These points have already been mentioned in the appendix and are described there. Point 1) would describe a novel effect that stands in line with the magnetoresistance. Point 2) closes the gap between the Kubo formalism and the Keldysh description used here and further extends upon the Boltzmann theory. Point 3) should yield facilitation for the convergence of large supercells, especially if they include a large number of vacuum spheres, therefore, making it easier to achieve self-consistency for larger spin Hall systems.

To extend this method for more realistic descriptions, the following points are possible.

## Multi-terminal transport

Since the spin Hall effect generates a transversal spin current from a longitudinal charge current, the extension of the KKR code to support multi-terminal transport is feasible.

A second decimation technique which is so-to-speak perpendicular to the normal one would enable one to calculate a transverse current. Instead of adding the transmission function of the two transport channels, the difference $m_\uparrow T_\uparrow - m_\downarrow T_\downarrow$ could yield a quantity proportional to the spin current $\mathbf{j}_s$.

## Characteristic quantities

The spin conductivity or spin Hall angle could be calculated to obtain a more direct comparison with other theories or experiments. As the longitudinal conductivity (neglecting the effects of contact resistance) is actually infinite in ballistic transport, a means to limit the conductivity to finite values has to be found. The virtual terminal formalism, which introduces scattering, yields such a means. The theory of the virtual terminal approach has to be reformulated to match the new multi-terminal setting. Additionally, the contributions to the charge density due to the virtual terminals have to be included. By doing this, one should achieve values for the longitudinal conductivity and the transverse spin conductivity, which would yield the spin Hall angle. Further, the scattering formalism should lay a foundation to describe spin relaxation processes and therefore to obtain values for the spin relaxation length or spin relaxation time.

## Extrinsic contributions

Extrinsic contributions were not considered up until now. The framework, as mentioned earlier, has to be included either in a real space version of the KKR code with impurities or very large supercells with an impurity have to be calculated to describe the effects of impurities. The coherent potential approximation has to be used in conjunction with the framework mentioned earlier to describe alloys. The implementation details, however, are not yet clear, and they might bear some complicated intricacies. However, the complete framework, which consists of multi-terminal transport with virtual terminal scattering and the inclusion of impurities together with the full steady-state non-equilibrium Green's function formalism, bears a great opportunity to bring theoretical description and real systems very close to each other, for an effect where there is very much debate going on about the physical details up until today. With this implementation, the first step in this direction could be done.

# Appendix

# A. Basic Theory

## A.1. Density Functional Theory

The density functional theory is based on the Hohenberg-Kohn theorem [95] and has gained immense popularity since its invention for describing molecules or condensed matter systems. Especially in condensed matter physics, the problem is the large number of particles to describe. This number is of the order of $10^{23}$. The task is now to separate the electronic problem from the problem of the cores and, in a second step, to find a method to reduce the amount of quantities to be calculated. The first is done via the Born-Oppenheimer approximation, while the latter involves the Hohenberg-Kohn theorem.

### A.1.1. Born-Oppenheimer Approximation

We start with the full Hamiltonian of a condensed matter system with only Coulomb interactions. In atomic units ($e^2 = 2$, $\hbar = 1$, $2m_e = 1$, $a_0 = \frac{\hbar^2}{me^2}$, $4\pi\varepsilon_0 = 1$) it reads [96]:

$$\mathcal{H} = \mathcal{T}_K + \mathcal{T}_e + \mathcal{V}_{ee} + \mathcal{V}_{Ke} + \mathcal{V}_{KK} \tag{A.1}$$

$$= -\sum_{i=1}^{N_e} \frac{\partial^2}{\partial \mathbf{r}_i^2} - \sum_{i=1}^{N_k} \frac{1}{M_i} \frac{\partial^2}{\partial \mathbf{R}_i^2} \tag{A.2}$$

$$+ \sum_{\substack{i,j=1 \\ i<j}}^{N_e} \frac{2}{|\mathbf{r}_i - \mathbf{r}_j|} - \sum_{i=1}^{N_e} \sum_{j=1}^{N_k} \frac{2Z_j}{|\mathbf{r}_i - \mathbf{R}_j|} + \sum_{\substack{i,j=1 \\ i<j}}^{N_k} \frac{2Z_i Z_j}{|\mathbf{R}_i - \mathbf{R}_j|}. \tag{A.3}$$

Here, $N_e$ is the number of electrons, $N_K$ the number of cores, $Z_i$ the atomic number of the $i$-th element, $\mathbf{R}_i$ denotes the position of the cores, and $\mathbf{r}_i$ the positions of electrons. The contributions are:

1. $\mathcal{T}_K$: kinetic energy of the cores

2. $\mathcal{T}_e$: kinetic energy of the electrons

3. $\mathcal{V}_{ee}$: electron-electron Coulomb interaction

4. $\mathcal{V}_{Ke}$: core-electron Coulomb interaction

5. $\mathcal{V}_{KK}$: core-core Coulomb interaction.

Since the motion of the atomic cores tends to be much smaller, that is $1/M_K < 10^{-4}$, within the so-called Born-Oppenheimer approximation the contribution of their kinetic

energy can be neglected in the lowest order. Excluding the kinetic energy of the cores, it remains

$$H_0 = -\sum_{i=1}^{N_e} \frac{\partial^2}{\partial \mathbf{r}_i^2} + \sum_{\substack{i,j=1 \\ i<j}}^{N_e} \frac{2}{|\mathbf{r}_i - \mathbf{r}_j|} - \sum_{i=1}^{N_e}\sum_{j=1}^{N_k} \frac{2Z_j}{|\mathbf{r}_i - \mathbf{R}_j|} + \sum_{\substack{i,j=1 \\ i<j}}^{N_k} \frac{2Z_i Z_j}{|\mathbf{R}_i - \mathbf{R}_j|} \tag{A.4}$$

in which the positions of the fixed cores can be treated as a parameter. The resulting eigenvalue equation for the separated electronic problem

$$H_0 \varphi_\alpha (\mathbf{r}, \mathbf{R}) = \epsilon_\alpha (\mathbf{R}) \varphi_\alpha (\mathbf{r}, \mathbf{R}) \tag{A.5}$$

yields the electronic wave functions $\varphi_\alpha$. Since they form a full orthonormal basis, the solution of the full eigenvalue problem

$$H\psi (\mathbf{r}, \mathbf{R}) = E\psi (\mathbf{r}, \mathbf{R}) \tag{A.6}$$

can be expanded by means of the electronic eigenfunctions $\varphi_\alpha (\mathbf{r}, \mathbf{R})$:

$$\psi (\mathbf{r}, \mathbf{R}) = \sum_\alpha \chi_\alpha (\mathbf{R}) \varphi_\alpha (\mathbf{r}, \mathbf{R}) . \tag{A.7}$$

Plugging Eq. A.7 into Eq. A.6, multiplying with $\varphi_\alpha^* (\mathbf{r}, \mathbf{R})$ and integrating over all electronic positions [96], neglecting the electron and core interactions [18] this finally yields the eigenvalue equation for the cores

$$(T_K + \varepsilon_\beta (\mathbf{R})) \chi_\beta (\mathbf{R}) = E\chi_\beta (\mathbf{R}) . \tag{A.8}$$

The cores are moving in the effective potential $\varepsilon_\beta (\mathbf{R})$ created by the electrons. By means of the Born Oppenheimer approximation, the electronic problem has been separated from the problem of the cores[1]. For the fixed positions of the cores, now the electronic problem remains to be solved.

## A.1.2. Kohn-Sham Equations

The problem is still that a large number of electrons have to be described. Instead of calculating the many-body wave function of the whole electronic system, the Hohenberg-Kohn theorem [95] can be used to only calculate the density of the electrons instead. The Hohenberg Kohn theorem states [96]

1. The ground state energy is a unique functional of the ground state density.

2. For the ground state density, the energy functional $E\{n(\mathbf{r})\}$ becomes minimal.

Statement 1 can also be reformulated to "The one particle potential is a unique functional of the ground state density" [95]. In other words, if the ground state is found, the corresponding energy is the ground state energy. It is therefore necessary to minimize the energy as a functional of the density. The energy functional can be split into con-

---

[1]The core-core interaction enters as a constant shift of the potential and is called Madelung constant.

tributions of the kinetic energy $T$, the (external) potential[2] $V$ and the electron-electron interaction energy $U$ [96]

$$E\{n(\mathbf{r})\} = T\{n(\mathbf{r})\} + V\{n(\mathbf{r})\} + U\{n(\mathbf{r})\} \tag{A.9}$$

$$= -\sum_{i=1}^{N_e} \int \psi_i^*(\mathbf{r})\nabla^2\psi_i(\mathbf{r})\mathrm{d}\mathbf{r} + \int V(\mathbf{r})n(\mathbf{r})\,\mathrm{d}\mathbf{r} \tag{A.10}$$

$$+ \iint \frac{n(\mathbf{r})n(\mathbf{r}')}{|\mathbf{r} - \mathbf{r}'|}\,\mathrm{d}\mathbf{r}\mathrm{d}\mathbf{r}' + E_{xc}\{n(\mathbf{r})\}. \tag{A.11}$$

Here, the ansatz for $T\{n(\mathbf{r})\}$ is made for an interaction-free electron gas under the assumption that the many-body wave function is actually representable by a combination of single-particle wave functions. The validity of the representation of the kinetic energy with single-particle wave functions for interacting electrons is not clear initially. Any contributions caused by the non-applicability of this ansatz will be included in the exchange-correlation part $E_{xc}\{n(\mathbf{r})\}$ [96]. The ansatz for $U$ is justified by the classical electron-electron interaction. Since this is the quantum mechanical Hartree contribution, only exchange-correlation contributions are included in $E_{xc}$ [96].
To find the minimal energy, the variation $\delta E$ must vanish. This is done under the condition that the wave function is normalized [96]. The resulting equations are the so-called Kohn-Sham equations [96]

$$\left(-\nabla^2 + V_{\mathrm{eff}}(\mathbf{r})\right)\psi_i(\mathbf{r}) = \epsilon_i\psi_i(\mathbf{r}), \tag{A.12}$$

where the effective potential is defined as [96]

$$V_{\mathrm{eff}}(\mathbf{r}) = V(\mathbf{r}) + \int \frac{2n(\mathbf{r}')}{|\mathbf{r} - \mathbf{r}'|}\,\mathrm{d}\mathbf{r}' + \frac{\delta E_{xc}\{n(\mathbf{r})\}}{\delta n(\mathbf{r})}. \tag{A.13}$$

The Kohn-Sham wave function $\psi_i$ and the Lagrange parameter $\epsilon_i$ have no real physical meaning, other than that they belong to an effective one-particle substitute system which yields the same electronic density as the real system [96]. The biggest problem remains the determination of the exchange-correlation potential $V_{xc} = \frac{\delta E_{xc}\{n(\mathbf{r})\}}{\delta n(\mathbf{r})}$. In practice, there are various approaches. The most common one is the local density approximation (LDA) or the local spin-density approximation (LSDA) in the spin-dependent case with different approaches of parameterization. In this work, the parameterization of Vosko, Wilk, and Nusair [97] will be used. Other approaches are the generalized gradient approximation [98] or the $GW$ approach [99].
Within a self-consistent cycle, the electronic density is calculated from a starting guess of the potential. For this density, the potential is re-calculated. If this potential happens to coincide with the former potential, that is, within a small error boundary, the potential is found. If not, the new potential will be mixed with the old potential and subsequently used as new input potential until the calculation eventually converges. Normally, simple mixing is used, where the new potential for the next cycle is given by $V_{\mathrm{new}} = a_{\mathrm{mix}}V_{\mathrm{old}} + (1 - a_{\mathrm{mix}})V_{\mathrm{calculated}}$. $V_{\mathrm{old}}$ is the input potential of the current cycle, $V_{\mathrm{calculated}}$ is the potential calculated in the current cycle, and $a_{\mathrm{mix}} \in [0, 1]$ is the mixing parameter. There are, however, more elaborated mixing schemes, such as the Broyden mixing schemes [100, 101] or the Anderson mixing scheme [102].

---

[2]The potential generated by the cores.

Instead of calculating the wave functions and from there the density, it is possible to calculate the density, as well as many other physical observables, from the Green's function.

## A.2. Green's Functions

As the Green's function can be seen as a propagator or a correlation function, the formulation of the KKR in terms of Green's functions can be seen as a more suitable approach in the basis of multiple scattering.

Especially the non-equilibrium Green's function method is a strong feature of the KKR. Therefore, we want to introduce the method of Green's functions here shortly.

### A.2.1. Definition

In quantum mechanics, the stationary Schrödinger equation

$$\mathcal{H} |\psi\rangle = E |\psi\rangle \tag{A.14}$$

is of particular interest. Here, $\mathcal{H}$ is the Hamiltonian, and $E$ the eigenenergy. To solve this differential equation, the Green's function proves useful. A differential equation with the differential operator $\mathcal{D}$

$$\mathcal{D} |y\rangle = |f\rangle \tag{A.15}$$

can be solved for the solution $|y\rangle$ as

$$\mathcal{G}\mathcal{D} |y\rangle = |y\rangle = \mathcal{G} |f\rangle , \tag{A.16}$$

by defining $\mathcal{G} = \mathcal{D}^{-1}$. The Green's function for solving the stationary Schrödinger equation case is normally defined for the equation

$$(E\mathcal{I} - \mathcal{H}) |\psi\rangle = 0 \tag{A.17}$$

as

$$\mathcal{G}(E\mathcal{I} - \mathcal{H}) = \mathcal{I}, \tag{A.18}$$

which can be written as

$$\mathcal{G} = (E\mathcal{I} - \mathcal{H})^{-1}. \tag{A.19}$$

In this form, the Green's function has poles at the real eigenenergies, which are the main quantity in band structure calculations. The Green's function is often evaluated at complex energies $z = E + i\eta$, because it reduces the computational effort dramatically. This is explained in Sec. 3.1.2. The following definitions of Green's functions are common:

$$\mathcal{G}^{\pm}(z) = \lim_{\eta \to 0} (E\mathcal{I} \pm i\eta\mathcal{I} - \mathcal{H})^{-1}, \tag{A.20}$$

where the $+$ represents the retarded Green's function, and the $-$ represents the advanced Green's function. When not explicitly stated, we will use the retarded Green's function [24]. The retarded Green's function $G^{+}(x, x'; z)$ can be seen as an outward (away from the source) traveling wave function at point $x$, which was excited by a unit excitation at a point $x'$ [24]. The advanced Green's function $G^{-}(x, x'; z)$ repre-

sents waves traveling inward (to the source of excitation) at point $x$ due to the unit excitation at $x'$ [24].

## A.2.2. Dyson Equation

The Dyson equation plays a central role in the Green's function formalism since it enables us to calculate any Green's function of a system from a known one if the difference in potential is known. Suppose we have a reference system with

$$\mathcal{H}^0 = \hat{\mathbf{p}}^2 + \mathcal{V}^0(r), \tag{A.21}$$

where $\hat{\mathbf{p}}^2$ is the momentum operator and $\mathcal{V}^0(r)$ the potential of the reference system, and a system under consideration, that defers from the reference system only by the potential $\mathcal{V}(r)$, that is

$$\mathcal{H} = \mathcal{H}^0 + \mathcal{V}(r). \tag{A.22}$$

The solution of the reference system is given by the eigenvalue equation [103]

$$\mathcal{H}^0 \left| \psi^0 \right\rangle = E^0 \left| \psi^0 \right\rangle. \tag{A.23}$$

and the solution of the system under consideration by [103]

$$\mathcal{H} \left| \psi \right\rangle = E \left| \psi \right\rangle. \tag{A.24}$$

The solution of these equations can be formally written as operator relation [103]

$$\mathring{\mathcal{G}}(z) = (z\mathcal{I} - \mathcal{H}^0)^{-1} \qquad \text{and} \qquad \mathcal{G}(z) = (z\mathcal{I} - \mathcal{H})^{-1}. \tag{A.25}$$

The Green's functions[3] have to satisfy [103, 104]

$$(z - H^0)\mathring{G}(\mathbf{r}, \mathbf{r}', z) = \delta(\mathbf{r} - \mathbf{r}') \qquad \text{and} \qquad (z - H)G(\mathbf{r}, \mathbf{r}', z) = \delta(\mathbf{r} - \mathbf{r}'). \tag{A.26}$$

By making use of A.25 and A.22, we derive the Dyson equation [104]

$$\begin{aligned} 1 &= (z\mathbb{1} - H)G & \text{(A.27)} \\ &= (z\mathbb{1} - H^0 - V)G & \text{(A.28)} \\ &= (\mathring{G}^{-1} - V)G \quad | \, \mathring{G} \to & \text{(A.29)} \\ \mathring{G} &= G - \mathring{G}VG & \text{(A.30)} \\ \Leftrightarrow G &= \mathring{G} + \mathring{G}VG & \text{(A.31)} \end{aligned}$$

$$\begin{aligned} 1 &= (z\mathbb{1} - H^0)\mathring{G} & \text{(A.32)} \\ &= (z\mathbb{1} - H + V)\mathring{G} & \text{(A.33)} \\ &= (G^{-1} + V)\mathring{G} \quad | \, G \to & \text{(A.34)} \\ \Leftrightarrow G &= \mathring{G} + GV\mathring{G} & \text{(A.35)} \end{aligned}$$

The resulting equation is called *Dyson equation*. Since it is independent on the basis chosen, it reads in operator representation

$$\mathcal{G} = \mathring{\mathcal{G}} + \mathcal{G}\mathcal{V}\mathring{\mathcal{G}} = \mathcal{G} + \mathring{\mathcal{G}}\mathcal{V}\mathcal{G}. \tag{A.36}$$

The Dyson equation is an exact equation and not to be mistaken with perturbation theory.

---

[3]In the following, we will not distinguish anymore between the operator representation of the Green's function and the Green's function itself. Both, operator and function, will be called Green's function

### A.2.3. Lippmann-Schwinger Equation

A similar equation for the evolution of wave functions can be derived and is called the Lippmann-Schwinger equation [105]. The Lippmann-Schwinger equation relates a known wave function $\left|\psi^0\right\rangle$ to an unknown wave function $\left|\psi\right\rangle$ in a similar way as the Dyson equation does with the Green's function:

$$\left|\psi\right\rangle = \left|\psi^0\right\rangle + \mathcal{G}\mathcal{V}\left|\psi^0\right\rangle = \left|\psi^0\right\rangle + \mathring{\mathcal{G}}\mathcal{V}\left|\psi\right\rangle. \tag{A.37}$$

### A.2.4. $\mathcal{T}$-operator

The Dyson and Lippmann-Schwinger equations are often written in terms of the $\mathcal{T}$-operator. The formal solution of Eq. A.37 is given by [103]

$$\left|\psi\right\rangle = \left(\mathcal{I} - \mathring{\mathcal{G}}\mathcal{V}\right)^{-1}\left|\psi^0\right\rangle. \tag{A.38}$$

Defining the $\mathcal{T}$-operator as

$$\mathcal{T} = \mathcal{V}(\mathcal{I} - \mathring{\mathcal{G}}\mathcal{V})^{-1} \tag{A.39}$$

the resulting identity is

$$\mathcal{V}\left|\psi\right\rangle = \mathcal{T}\left|\psi^0\right\rangle. \tag{A.40}$$

The wave function $\left|\psi\right\rangle$ can be found by means of the $\mathcal{T}$-operator. The defining equation Eq. A.39 of the $\mathcal{T}$-operator can be written as

$$\mathcal{T} = \mathcal{V} + \mathcal{T}\mathring{\mathcal{G}}\mathcal{V}. \tag{A.41}$$

Inserting this result in itself repeatedly yields a so-called Born series as

$$\mathcal{T} = \mathcal{V} + \mathcal{V}\mathring{\mathcal{G}}\mathcal{V} + \mathcal{V}\mathring{\mathcal{G}}\mathcal{V}\mathring{\mathcal{G}}\mathcal{V} + \dots. \tag{A.42}$$

On the other hand, the Dyson equation $\mathcal{G} = \mathring{\mathcal{G}} + \mathcal{G}\mathcal{V}\mathring{\mathcal{G}}$ can also be expanded as a Born series, which yields [103, 105]

$$\mathcal{G} = \mathring{\mathcal{G}} + \mathring{\mathcal{G}}\mathcal{V}\mathring{\mathcal{G}} + \mathring{\mathcal{G}}\mathcal{V}\mathring{\mathcal{G}}\mathcal{V}\mathring{\mathcal{G}} + \dots \tag{A.43}$$

$$= \mathring{\mathcal{G}} + \mathring{\mathcal{G}}\left(\mathcal{V} + \mathcal{V}\mathring{\mathcal{G}}\mathcal{V} + \dots\right)\mathring{\mathcal{G}} \tag{A.44}$$

$$= \mathring{\mathcal{G}} + \mathring{\mathcal{G}}\mathcal{T}\mathring{\mathcal{G}}. \tag{A.45}$$

In other words, $\mathcal{G}$ can be determined by the Dyson equation via the $\mathcal{T}$ operator. Comparing Eq. A.36 to Eq. A.45 the relation

$$\mathcal{V}\mathcal{G} = \mathcal{T}\mathring{\mathcal{G}} \tag{A.46}$$

becomes apparent.

### A.2.5. Spectral Representation of the Green's Function

A useful way to represent the Green's function is the representation in the eigenbasis or spectral representation [18, 103]. From the defining equation

$$\mathcal{G}(z\mathcal{I} - \mathcal{H}) = \mathcal{I} \tag{A.47}$$

the Matrix elements $\langle \varphi | \mathcal{G} | \varphi' \rangle$ can be evaluated. Introducing the eigenbasis $|\varphi\rangle$ of the Hamiltonian $\mathcal{H}$ the equation can be written as [18]

$$\langle \varphi | \mathcal{G}(z\mathcal{I} - \mathcal{H}) | \varphi' \rangle = \oint \langle \varphi | \mathcal{G} | \varphi'' \rangle \langle \varphi'' | z\mathcal{I} - \mathcal{H} | \varphi' \rangle \, \mathrm{d}\varphi'' \tag{A.48}$$

$$= \oint \langle \varphi | \mathcal{G} | \varphi'' \rangle (z - E_{\varphi'}) \langle \varphi'' | \varphi' \rangle \, \mathrm{d}\varphi'' \tag{A.49}$$

$$= \langle \varphi | \mathcal{G} | \varphi' \rangle (z - E_{\varphi'}) \qquad\qquad = \langle \varphi | \mathcal{I} | \varphi' \rangle \tag{A.50}$$

$$= \delta(\varphi - \varphi') \tag{A.51}$$

from which the matrix element

$$\langle \varphi | \mathcal{G} | \varphi' \rangle = \frac{\delta(\varphi - \varphi')}{z - E_{\varphi'}} \tag{A.52}$$

can be obtained [18]. Using $\mathcal{I} = \oint |\varphi\rangle \langle \varphi|$ on both sides of $\mathcal{G}$ the spectral representation can be obtained

$$\mathcal{G} = \oiint |\varphi\rangle \langle \varphi | \mathcal{G} | \varphi' \rangle \langle \varphi' | \, \mathrm{d}\varphi \mathrm{d}\varphi' = \oint \frac{|\varphi\rangle \langle \varphi|}{z - E_{\varphi}} \mathrm{d}\varphi. \tag{A.53}$$

## A.2.6. Physical Observables

From the Green's function the electron density defined as [18, 103]

$$n(\mathbf{r}, E) = 2 \sum_{\mathbf{k}} |\varphi_{\mathbf{k}}(\mathbf{r})|^2 \delta(E - E_{\mathbf{k}}) \tag{A.54}$$

can be calculated as it contains all the necessary information about the system under consideration, especially the eigenstates and eigenenergies. Using the Dirac identity [103]

$$\lim_{\eta \to 0^+} \frac{1}{E \pm i\eta - E_{\mathbf{k}}} = \mp \pi i \delta(E - E_{\mathbf{k}}) + \mathcal{P}\left(\frac{1}{E - E_{\mathbf{k}}}\right), \tag{A.55}$$

where $\mathcal{P}(x)$ is the Cauchy principal value, we can relate the Green's function via the spectral representation

$$\mathcal{G}(E) = \lim_{\eta \to 0^+} \int \frac{|\varphi\rangle \langle \varphi|}{E + i\eta - E_{\varphi}} \mathrm{d}\varphi \tag{A.56}$$

$$= -\pi i \int |\varphi\rangle \langle \varphi | \delta(E - E_{\mathbf{k}}) \mathrm{d}\varphi + \int |\varphi\rangle \langle \varphi | \mathcal{P}\left(\frac{1}{E - E_{\mathbf{k}}}\right) \mathrm{d}\varphi \tag{A.57}$$

to the density operator $\hat{n}(E)$ via

$$\hat{n}(E) = \int |\varphi\rangle \langle \varphi | \delta(E - E_{\varphi}) \mathrm{d}\varphi = \frac{i}{2\pi}(\mathcal{G} - \mathcal{G}^\dagger) = -\frac{1}{\pi} \operatorname{Im} \mathcal{G}. \tag{A.58}$$

With this, it is easy to calculate the spatial electron density as

$$n(\mathbf{r}) = \int_{-\infty}^{\infty} f(E) \langle \mathbf{r} | \hat{n}(E) | \mathbf{r} \rangle \, \mathrm{d}E = -\frac{1}{\pi} \int_{-\infty}^{E_F} \operatorname{Im} G(\mathbf{r}, \mathbf{r}; E) \mathrm{d}E \tag{A.59}$$

and the density of states

$$n(E) = \int_V \langle \mathbf{r} | \hat{n}(E) | \mathbf{r} \rangle \, \mathrm{d}V = -\frac{1}{\pi} \int \mathrm{Im} \, G(\mathbf{r}, \mathbf{r}, E) \, \mathrm{d}V. \tag{A.60}$$

The evaluation of Eq. A.59 is done along a path in the complex plane for numerical reasons and is described in Sec. 3.1.2

## A.3. Korringa-Kohn-Rostoker Formalism

### A.3.1. Cell-Centered Coordinates and Atomic Sphere Approximation

In order to make use of the spherical nature of the atomic potential and to approximate the potential in the crystal, the space is divided into spheres. Each of these spheres originates at the center of an atom. There are two common possibilities to construct the spheres: In the muffin tin method, the spheres are extended such that they touch each other and the second method is the atomic sphere approximation (ASA), in which the spheres are extended to a size that the volume of all spheres equals the volume of the unit cell [84, 104]. This causes overlap of the spheres and therefore leads to double counting contributions. However, due to the equality of volumes, it is sufficient to evaluate the volume integral for the electronic density only for the atomic spheres and no interstitial regions have to be considered [104].
The cell-centered coordinates transform as follows:

$$\mathbf{r} \to \mathbf{r} + \mathbf{R}_n; \qquad \mathbf{r}' \to \mathbf{r}' + \mathbf{R}_{n'}. \tag{A.61}$$

The upper-case vectors $\mathbf{R}_n$ point to the origin of an ASA sphere and the lower-case vectors $\mathbf{r}$ point to a location restricted to the inside of the ASA sphere.
It is also possible to divide the space into polyhedral cells. Each polyhedral cell is divided into a sphere with a muffin tin radius and the "interstitial" part inside the polyhedron. In both sections, the potential is now comprised of a spherical part and a part that is described by higher order $(\ell, m)$ expansions after spherical harmonics $Y_{lm}(\hat{\mathbf{r}})$. The polyhedra are truncated by a shape function $\Theta$, which is 1 if a point lies inside the polyhedron and 0 otherwise. This approach is called full potential approach and is described in [105–107]. The potential is given by Eq. A.75.

### A.3.2. Green's Function of the Free System

The Green's function of the free system in the KKR is expanded in spherical Bessel functions [105]. Since they are eigenfunctions of the Hamiltonian, the spectral representation from Eq. A.53 can be used to represent the Green's function of the free system [105]

$$\mathring{G}(\mathbf{r}, \mathbf{r}', z) = \int_0^\infty \mathrm{d}E \sum_L \frac{\sqrt{E}}{\pi} \frac{j_L(E, \mathbf{r}) j_L(E, \mathbf{r}')^*}{z - E}. \tag{A.62}$$

Here, $(\ell, m) \to L := \ell^2 + \ell + m + 1$ is the combined index of the orbital momentum $\ell$ and the magnetic quantum number $m$, respectively. Further, the notation

$$f_L(z, \mathbf{r}) = f_\ell(\sqrt{z}r) Y_L(\hat{\mathbf{r}}) \tag{A.63}$$

and

$$f_L(z, \mathbf{r})^\times = f_\ell(\sqrt{z}r)Y_L(\hat{\mathbf{r}})^* \tag{A.64}$$

is used for the product of, for example, a spherical Bessel function $j_\ell(\sqrt{z}r)$ (or later the spherical Hankel function $h_\ell^+(\sqrt{z}r)$) with a spherical harmonic $Y_L(\hat{\mathbf{r}})$. The vecotr $\hat{\mathbf{r}}$ is the unit vector of the position vector $\mathbf{r}$. Integrating this equation yields the single-center solution [105]

$$\mathring{g}(\mathbf{r}, \mathbf{r}', z) = -i\sqrt{z}\sum_L j_\ell(\sqrt{z}r_<)h_\ell^+(\sqrt{z}r_>)Y_L(\hat{\mathbf{r}})Y_L(\hat{\mathbf{r}}')^*. \tag{A.65}$$

Here, the smaller or greater norm of the vectors $\mathbf{r}$ and $\mathbf{r}'$ are used, that is $r_< = \min(r, r')$ and $r_> = \max(r, r')$. When the vectors $\mathbf{r}$ and $\mathbf{r}'$ originate in two different cells (two-center solution), cell-centered coordinates are used. Since $\mathring{G}(\mathbf{r} + \mathbf{R}_n, \mathbf{r}' + \mathbf{R}_m, z) = \mathring{G}(\mathbf{r} - \mathbf{r}', \mathbf{R}_n - \mathbf{R}_m; z)$ only depends on the differences between the position vectors and the centering vectors, the following expansion holds true [105]

$$\mathring{G}(\mathbf{r} + \mathbf{R}_n, \mathbf{r}' + \mathbf{R}_m, z) = -i\sqrt{z}\sum_L h_L^+(z, \mathbf{R}_n - \mathbf{R}_m)j_L(z, \mathbf{r} - \mathbf{r}')^\times. \tag{A.66}$$

By using an expansion for

$$j_L(z, \mathbf{r} - \mathbf{r}')^\times = 4\pi\sum_{L',L''} i^{\ell'-\ell''-\ell} j_{L'}(z, \mathbf{r})j_{L''}(z, \mathbf{r}')^\times C_{LL'}^{L''} \tag{A.67}$$

with the Gaunt coefficients

$$C_{LL'}^{L''} = \int \mathrm{d}\Omega_{\mathbf{k}}\, Y_L(\hat{\mathbf{k}})Y_{L'}(\hat{\mathbf{k}})Y_{L''}^*(\hat{\mathbf{k}}), \tag{A.68}$$

where $\mathrm{d}\Omega_{\mathbf{k}}$ denotes the spherical angle element in $\mathbf{k}$-space, and $\hat{\mathbf{k}}$ the direction of $\mathbf{k}$, the Green's function can finally be rewritten as [105]

$$\mathring{G}(z, \mathbf{r} + \mathbf{R}_n, \mathbf{r}' + \mathbf{R}_m) = -4\pi\sqrt{z}i\sum_{L,L',L''} h_L^+(z, \mathbf{R}_n - \mathbf{R}_m)i^{\ell'-\ell''-\ell} \tag{A.69}$$

$$\times j_{L'}(z, \mathbf{r})j_{L''}(z, \mathbf{r}')^\times C_{LL'}^{L''}. \tag{A.70}$$

Finally, the complete form of the Green's function can be written as the sum of the single-center and the two-center expansion as [18, 105]

$$\mathring{G}(z, \mathbf{r} + \mathbf{R}_n, \mathbf{r}' + \mathbf{R}_m) = (1 - \delta_{nm})\sum_{LL'} j_L(z, \mathbf{r})\mathring{G}_{LL'}^{nm}j_{L'}(z, \mathbf{r}')^\times \tag{A.71}$$

$$- i\sqrt{z}\delta_{nm}\sum_L j_L(z, \mathbf{r}_<)h_L^+(z, \mathbf{r}_>) \tag{A.72}$$

with the so-called real-space structure constants

$$\mathring{G}_{LL'}^{nm}(z) = -4\pi\sqrt{z}i\sum_{L''} i^{\ell-\ell'-\ell''} h_{L''}^+(z, \mathbf{R}_n - \mathbf{R}_m)C_{LL''}^{L'}. \tag{A.73}$$

We see here that the spherical Bessel functions enter as a regular solution to the radial Schrödinger equation and the spherical Hankel functions as irregular solutions. The

solution of the multiple scattering problem later will also consist of a regular and an irregular solution in analogy to the Green's function of free electrons.

### A.3.3. Single Scatterering

First, we consider a single scattering potential cut at a specific radius, which is called the ASA or muffin tin radius. The corresponding Hamiltonian reads (in atomic units) [103]

$$H = -\nabla^2 + V(\mathbf{r}),$$ (A.74)

where $V(\mathbf{r})$ is the single scattering potential defined as [103]

$$V(r) = \begin{cases} V_{\mathrm{MT}}(r) & r < R_{\mathrm{ASA}} \\ V_0 & r > R_{\mathrm{ASA}} \end{cases}.$$ (A.75)

Usually, $V_0$ can be chosen to be 0, but in practice, for matters of the multiple scattering with different species of elements, $V_0$ is chosen such that the overall discontinuities at the muffin tin radius are minimized for all potentials. To solve the problem we use that $V(\mathbf{r}) \equiv V(r)$ is a central potential. Thus we can separate the solution $\psi_L(\mathbf{r})$ of the eigenvalue problem

$$H\psi_L(\mathbf{r}) = E\psi_L(\mathbf{r})$$ (A.76)

into

$$\psi_L(\mathbf{r}) = R_\ell(r, E) Y_L(\hat{\mathbf{r}}).$$ (A.77)

$Y_L(\hat{\mathbf{r}})$ are the real spherical harmonics. The final problem remains to find the radial part $R_\ell(r, E)$ of the wave function. Therefore the radial Schrödinger equation has to be solved [103]:

$$\left( -\frac{\mathrm{d}^2}{\mathrm{d}r^2} - \frac{2}{r}\frac{\mathrm{d}}{\mathrm{d}r} + \frac{\ell(\ell+1)}{r^2} + V(r) - E \right) R_\ell(r, E) = 0.$$ (A.78)

Where the potential is 0, that is, outside the muffin tin radius, the solution is a superposition of regular and irregular solutions, which are the spherical Bessel and Neumann functions, respectively. The remaining phase shifts for the outer solution are determined by continuity conditions of the wave function at the boundary $R_{\mathrm{ASA}}$ [103].
Inside the muffin tin radius, from the Lippmann-Schwinger equation we get [103]

$$\psi(\mathbf{r}) = \langle \mathbf{r} | \psi \rangle = \langle \mathbf{r} | \psi^0 \rangle + \int \langle \mathbf{r} | \mathring{\mathcal{G}} \mathcal{V} | \mathbf{r}' \rangle \langle \mathbf{r}' | \psi \rangle \, \mathrm{d}\mathbf{r}'$$ (A.79)

$$= \psi^0(\mathbf{r}) + \int \mathring{G}(\mathbf{r}, \mathbf{r}', z) V(\mathbf{r}') \psi(\mathbf{r}') \, \mathrm{d}\mathbf{r}'.$$ (A.80)

Now, in the case of the single scattering potential, we can calculate the radial solution of the radial Schrödinger equation by using the radial eigenfunctions of the free system, the spherical Bessel functions. This yields [103, 108]

$$R_\ell(r, z) = j_\ell(\sqrt{z}r) + \int \mathring{G}(r, r', z) V(r') R_\ell(r', z) \, r'^2 \, \mathrm{d}r'.$$ (A.81)

Together with the irregular solution $H_l^+(r, z)$, that is necessary, as it can be seen already by the Green's function for the free system, the single site Green's function can be obtained as [103, 108]

$$g^n\left(\mathbf{r} + \mathbf{R}_n; \mathbf{r}' + \mathbf{R}_n; E\right) = \sqrt{E} \sum_L R_\ell(r_<, E) H_\ell^+(r_>, E) Y_L(\hat{\mathbf{r}}) Y_L^*(\hat{\mathbf{r}}') \tag{A.82}$$

using the regular and irregular solutions from the single scatterer problem.

Instead of using the Lippmann-Schwinger like Eq. A.81, in practice, the wave function is solved numerically by means of a predictor-corrector algorithm with in- and outward integration. Both the regular solution $R_L(r, z)$ and irregular solution $H_L^+(r, z)$ are retrieved [105].

## A.3.4. Multiple Scattering

In a crystal, the situation is more complicated as several atoms are placed on different sites and contribute to the overall potential. We, therefore, consider here a superposition of potentials centered in ASA spheres as [103]

$$V(\mathbf{r}) = \sum_n V\left(|\mathbf{r} - \mathbf{R}_n|\right) = \sum_n V_n(\mathbf{r}). \tag{A.83}$$

From here, it is convenient to use the cell-centered coordinates as introduced before. The corresponding Schrödinger equation for ASA sphere $n$ now reads [103]

$$\left(-\nabla^2 + V_n(r) - E\right) G\left(\mathbf{r} + \mathbf{R}_n; \mathbf{r}' + \mathbf{R}_{n'}; E\right) = -\delta_{nn'}\delta\left(\mathbf{r} - \mathbf{r}'\right). \tag{A.84}$$

This equation is homogenous if we look at two separate cells $\mathbf{R}_n \neq \mathbf{R}_{n'}$. Then we can expand the Green's function in the basis of the radial solutions $R_\ell$ of the Schrödinger equation. If, however, we look at scattering events inside the cell, we know the solution already as it is the solution for the single scatterer as before. The full solution, therefore, reads [103]

$$G\left(\mathbf{r} + \mathbf{R}_n; \mathbf{r}' + \mathbf{R}_{n'}; E\right) = \delta_{nn'} g^n\left(\mathbf{r} + \mathbf{R}_n; \mathbf{r}' + \mathbf{R}_n; E\right) \tag{A.85}$$

$$+ \sum_{L,L'} R_L(\mathbf{r}, E) G_{LL'}^{nn'}(E) R_{L'}^{n'}(\mathbf{r}', E), \tag{A.86}$$

where the first part is called the single scattering solution and the second part is called the multiple scattering solution. The coefficients $G_{LL'}^{nn'}(E)$ are the structural Green's functions, which happen to contain all the information of the multiple scattering [103].

### Algebraic Dyson Equation

Now that we have expressions for the Green's functions, we can relate them to each other via the Dyson equation (Eq. A.36). Inserting the two expressions for the Green's function and the Green's function of the free system yields the Dyson equation for the single scatterer [103]

$$g(\mathbf{r}, \mathbf{r}', z) = \mathring{g}(\mathbf{r}, \mathbf{r}', z) + \mathring{g}(\mathbf{r}, \mathbf{r}', z) \Delta V g(\mathbf{r}, \mathbf{r}', z) \tag{A.87}$$

and a Dyson-like equation for the structural Green's function [103]

$$G_{LL'}^{nn'}(z) = \mathring{G}_{LL'}^{nn'}(z) + \sum_{L''} \sum_{n''} \mathring{G}_{LL''}^{nn''}(z) \Delta t_{\ell''}^{n''}(z) G_{L''L'}^{n''n'}(z), \tag{A.88}$$

which is called *algebraic Dyson equation*.
Here the difference of two $\mathcal{T}$-operators is introduced

$$\Delta t_\ell^n(E) = t_\ell^n(E) - \left(t^0\right)_\ell^n(E). \tag{A.89}$$

The matrix elements $t_\ell(E)$ of the $\mathcal{T}$-operators are defined as follows [103]:

$$t_\ell(z) = \langle j_\ell | \mathcal{T} | j_\ell \rangle = \langle j_\ell | \mathcal{V} | R_\ell \rangle = \int \mathrm{d}r r^2 j_\ell(\sqrt{E}r) V(r) R_\ell(r, E). \tag{A.90}$$

The algebraic Dyson equation is the equation at the core of the KKR formalism. A formal solution of the algebraic Dyson equation is

$$G = (1 - \mathring{G}\Delta t)^{-1} \mathring{G}. \tag{A.91}$$

This equation is, however, not exactly the equation that is solved, but there are several further considerations to take into account like the translational invariance of the crystal or the transport geometry for the non-equilibrium formalism.

### A.3.5. Further Remarks

**Translational Invariance of the Ideal Crystal**

The systems under consideration normally are ideal crystals, that is, they possess a translational invariance. This translational invariance can be made use of by [104, 109]

$$\mathring{G}_{LL'}^{\mu\mu'nn'}(E) = \frac{\Omega}{(2\pi)^3} \int_{\Omega_{\mathrm{BZ}}} \mathrm{d}^3 k \exp\left(-i\mathbf{k}\mathbf{R}^{nn'}\right) \mathring{G}_{LL'}^{\mu\mu'}(\mathbf{k}, E). \tag{A.92}$$

$\Omega$ is the volume of the real space unit cell, and $\Omega_{\mathrm{BZ}}$ is the volume of the Brillouin zone. Here, two additional indices $\mu$ and $\mu'$ are introduced, which refer to the basis of the unit cell. The indices $n$ and $n'$ now refer to the unit cell [104].
The lattice Fourier transformation finally yields the formal solution for the structure constants [104]

$$G_{LL'}^{\mu\mu'}(\mathbf{k}, E) = \sum_{\mu''L''} \left[\left(1 - \mathring{G}(\mathbf{k}, E)\Delta t\right)^{-1}\right]_{LL''}^{\mu\mu''} \mathring{G}_{LL''}^{\mu\mu''}(\mathbf{k}, E). \tag{A.93}$$

It is computationally more efficient though – instead of solving Eq. A.93 directly – to invert the so called KKR matrix [109–111]

$$M_{LL'}^{\mu\mu'}(\mathbf{k}, E) = \mathring{G}_{LL'}^{nn'}(\mathbf{k}, E) - \delta_{nn'}\delta_{LL'}\left((\Delta t)^{-1}(E)\right)_L^\mu \tag{A.94}$$

and calculate the $\mathbf{k}$ dependant structure constants from this matrix. Using a back-transformation, the real-space structure constants can be obtained.

**Screened KKR**

Usually, when the Green's function for the reference system, that is, the free system, is calculated, many atoms have to be included because of the long-range interactions from the Coulomb potentials. For convergence of the calculations, many atomic spheres inside a cluster must be considered until the decreasing contributions can be ignored. Since the Dyson equation is in-principle exact, any reference system can be chosen. The Dyson equation for the system under consideration can be solved via two steps: from the free electrons to the reference and from the reference system to the final solution. When choosing a highly-repulsive reference system, the Green's function of this repulsive system decays exponentially in real space so that clusters with smaller radii containing much less atoms can be used. This reduces the computational demand very drastically.

Care must be taken of the states introduced by the reference system. If the reference system is not chosen to be reasonably repulsive, states of that system can exist within the energy contour used for the calculation of the density $n(\mathbf{r})$. However, since the reference potential is highly repulsive, the states of the reference system lie high enough to not interfere with actual states of the physical system [109, 112].

Only with the screened KKR is it possible to achieve a tight-binding like banded matrix structure of the KKR matrix $M_{LL'}^{\mu\mu'}(\mathbf{k}, E)$ in the transport geometry [104, 110]. The banded matrix is necessary because of the employed solution strategy for the infinite matrix in the transport geometry. This will be discussed later.

**2D-translational invariant systems**

In the transport geometry for the non-equilibrium formalism, the transport direction will be solved in real space by the decimation technique since tunnel barriers break the translational invariance in the transport direction. Instead of a full Fourier transformation, only the in-plane components of the plane perpendicular to the transport direction will be Fourier transformed. Therefore, the in-plane wave vector $\mathbf{k}_\parallel$ is introduced. Further description of this procedure can be found in [104, 105, 110].

## A.3.6. Spin-Polarized and Non-Collinear KKR

To account for magnetic systems, the Kohn-Sham Hamiltonian can be extended by an effective magnetic field term [108]

$$H = \left(-\nabla^2 + V_{\text{eff}}(\mathbf{r})\right) \mathbb{1}_2 + \mu_B \underline{\underline{\Xi}} \mathbf{B}_{\text{eff}}(\mathbf{r}) \tag{A.95}$$

with the effective magnetic field

$$\mathbf{B}_{\text{eff}}(\mathbf{r}) = \mathbf{B}_{\text{ext}}(\mathbf{r}) + \frac{\delta E_{xc}}{\delta \mathbf{m}(\mathbf{r})} \tag{A.96}$$

and

$$\underline{\underline{\Xi}} = \begin{pmatrix} \xi & 0 \\ 0 & \xi \end{pmatrix}, \qquad \xi = (\xi_x, \xi_y, \xi_z), \tag{A.97}$$

where $\xi_x$, $\xi_y$, $\xi_z$ are the conventional Pauli spin matrices. Instead of only the electronic density $n(\mathbf{r})$, now also the magnetization $\mathbf{m}(\mathbf{r})$ enters into the description. The theory can now be reformulated in terms of the spin density matrix

$$\underline{n}(\mathbf{r}) = \frac{1}{2} \left( n(\mathbf{r})\mathbb{1}_2 + \underline{\Xi} \cdot \mathbf{m}(\mathbf{r}) \right), \tag{A.98}$$

which is a $2 \times 2$ matrix in the spin space [113].

In the collinear case, this matrix becomes diagonal, and hence it just remains to solve the problem for each spin direction seperately [108]. In the case of non-collinearity, the spin density matrix is not diagonal anymore. Instead, the spin density matrix has to be transformed into a local frame in which the spin density matrix is diagonal, then solved and finally rotated back [108]. Details on the formalism for the collinear and the non-collinear case can be found in Ref. [105, 108]

## A.3.7. Full-Relativistic KKR Formalism

In order to describe the spin Hall effect, a correct inclusion of the spin-orbit coupling plays a central role. The influences of spin-orbit coupling are best described in a full-relativistic framework. Instead of the Kohn-Sham equations, now the Kohn-Sham-Dirac equation is solved [105]. The corresponding Kohn-Sham-Dirac Hamiltonian reads [105]

$$H = c\underline{\alpha}\mathbf{p} + \underline{\beta}mc^2 + V_{\text{eff}}(\mathbf{r})\mathbb{1}_4 + \underline{\beta}\underline{\Xi} \cdot \mathbf{B}_{\text{eff}}(\mathbf{r}). \tag{A.99}$$

Here,

$$\underline{\alpha} = \begin{pmatrix} 0 & \xi \\ \xi & 0 \end{pmatrix}, \qquad \underline{\beta} = \begin{pmatrix} \mathbb{1}_2 & 0 \\ 0 & -\mathbb{1}_2 \end{pmatrix}. \tag{A.100}$$

The solutions

$$\psi(E,\mathbf{r}) = \sum_{\kappa\mu} \begin{pmatrix} g_{\kappa\mu}(E,r)\chi_{\kappa\mu}(\hat{\mathbf{r}}) \\ if_{\kappa\mu}(E,r)\chi_{-\kappa\mu}(\hat{\mathbf{r}}) \end{pmatrix} \tag{A.101}$$

consist of a combination of bi-spinors $g_{\kappa\mu}(E,r)$ and $f_{\kappa\mu}(E,r)$, and the spin spherical harmonics $\chi_{\kappa\mu}(\hat{\mathbf{r}})$ [105]. Instead of the angular quantum numbers $(\ell, m) \rightarrow L$, the relativistic angular momentum quantum numbers $(\kappa, \mu) \rightarrow Q$ are used [105].

Inserting this ansatz and integrating the angular parts yields the following equation [105]

$$\sum_{Q'} \begin{pmatrix} W - mc^2 - U_{QQ'}^+(r) & -i\hbar c \left[ \frac{\mathrm{d}}{\mathrm{d}r} + \frac{1}{r} - \frac{\kappa}{r} \right] \\ -i\hbar c \left[ \frac{\mathrm{d}}{\mathrm{d}r} + \frac{1}{r} + \frac{\kappa}{r} \right] & W + mc^2 - U_{QQ'}^-(r) \end{pmatrix} \begin{pmatrix} g_{Q'}(r) \\ if_{Q'}(r) \end{pmatrix} = 0 \tag{A.102}$$

with

$$U_{QQ'}^{\pm}(r) = \langle \pm\kappa, \mu | V_{\text{eff}}(\mathbf{r}) \pm \xi \cdot \mathbf{B}_{\text{eff}}(\mathbf{r}) | \pm\kappa', \mu' \rangle, \tag{A.103}$$

and the relativistic dispersion relation $W^2 = c^2p^2 + m^2c^4$, where $p$ is the momentum, $c$ the speed of light, and $m$ the rest mass. This system of equations can be solved numerically and the resulting regular and irregular solutions can be used to calculate the final Green's function in analogy to the non-relativistic case [105, 108]

$$G(\mathbf{r},\mathbf{r}';z) = \delta_{nm} \sum_Q R_Q^n(\mathbf{r}_<,z)H_Q^n(\mathbf{r}_>,z)^\times + \sum_{QQ'} R_Q^n(\mathbf{r},z)G_{QQ'}^{nm}(z)R_{Q'}^m(\mathbf{r}',z)^\times. \tag{A.104}$$

**Green's Function of the Free System**

The Green's function for the free system can be written in analogy to the non-relativistic case [105]

$$
\mathring{G}(E, \mathbf{r} + \mathbf{R}_n, \mathbf{r}' + \mathbf{R}_m) = (1 - \delta_{nm}) \sum_{QQ'} j_Q(E, \mathbf{r}) \mathring{G}_{QQ'}^{nm} j_{Q'}(E, \mathbf{r}')^{\times}
$$
$$
- i\sqrt{E} \delta_{nm} \sum_Q h_Q^+(E, \mathbf{r}_<) j_Q(E, \mathbf{r}_>)^{\times}. \qquad (A.105)
$$

Here, the notation

$$
f_Q(E, \mathbf{r})^{\times} = \left[ f_\ell(pr/\hbar) \chi_{\kappa\mu}(\hat{\mathbf{r}}), \frac{iS_\kappa pc}{W + mc^2} f_{\bar{\ell}}(pr/\hbar) \chi_{-\kappa\mu}(\hat{\mathbf{r}}) \right], \qquad (A.106)
$$

with $S_\kappa = \frac{\kappa}{|\kappa|}$, $\bar{\ell} = \ell - S_\kappa$, and $p = \sqrt{W^2 - m^2c^4}$, is used as an abbreviation for the product of the spherical Bessel or Hankel functions with the spin spherical harmonics $\chi_{\kappa\mu}(\hat{\mathbf{r}})$ in the big and small component.

**Electronic and Magnetic Density**

For the equilibrium case, the electronic density is finally given by [105]

$$
n(\mathbf{r}) = -\frac{1}{\pi} \operatorname{Im} \int_{-\infty}^{E_F} \langle \mathbf{r} | \operatorname{Tr}(G(E)\mathbb{1}_4)) | \mathbf{r} \rangle \, \mathrm{d}E \qquad (A.107)
$$

and the $i$-th component of the spin magnetic moment by [105]

$$
m_i(\mathbf{r}) = -\frac{\mu_B}{\pi} \operatorname{Im} \int_{-\infty}^{E_F} \langle \mathbf{r} | \operatorname{Tr}\big(G(E)\underline{\beta}\underline{\Xi}_i\big) | \mathbf{r} \rangle \, \mathrm{d}E. \qquad (A.108)
$$

Integrating the magnetic density over the Volume $V_\mu$ of corresponding atomic sphere $\mu$ yields the magnetic moment $a_i(\mu)$ in this sphere as

$$
a_i(\mu) = \int_{V_\mu} m_i(\mathbf{r}) \, \mathrm{d}V. \qquad (A.109)
$$

Further, more intricate theoretical details can be found in Refs. [84, 105, 108].

# B. Supplemental Information to Phys. Rev. B 104, 054402, (2021)

# Supplemental Material:
# Spin accumulation from non-equilibrium first principles methods

Alexander Fabian, Michael Czerner, and Christian Heiliger

*Institute for Theoretical Physics, Justus Liebig University Giessen,*
*Heinrich-Buff-Ring 16, 35392 Giessen, Germany and*
*Center for Materials Research (LaMa), Justus Liebig University Giessen,*
*Heinrich-Buff-Ring 16, 35392 Giessen, Germany*

Hugo Rossignol and Ming-Hung Wu

*HH Wills Physics Laboratory, University of Bristol, Tyndall Avenue BS8 1TL, United Kingdom*

Martin Gradhand

*HH Wills Physics Laboratory, University of Bristol, Tyndall Avenue BS8 1TL, United Kingdom and*
*Institute of Physics, Johannes Gutenberg University Mainz, 55099 Mainz, Germany*

## CONTENTS

## ORGANIZATION

The supplemental information is organized as follows: In section I we show the calculated accumulation for all small systems considered in the main text. In section II we show the accumulation for larger systems of Cu, Pt, and U. We make a short remark on the behavior of U. In section III we conclude the supplemental information by showing the Fermi surfaces of the considered systems with colour coded group velocity.

# I. ACCUMULATIONS FOR SMALL SYSTEMS

The accumulation of all the small (3 atomic layers) systems is depicted in Fig. 1 for the fcc (Ag, Au, Cu, Pd, Pt) and Fig. 2 for the bcc systems (Ta, U) for all elements considered in the main text. The blue lines are calculated via the Boltzmann formalism, the red lines are calculated via the Keldysh formalism. The accumulation shows qualitatively the same symmetry enforced anti-symmetric behaviour in both methods. The trend between the elements is quite consistent for both methods. The sign change in the accumulation for U and Ta is consistent in both methods. For a detailed discussion refer to the main text. For an overview of the trend refer to Table I of the main text.
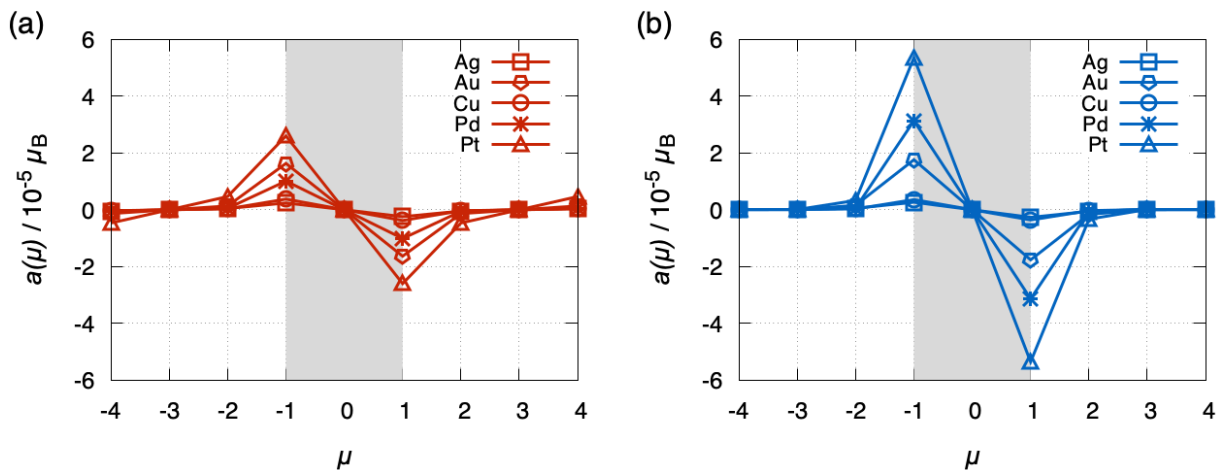


Figure 1. Plot of the magnetic moment per atom for the fcc systems. (a) Keldysh, (b) Boltzmann. The thin film is highlighted in grey. Each line shows the same antisymmetric behaviour. The agreement of (a) and (b) between Cu, Ag, and Au is better than for Pd and Pt.
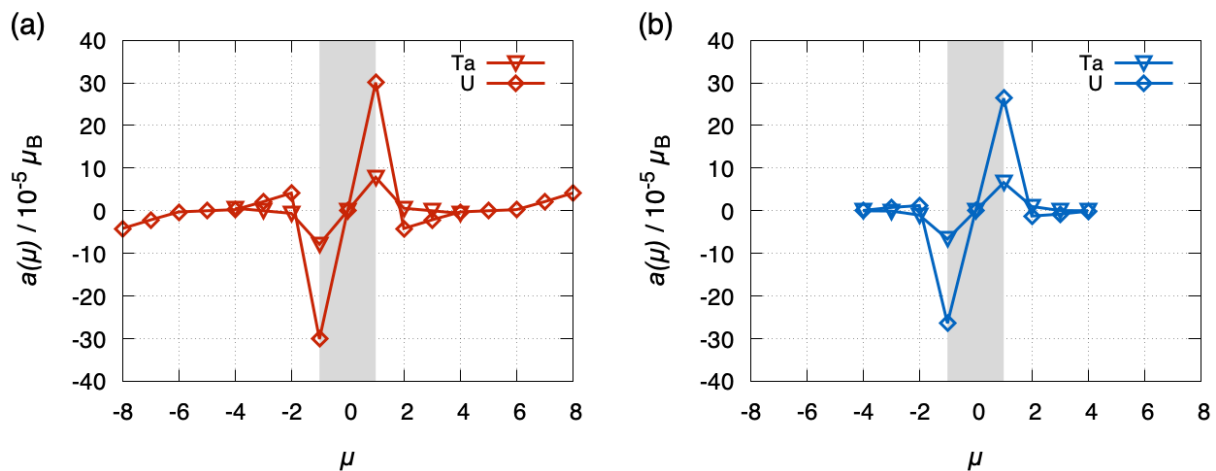


Figure 2. Plot of the magnetic moment per atom for the bcc systems. (a) Keldysh, (b) Boltzmann. The thin film is highlighted in grey. Each line shows the same antisymmetric behaviour. The sign of the first extremum is changed compared to the systems with fcc lattice. The agreement of the absolute values is not of the same order as for Cu, Ag, and Au.

## II.   ACCUMULATIONS FOR LARGE SYSTEMS

The accumulations of the large systems (9 atomic layers) are depicted in Fig. 3. The behavior in (a) for Cu shows the best agreement between the two methods. The decay length of the accumulation is rather short compared to U and Pt. Pt in Fig. 3 (b) shows a good agreement in extremal values, which may be a coincidence here, since for the small systems of Pt the extremal values differ by factor of roughly 2. The inner structure of the magnetization accumulation, differs more than that of Cu. For U in (c) with a more complex Fermi surface, the extremal values differ in sign. Additionally, U shows a more complex inner structure in the accumulation, which also differs between the two methods. We attribute the sign change which appears in the Keldysh calculation to finite size effects, since this deviation does not occur for a thinner system with 7 atomic U layers or a larger system of 11 atomic U layers. This is depicted in Fig. 4 (a) and (c). For comparison, the system with 9 atomic U layers is depicted in Fig. 4 (b) as well. The absolute extremal values match rather well, but especially for the 9 layer system and the 11 layer system the inner structure does differ significantly. While the extremal value of accumulation of Cu tends to decrease compared to the thin film with 3 layers, the extremal values for Pt increase in both methods. In the case of U, compared to the very thin film, each system shows a smaller extremal value. However, this extremal value is increasing from the 7 layer system to the 11 layer system except only for the 9 layer Boltzmann calculation. Also, the position of the extremal value slightly changes compared between Keldysh and Boltzmann. Again, we attribute this also to the strong influence of finite size effects in very thin films. However, the trend between the three systems remains qualitatively the same. For a detailed comparison of the smaller systems refer to the main text and Table I in the main text.
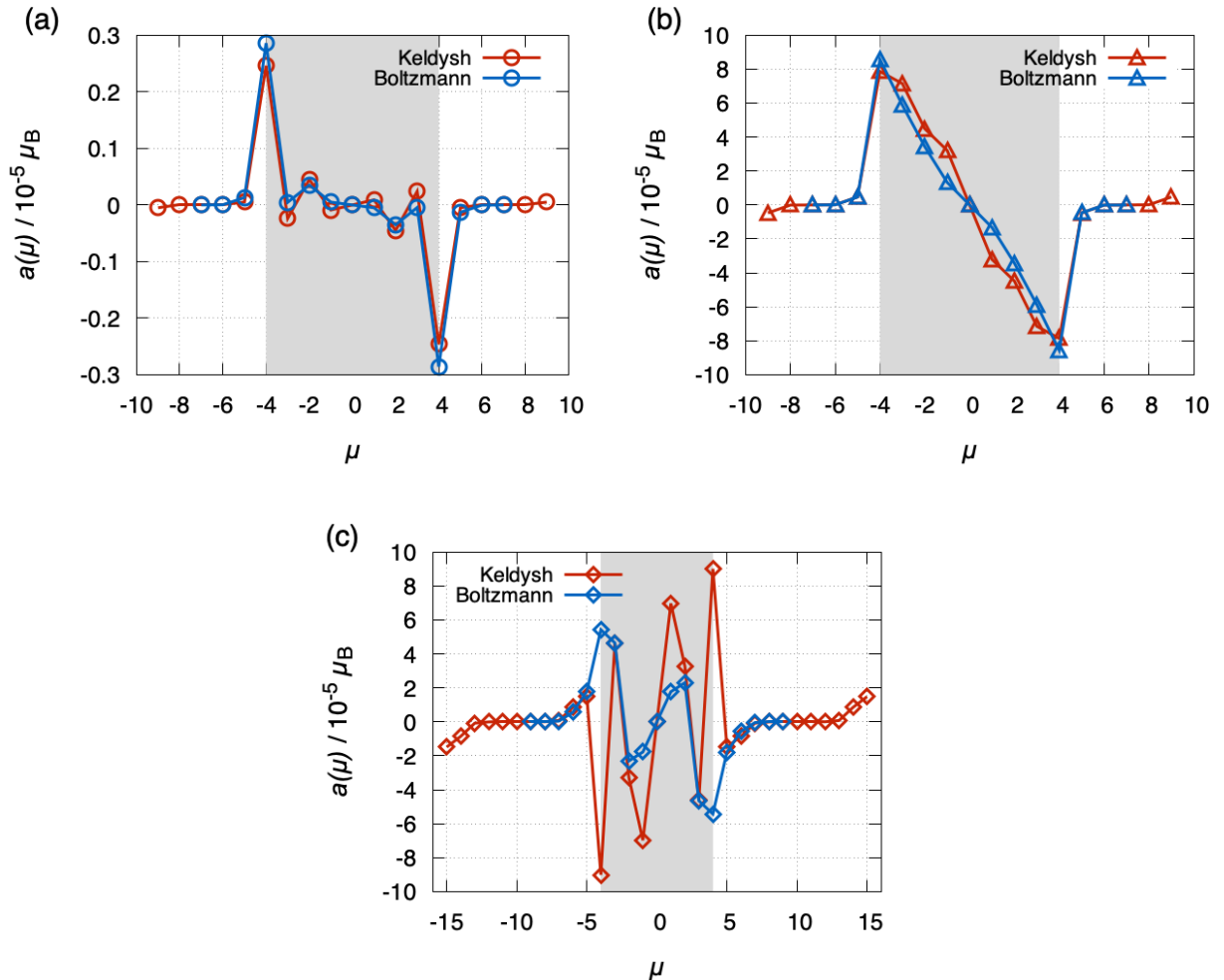


Figure 3. Magnetization for a thin film of 9 (a) Cu, (b) Pt and (c) U atoms (highlighted in grey). The agreement is very good for Cu. U and Pt differ in absolute values. U also shows a more complex inner structure of the accumulation. While the extremal values of accumulation decrease for Cu and U, for Pt they increase. We attribute this to the strong influence of finite size effects.
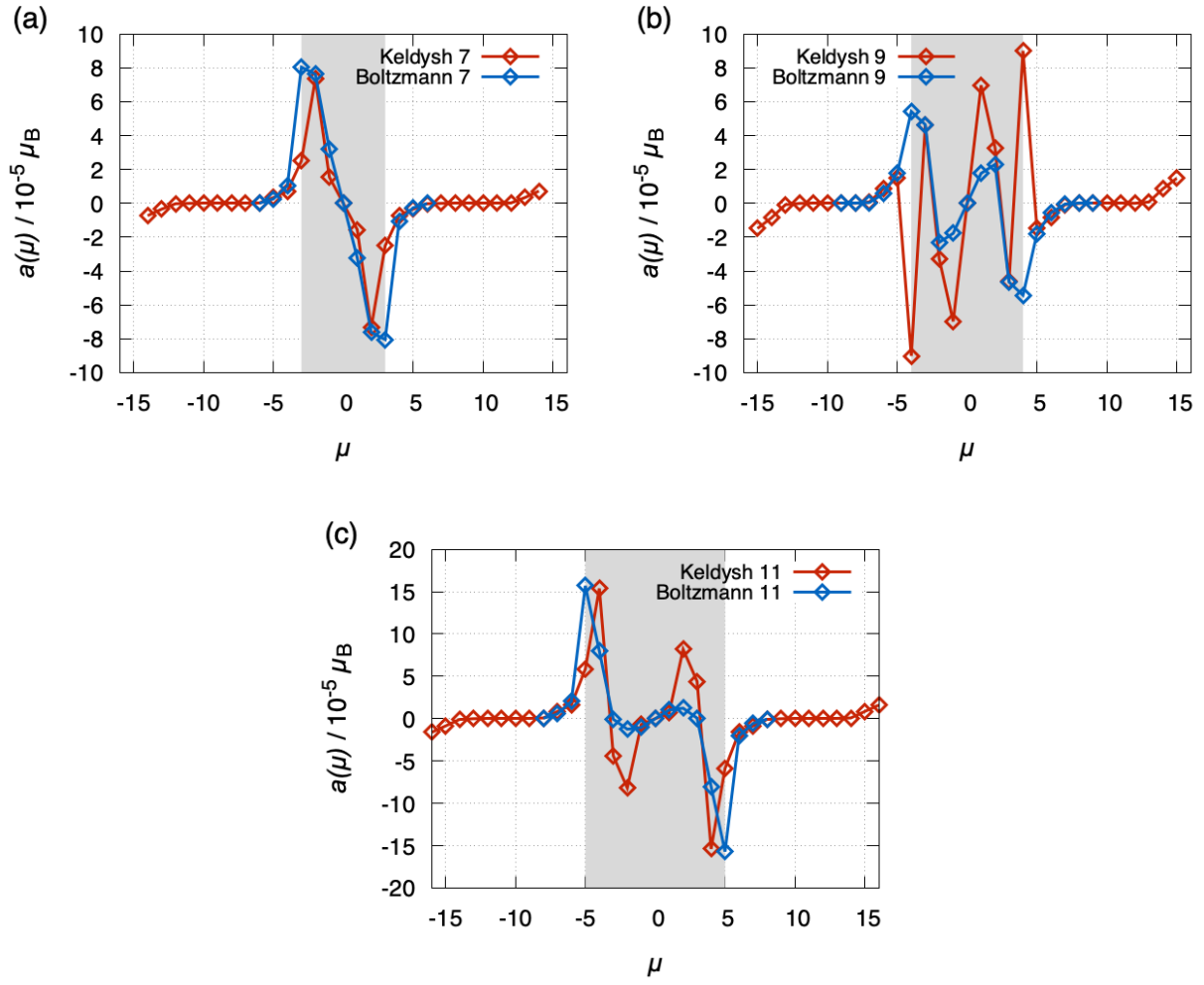
Figure 4. Magnetization for a thin film of (a) 7, (b) 9 and (c) 11 U atoms (highlighted in grey). While the sign change is evident for the system with 9 layers, it vanishes for the smaller and the larger systems. The position of the extremal value in (a) and (c) differs slightly between the two methods.

## III.   FERMI SURFACES

In Fig. 5 the group velocity is colour encoded on the Fermi surface. Cu, Ag, and Au show simple Fermi surfaces without too much variation of the group velocity. Ta, Pd, Pt, and U show a more complex structure with a more elaborated variation of the group velocity on the surface. For the entire discussion of the influences on the accumulation refer to the main text.
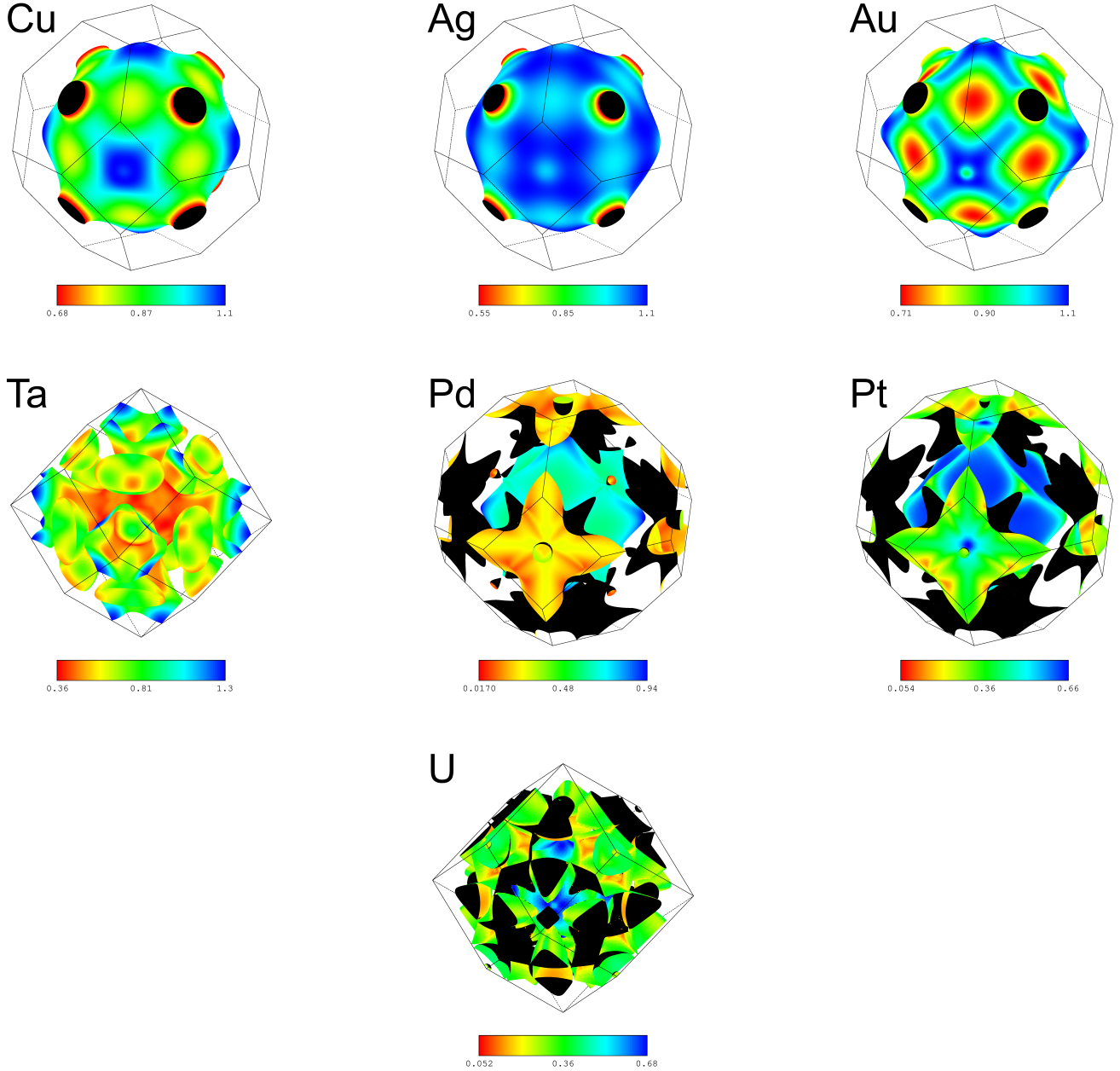


Figure 5. Fermi surfaces of the all the different systems (Cu, Ag, Au, Ta, Pd, Pt, U). The color code depicts the group velocity on the Fermi surface.

# C. Magneto Capacitance

The idea of the magneto capacitance is a magnetization orientation-dependent capacitance like the magnetoresistance [114] or the magneto Seebeck effect [115]. The capacity of a tunneling structure can be evaluated based on the findings in [13], that is, viewing the tunneling barrier as a classical plate capacitor for which

$$C = \frac{\Delta Q}{\Delta U} \tag{C.1}$$

holds. Here, $\Delta Q$ is the excess charge that is obtained by calculating the equilibrium density and the non-equilibrium density in the whole energy interval, adding the core electrons and the valence electrons in the energy interval $[E_B, \mu_>]$ as $\Delta Q = Q_{\text{NEQ}} - Q_{\text{EQ}}$. $Q_i$ are the charges in one half-space of the symmetric tunneling barrier with $Q_i = \sum_j \int_{V_j} \rho(\mathbf{r}) d\mathbf{r}$ and $V_i$ the volume of atomic spheres, that is contained in one half-space. The applied bias voltage is $e\Delta U = \mu_> - \mu_<$.

Expanding upon [13], introducing a magnetization, two cases are considered via the non-collinear magnetism formalism already implemented in the KKR code: parallel (p) and anti-parallel (ap) configuration. In the parallel configuration, the quantization axis of the magnetization is oriented parallel in both half-spaces. In the anti-parallel configuration, the quantization axis of the magnetization of the opposing half-space is oriented 180° to the first half-space. This allows for the definition of the two capacitances

$$C_{\text{p|ap}} = e\frac{\sum_j \int_{V_j} \left( \rho_{\text{NEQ}}^{\uparrow\uparrow|\uparrow\downarrow}(\mathbf{r}) - \rho_{\text{EQ}}^{\uparrow\uparrow|\uparrow\downarrow}(\mathbf{r}) \right) d\mathbf{r}}{\mu_> - \mu_<} \tag{C.2}$$

and likewise the definition of the magneto capacitance ratio in analogy [115, 116]

$$N_{MC} = \frac{C_{\text{ap}} - C_{\text{p}}}{f(C_{\text{ap}}, C_{\text{p}})} \tag{C.3}$$

with $f(\cdot, \cdot) := \max(\cdot, \cdot)$ or $\min(\cdot, \cdot)$.

For a symmetric Li tunneling barrier consisting of 44 Li and 12 Vac spheres , reasonable results for the capacitance could be obtained. In Fig. C.1, the integrated excess charge $\sum_j \int_{V_j} (\rho_{\text{NEQ}}(\mathbf{r}) - \rho_{\text{EQ}}(\mathbf{r})) d\mathbf{r}$ is shown for different applied bias voltages. The results are similar to [13], that is, the excess charge is mainly accumulating near the surface of the lithium. There are oscillations in the charge which are similar to Friedel oscillations, as expected from the interface structure. As expected, the additional potential barrier of the vacuum causes the electrons to reflect at the boundary. Note that the shape of the charge distribution is anti-symmetric, and a change in the sign of the bias voltage corresponds to a change in the sign of excess charge.

Looking at the charge in the left or right half-space in Fig. C.1 as the charge of a plate of a classical parallel plate capacitor, the obtained capacitance can be calculated via Eq. C.1. The capacitance per unit cell area is shown in Fig. C.2. The value for a bias of
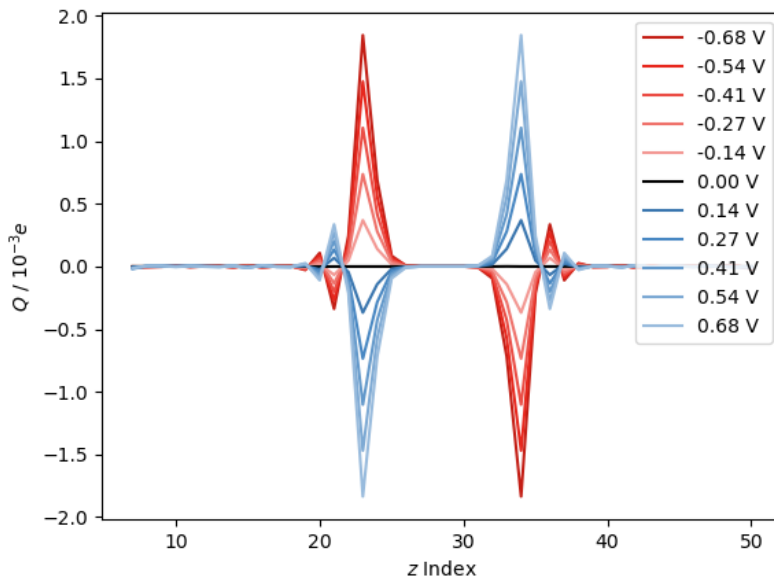
Figure C.1.: Excess Charge of a Lithium-Vac tunneling barrier for different values of applied bias voltage

$eU = 10^{-6}$ Ry has been left out, as Eq. C.1 diverges for $U \to 0$. Note that the relative deviation of the capacitance is less than 1%. Therefore, the capacitance is practically constant. This result might seem to be expected at first, but given the microscopic nature of the Li tunneling barrier and the comparably crude simplification, the result is quite remarkable.

For a symmetric Fe tunneling barrier (46 Fe, 4 Fe), however, the convergence was very hard to achieve. When the calculation eventually converged with a relative error for the potential below $10^{-8}$, the charge distribution in the transport direction showed strong oscillations that make the result at least questionable. Also, the excess charge distribution in Fig. C.3 shows no mirror symmetry as the charge distribution of the Li tunneling barrier in Fig. C.1. For the excess charge of a Fe vacuum tunneling barrier, see Fig. C.3.

We tried to achieve better convergence behavior by using the full-potential approach, where complete space-filling is achieved by introducing polyhedra. This introduces non-spherical parts to the potential, which are described by the expansion coefficients for the expansion after spherical harmonics. The higher $L$ components, especially the $p_z$ components, should facilitate the convergence of the potential with applied linear bias voltage because of their extension in the $z$ direction. It was found that the convergence behavior was not enhanced, but rather convergence could not be achieved. Presumably, this is due to the enhanced complexity of the method, which involves multiple higher $L$ components to converge in the already demanding NEQ scheme.
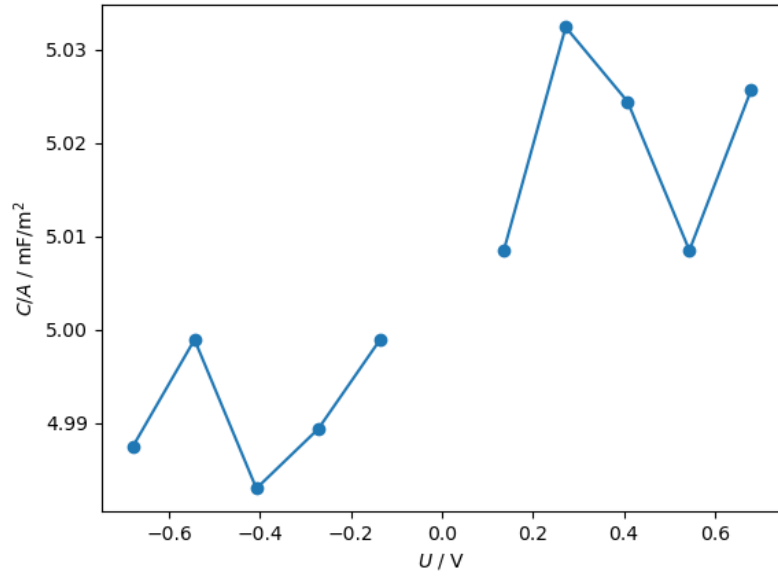
Figure C.2.: Capacitance per area vs. voltage for the Li tunneling barrier. The relative change of the capacitance is less than 1%, making the capacitance practically a constant as expected
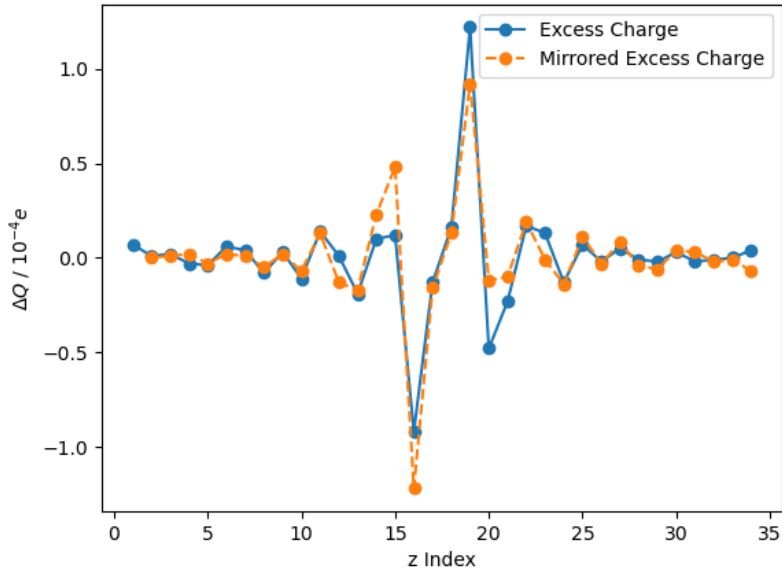


Figure C.3.: Excess charge of a Fe Vac tunneling barrier. The excess charge shows strong oscillations and a non-symmetric behavior. Moreover, the criterion for convergence during self-consistency was hard to achieve.

# D. Self-Consistent Spin Hall Calculations

The spin Hall calculations are done over the whole energy contour with an applied bias voltage to consider magnetization contributions from the Fermi surface and the Fermi sea. During the self-consistent cycle, the potential shifts and, therefore, magnetization contributions from the Fermi sea arise.

Here we want to consider two cases:

1. One-shot calculation

2. Self-consistent calculation

    a) without applied bias shift
    b) with applied bias shift

If not mentioned otherwise, the energy window (bias window) for the Fermi surface part (NEQ part) is $\mu_> - \mu_< = e\Delta\varphi = 10^{-4}$ Ry. States originating from the left side, that is, $n_L$, have to be calculated. The term "bias shift" means the actual shifting of the potential. On the left side, the potential gets shifted up by $e\Delta\varphi/2$, and likewise, on the right, shifted down by $-e\Delta\varphi/2$. In between, the potential is modeled as a linear potential drop.

## D.1. One-Shot Calculation

The magnetization for a one-step calculation without applied bias voltage shift is shown in Fig. D.1(a) for the EQ part and (b) for the NEQ part. We see that the resulting magnetization stems exclusively from the NEQ part as the fermi sea contribution vanishes. In Fig. D.2 the corresponding one-shot calculation at the Fermi Energy is shown. There is no difference visible between Fig. D.1(a) and Fig. D.2, again illustrating the fact that for the Fermi surface distribution at small bias voltages, only the value of the magnetization at the Fermi energy is relevant.

## D.2. Self-Consistent Calculation

Next, we consider the complete self-consistent cycle, which is shown in Fig. D.3. The magnetization is calculated from the full contour without a bias shift of the potential. The resulting magnetization profile dramatically changes along with the $z$ index, and the anti-symmetry in the $y$ direction completely breaks.

The first $z$ layer ($\eta = 1$) shows a tendency of anti-symmetry, but also, here, the anti-symmetry is not given ideally, as it was the case in the one-shot calculations. The contributions from the Fermi sea and the Fermi surface are shown in Fig. D.4(a) and (b), respectively. Splitting the contributions, we see that the Fermi sea contributes with negative values, which exhibit no anti-symmetry at all but rather a symmetry around
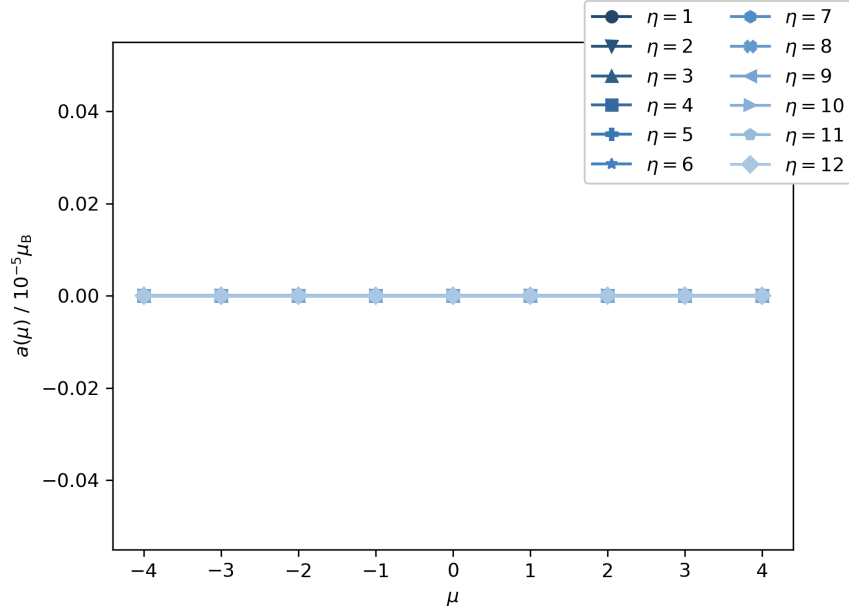
(a) Fermi sea contribution
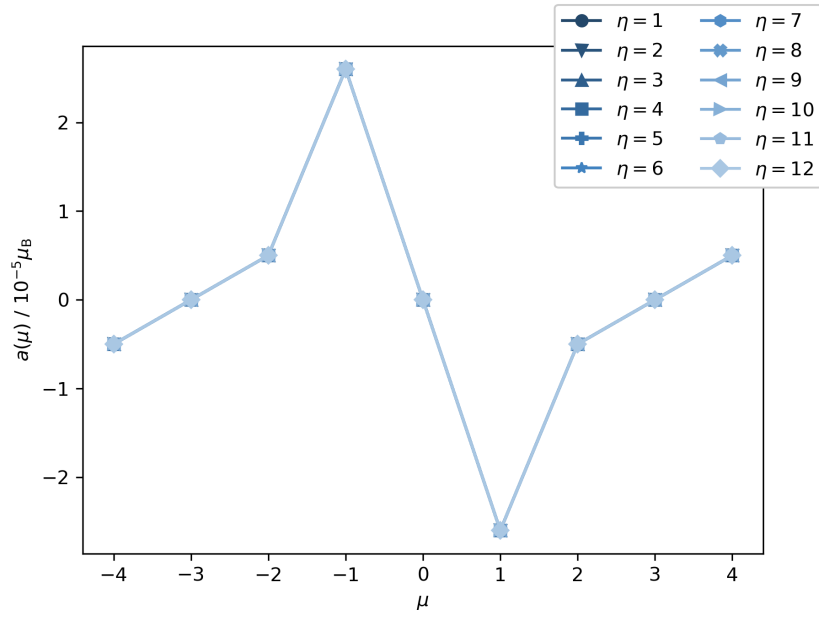


(b) Fermi surface contribution

Figure D.1.: Contributions of the magnetization of a Pt system (3Pt-3Vac) along the complete contour in a one-shot calculation.
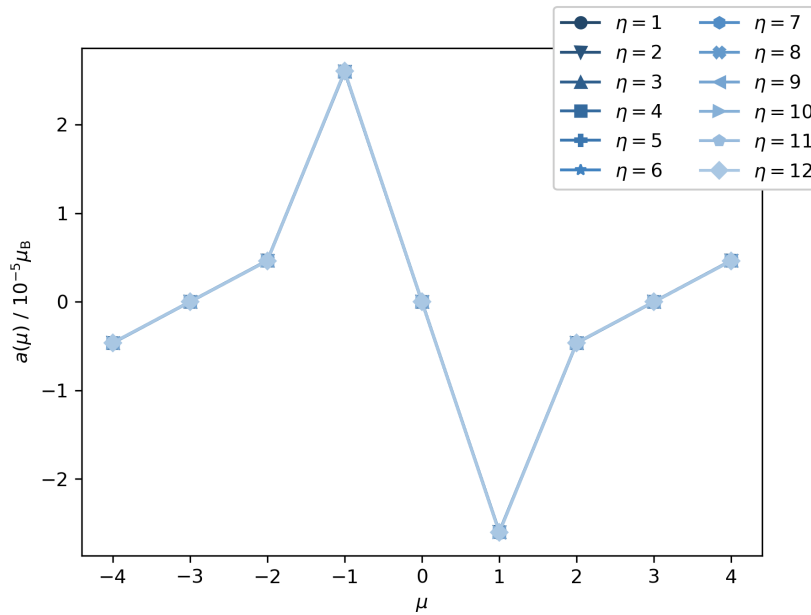
Figure D.2.: Magnetization of a Pt system (3Pt-3Vac) at the Fermi energy in a one-shot calculation. This result is obtained in analogy to Phys. Rev. B **104**, 054402, (2021).

$\mu = 0$. The Fermi surface contribution exhibits a tendency for anti-symmetry, which is visible for the $z$ layers $\eta = 2$ and $\eta = 11$. This tendency for symmetry and anti-symmetry for both parts, respectively, is at least in good agreement with the behavior of the torque in Ref. [15].

We continue with the self-consistent calculation with an applied bias shift. The result from the complete contour is shown in Fig. D.5 and the contributions from the Fermi sea and the Fermi surface in Fig. D.6(a) and (b), respectively. In this calculation, the potential has been shifted by the according linearly interpolated bias shift and then calculated self consistently. We see here a similar behavior to the calculation without an explicitly applied bias voltage. The total magnetization shows both symmetric and anti-symmetric behavior. The Fermi sea contribution is almost always negative with the tendency to symmetric behavior. The Fermi surface contribution shows an anti-symmetric-like behavior for $\eta = 2$ and $\eta = 11$.

In both versions of the calculations, the Fermi sea contribution dominates.

We now explicitly take the even-under-spatial-inversion magnetization contributions into account by integrating over the full contour. The calculations are then done self-consistently until the potential has sufficiently converged. During this self-consistent cycle, the Fermi energy is pinned in the left and right leads, and the potential shifts relative to the pinned Fermi energies. Due to this potential shift during the self-consistent cycle, it is not *a priori* clear if obtained contributions now only stem from the Fermi sea or if they get mixed, resulting in a superposition of both contributions. From the point of view of the KKR one-shot calculations, the distinction between Fermi sea and surface term in analogy to Boltzmann and Kubo calculations makes sense, as the latter also derive from a pre-converged potential. The fully self-consistent calculations in the
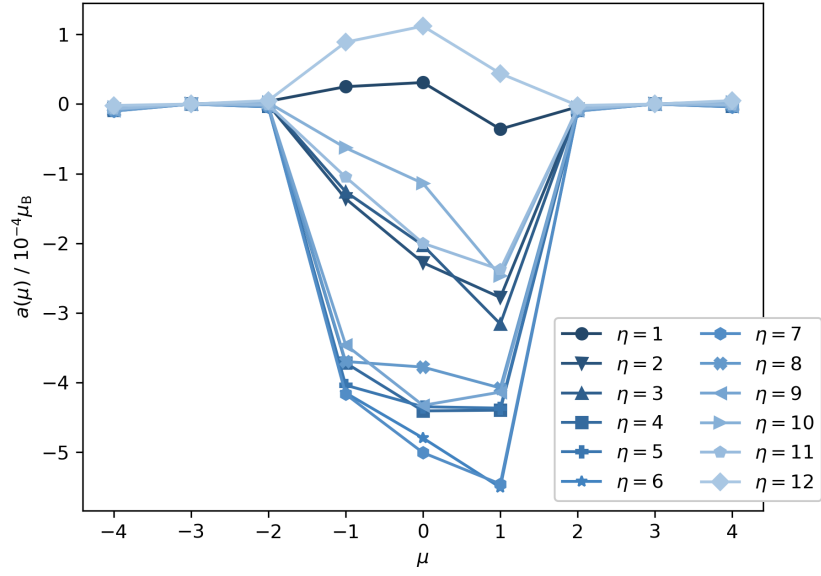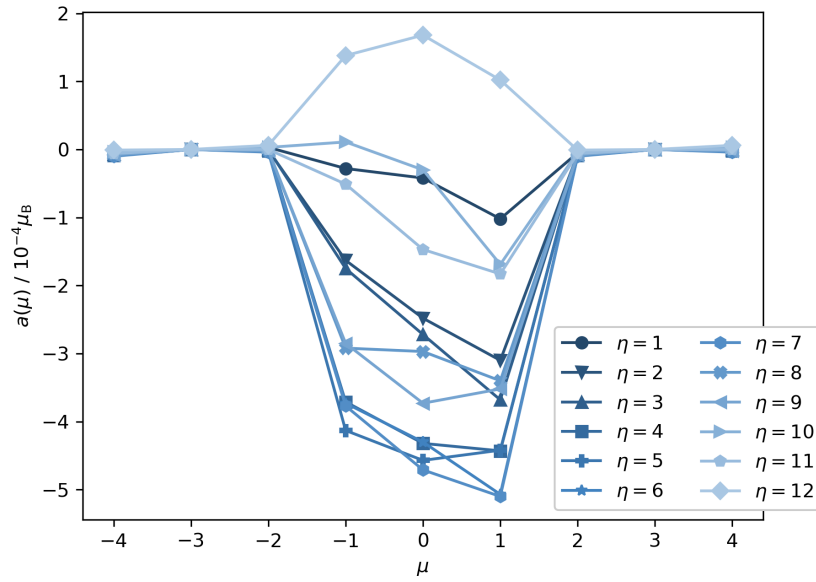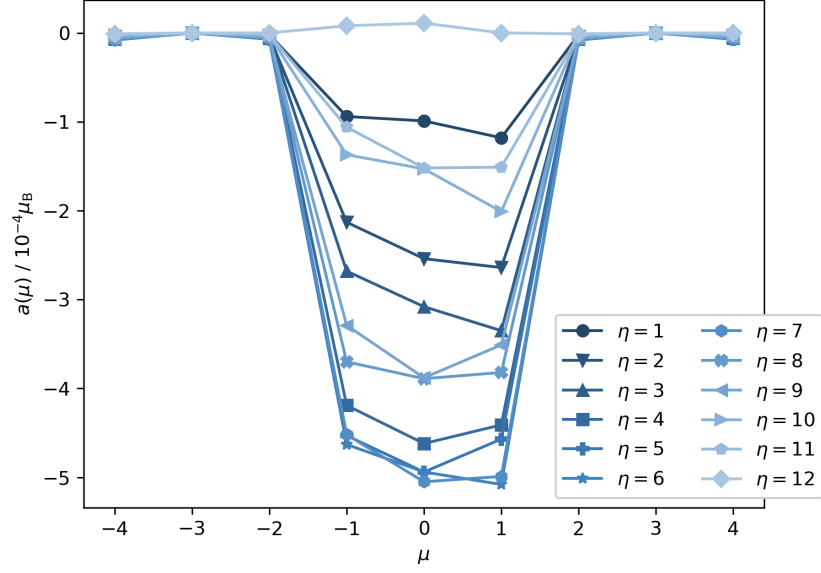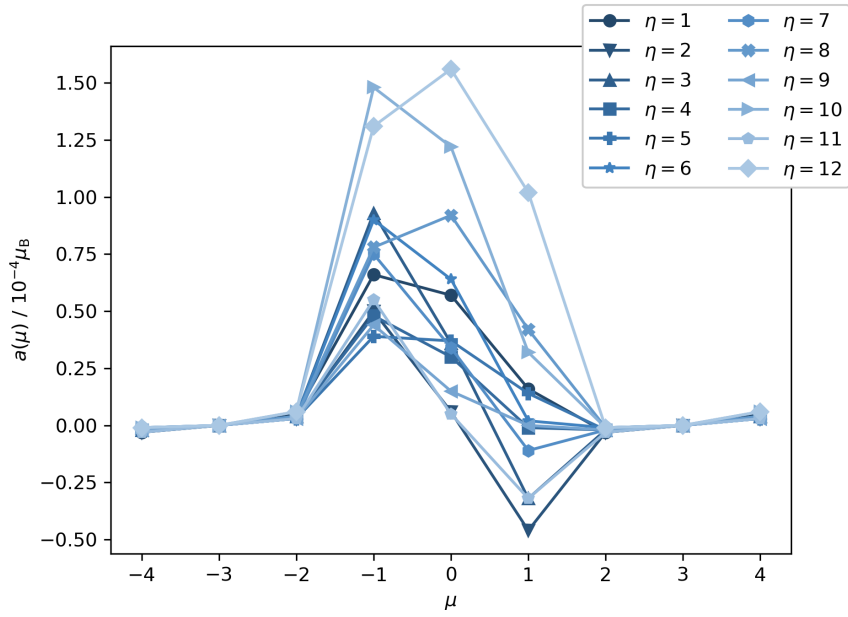
Figure D.3.: Magnetization of a Pt system (3Pt-3Vac) along the complete contour after a full self-consistent cycle without bias-shifted potentials.

KKR, however, make it at least questionable to attribute certain features to either sea or surface contribution or distinguish between them.
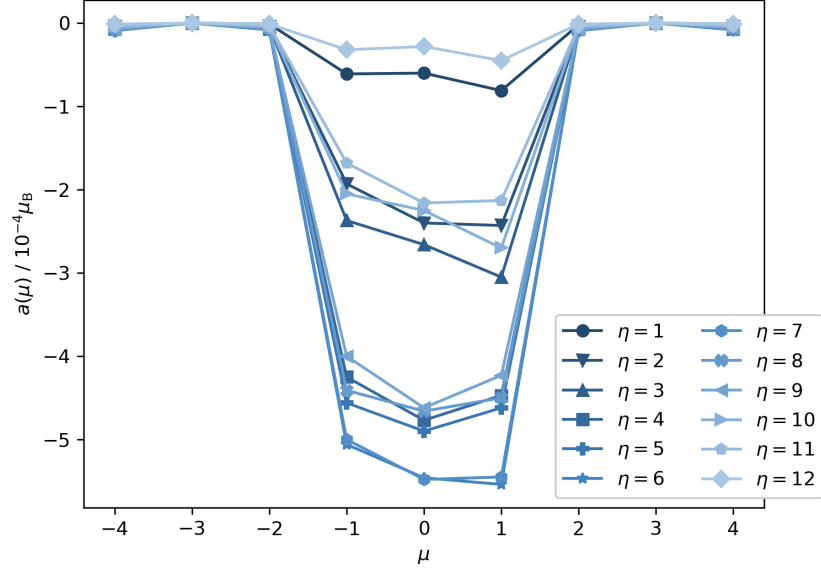
(a) Fermi sea contribution
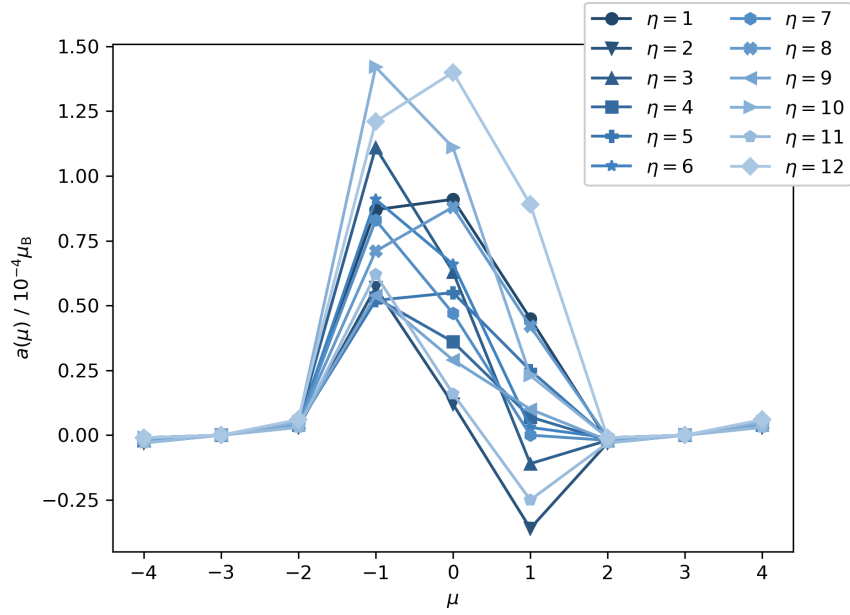


(b) Fermi surface contribution

Figure D.4.: Contributions of the magnetization of a Pt system (3Pt-3Vac) along the complete contour after a full self-consistent cycle without bias-shifted potentials.

Figure D.5.: Magnetization of a Pt system (3Pt-3Vac) along the complete contour after a full self-consistent cycle with bias-shifted potentials.

(a) Fermi sea contribution



(b) Fermi surface contribution

Figure D.6.: Contributions of the magnetization of a Pt system (3Pt-3Vac) along the complete contour after a full self-consistent cycle with bias-shifted potentials.

87

# E. Kerker Preconditioner

The Kerker preconditioner is mainly based on the work of Kerker [117]. Spurious charges originating from the starting potential can occur during the mixing process of the potential since the starting potential is only an educated guess for the final self-consistent potential [117]. These charges contribute to the potential in the next step in the self-consistent cycle and can therefore cause instabilities in the convergence process [117]. This is especially the case for large supercells. Kerker's main idea is to introduce a screening term in the Poisson equation [117, 118]

$$\left(\nabla^2 - \lambda^2\right) V_{\text{Coul}}(\mathbf{r}) = -4\pi e^2 \left(\rho(\mathbf{r}) + \frac{\lambda^2}{4\pi e^2} V_{\text{Coul}}(\mathbf{r})\right) \tag{E.1}$$

that leads to exponentially decaying long-range contributions. The factor $\lambda$ can be seen as a screening parameter.

Since in KKR the implementation of the Coulomb contributions to the potential is implemented by an Ewald method, the far field contributions are treated via Fourier transformation. During the evaluation of the necessary coefficients [105], an integral of the form

$$\int_0^\infty e^{-r^2 x^2} e^{-\lambda r} j_\ell(Gr) r^{2+k} \mathrm{d}r \tag{E.2}$$

arises. No obvious analytic solution could be found. However, evaluation might be possible with numerical methods. It remains the question of whether far-field contributions have to be considered at all when they decay exponentially anyway. An edge case for testing this ansatz is a vanishing screening parameter $\lambda$. To test the old and new implementations against each other, however, for vanishing $\lambda$, the far-field contributions have to be considered explicitly in the Kerker approach. Unfortunately, this task remains open.

# Bibliography

[1]  G. E. Moore, "Cramming more components onto integrated circuits", Electronics **38**, 114–117 (1965).

[2]  S. A. Wolf, D. D. Awschalom, R. A. Buhrman, J. M. Daughton, S. von Molnár, M. L. Roukes, A. Y. Chtchelkanova, and D. M. Treger, "Spintronics: A Spin-Based Electronics Vision for the Future", Science **294**, 1488–1495 (2001) DOI: 10.1126/science.1065389.

[3]  R. Kubo, "Statistical-Mechanical Theory of Irreversible Processes. I. General Theory and Simple Applications to Magnetic and Conduction Problems", J. Phys. Soc. Jpn. **12**, 570–586 (1957) DOI: 10.1143/JPSJ.12.570.

[4]  T. Low, A. S. Rodin, A. Carvalho, Y. Jiang, H. Wang, F. Xia, and A. H. Castro Neto, "Tunable optical properties of multilayer black phosphorus thin films", Phys. Rev. B **90**, 075434 (2014) DOI: 10.1103/PhysRevB.90.075434.

[5]  S. Lowitzer, M. Gradhand, D. Ködderitzsch, D. V. Fedorov, I. Mertig, and H. Ebert, "Extrinsic and Intrinsic Contributions to the Spin Hall Effect of Alloys", Phys. Rev. Lett. **106**, 056601 (2011) DOI: 10.1103/PhysRevLett.106.056601.

[6]  G. Y. Guo, Y. Yao, and Q. Niu, "Ab initio Calculation of the Intrinsic Spin Hall Effect in Semiconductors", Phys. Rev. Lett. **94**, 226601 (2005) DOI: 10.1103/PhysRevLett.94.226601.

[7]  Y. Yao and Z. Fang, "Sign Changes of Intrinsic Spin Hall Effect in Semiconductors and Simple Metals: First-Principles Calculations", Phys. Rev. Lett. **95**, 156601 (2005) DOI: 10.1103/PhysRevLett.95.156601.

[8]  I. Mertig, "Transport properties of dilute alloys", Rep. Prog. Phys. **62**, 237–276 (1999) DOI: 10.1088/0034-4885/62/2/004.

[9]  W. Li, "Electrical transport limited by electron-phonon coupling from Boltzmann transport equation: An *ab initio* study of Si, Al, and $MoS_2$", Phys. Rev. B **92**, 075405 (2015) DOI: 10.1103/PhysRevB.92.075405.

[10]  J. M. Ziman, *Principles of the Theory of Solids*, Second Edition (Cambridge University Press, 1972), DOI: 10.1017/CBO9781139644075.

[11]  C. Herschbach, M. Gradhand, D. V. Fedorov, and I. Mertig, "Enhancement of the spin Hall angle by quantum confinement", Phys. Rev. B **85**, 195133 (2012) DOI: 10.1103/PhysRevB.85.195133.

[12]  G. Géranton, B. Zimmermann, N. H. Long, P. Mavropoulos, S. Blügel, F. Freimuth, and Y. Mokrousov, "Spin-orbit torques and spin accumulation in FePt/Pt and Co/Cu thin films from first principles: The role of impurities", Phys. Rev. B **93**, 224420 (2016) DOI: 10.1103/PhysRevB.93.224420.

[13] S. Achilles, M. Czerner, J. Henk, I. Mertig, and C. Heiliger, "Nonequilibrium Green's functions and Korringa-Kohn-Rostoker method: Open planar junctions", Phys. Rev. B **88**, DOI: 10.1103/PhysRevB.88.125411 (2013) DOI: 10.1103/PhysRevB.88.125411.

[14] F. Freimuth, S. Blügel, and Y. Mokrousov, "Spin-orbit torques in Co/Pt(111) and Mn/W(001) magnetic bilayers from first principles", Phys. Rev. B **90**, 174423 (2014) DOI: 10.1103/PhysRevB.90.174423.

[15] S. Wimmer, K. Chadova, M. Seemann, D. Ködderitzsch, and H. Ebert, "Fully relativistic description of spin-orbit torques by means of linear response theory", Phys. Rev. B **94**, 054415 (2016) DOI: 10.1103/PhysRevB.94.054415.

[16] A. Fabian, M. Czerner, C. Heiliger, H. Rossignol, M.-H. Wu, and M. Gradhand, "Spin accumulation from nonequilibrium first principles methods", Phys. Rev. B **104**, 054402 (2021) DOI: 10.1103/PhysRevB.104.054402.

[17] C. E. Mahr, M. Czerner, and C. Heiliger, "Implementation of a method for calculating temperature-dependent resistivities in the KKR formalism", Phys. Rev. B **96**, 165121 (2017) DOI: 10.1103/PhysRevB.96.165121.

[18] C. E. Mahr, "Ab initio description of transport in nanostructures including electron-phonon coupling", PhD thesis (Justus-Liebig-Universität Gießen, 2018).

[19] M. Büttiker, "Small normal-metal loop coupled to an electron reservoir", Phys. Rev. B **32**, 1846–1849 (1985) DOI: 10.1103/PhysRevB.32.1846.

[20] A. Fabian, M. Gradhand, M. Czerner, and C. Heiliger, "First-principles scattering with Büttiker probes: The role of self-energies", Phys. Rev. B **105**, 165106 (2022) DOI: 10.1103/PhysRevB.105.165106.

[21] J. Henk, A. Ernst, K. K. Saha, and P. Bruno, "Computing conductances of tunnel junctions by the Korringa–Kohn–Rostoker method: formulation and test of a Green function approach", J. Phys. Condens. Matter **18**, 2601–2614 (2006) DOI: 10.1088/0953-8984/18/8/021.

[22] C. Heiliger, M. Czerner, B. Y. Yavorsky, I. Mertig, and M. D. Stiles, "Implementation of a nonequilibrium Green's function method to calculate spin-transfer torque", J. Appl. Phys. **103**, 07A709 (2008) DOI: 10.1063/1.2835071.

[23] C. Franz, M. Czerner, and C. Heiliger, "Implementation of non-equilibrium vertex corrections in KKR: transport through disordered layers", J. Phys. Condens. Matter **25**, 425301 (2013) DOI: 10.1088/0953-8984/25/42/425301.

[24] S. Datta, *Electronic Transport in Mesoscopic Systems* (Cambridge University Press, 1995), DOI: 10.1017/CBO9780511805776.

[25] K. Wildberger, "Tight-Binding-Korringa-Kohn-Rostoker-Methode und Grenzflächenreflektivität in magnetischen Schichtsystemen", PhD thesis (Forschungszentrum Jülich, 1997).

[26] M. Fechner, "Theoretische Untersuchung der Dispersionsrelation von Feldemissionszuständen", PhD thesis (Martin-Luther-Universität Halle, 2006).

[27] M. P. Lopez Sancho, J. M. Lopez Sancho, J. M. L. Sancho, and J. Rubio, "Highly convergent schemes for the calculation of bulk and surface Green functions", J. Phys. F: Met. Phys. **15**, 851–858 (1985) DOI: 10.1088/0305-4608/15/4/009.

[28]  M. Pourfath, *The Non-Equilibrium Green's Function Method for Nanoscale Device Simulation*, Computational Microelectronics (Springer, Vienna, 2014), DOI: 10.1007/978-3-7091-1800-9.

[29]  R. Zeller, J. Deutz, and P. H. Dederichs, "Application of complex energy integration to selfconsistent electronic structure calculations", Solid State Commun. **44**, 993–997 (1982) DOI: 10.1016/0038-1098(82)90320-9.

[30]  K. Wildberger, P. Lang, R. Zeller, and P. H. Dederichs, "Fermi-Dirac distribution in *ab initio* Green's-function calculations", Phys. Rev. B **52**, 11502–11508 (1995) DOI: 10.1103/PhysRevB.52.11502.

[31]  M. Brandbyge, J.-L. Mozos, P. Ordejón, J. Taylor, and K. Stokbro, "Density-functional method for nonequilibrium electron transport", Phys. Rev. B **65**, DOI: 10.1103/PhysRevB.65.165401 (2002) DOI: 10.1103/PhysRevB.65.165401.

[32]  D. Ryndyk, *Theory of Quantum Transport at Nanoscale*, Vol. 184, Springer Series in Solid-State Sciences (Springer, Cham, 2016), DOI: 10.1007/978-3-319-24088-6.

[33]  G. Metalidis, "Electronic Transport in Mesoscopic Systems", PhD thesis (Martin-Luther-Universität Halle-Wittenberg, 2007).

[34]  M. Czerner and C. Heiliger, "Influence of interface termination on the magneto-Seebeck effect in MgO based tunnel junctions", J. Appl. Phys. **111**, 07C511 (2012) DOI: 10.1063/1.3675987.

[35]  Y. Ouyang and J. Guo, "A theoretical study on thermoelectric properties of graphene nanoribbons", Appl. Phys. Lett. **94**, 263107 (2009) DOI: 10.1063/1.3171933.

[36]  M. Czerner, Private Communication (2021).

[37]  G. Czycholl, *Theoretische Festkörperphysik. Band 2: Anwendungen: Nichtgleichgewicht, Verhalten in äußeren Feldern, kollektive Phänomene*, Fourth Edition (Springer Spektrum, Berlin, 2017).

[38]  M. Gradhand, D. V. Fedorov, P. Zahn, and I. Mertig, "Extrinsic Spin Hall Effect from First Principles", Phys. Rev. Lett. **104**, 186403 (2010) DOI: 10.1103/PhysRevLett.104.186403.

[39]  N. A. Sinitsyn, A. H. MacDonald, T. Jungwirth, V. K. Dugaev, and J. Sinova, "Anomalous Hall effect in a two-dimensional Dirac band: The link between the Kubo-Streda formula and the semiclassical Boltzmann equation approach", Phys. Rev. B **75**, 045315 (2007) DOI: 10.1103/PhysRevB.75.045315.

[40]  J. M. Luttinger and W. Kohn, "Quantum Theory of Electrical Transport Phenomena. II", Phys. Rev. **109**, 1892–1909 (1958) DOI: 10.1103/PhysRev.109.1892.

[41]  H. Usui, R. Arita, and K. Kuroki, "First-principles study on the origin of large thermopower in hole-doped $LaRhO_3$ and $CuRhO_2$", J. Phys.: Condens. Matter **21**, 064223 (2009) DOI: 10.1088/0953-8984/21/6/064223.

[42]  E. H. Hall, "On a New Action of the Magnet on Electric Currents", Am. J. Math. **2**, 287–292 (1879).

[43]  K. von Klitzing, "The quantized Hall effect", Rev. Mod. Phys. **58**, 519–531 (1986) DOI: 10.1103/RevModPhys.58.519.

[44]  J. E. Hirsch, "Spin Hall Effect", Phys. Rev. B **83**, 1834 (1999) DOI: 10.1103/PhysRevLett.83.1834.

[45] C. L. Kane and E. J. Mele, "Quantum Spin Hall Effect in Graphene", Phys. Rev. Lett. **95**, 226801 (2005) DOI: 10.1103/PhysRevLett.95.226801.

[46] N. Nagaosa, J. Sinova, S. Onoda, A. H. MacDonald, and N. P. Ong, "Anomalous Hall effect", Reviews of Modern Physics **82**, 1539–1592 (2010) DOI: 10.1103/RevModPhys.82.1539.

[47] S. Fukami, T. Anekawa, C. Zhang, and H. Ohno, "A spin–orbit torque switching scheme with collinear magnetic easy axis and current configuration", Nature Nanotech **11**, 621–625 (2016) DOI: 10.1038/nnano.2016.29.

[48] Y. V. Pershin, N. A. Sinitsyn, A. Kogan, A. Saxena, and D. L. Smith, "Spin polarization control by electric stirring: Proposal for a spintronic device", Appl. Phys. Lett. **95**, 022114 (2009) DOI: 10.1063/1.3180494.

[49] A. Hoffmann, "Spin Hall Effects in Metals", IEEE Trans. Magn. **49**, 5172–5193 (2013) DOI: 10.1109/TMAG.2013.2262947.

[50] L. Liu, C.-F. Pai, Y. Li, H. W. Tseng, D. C. Ralph, and R. A. Buhrman, "Spin-Torque Switching with the Giant Spin Hall Effect of Tantalum", Science **336**, 555–558 (2012) DOI: 10.1126/science.1218197.

[51] Y. Kajiwara, K. Harii, S. Takahashi, J. Ohe, K. Uchida, M. Mizuguchi, H. Umezawa, H. Kawai, K. Ando, K. Takanashi, S. Maekawa, and E. Saitoh, "Transmission of electrical signals by spin-wave interconversion in a magnetic insulator", Nature **464**, 262–266 (2010) DOI: 10.1038/nature08876.

[52] H. Nakayama, M. Althammer, Y.-T. Chen, K. Uchida, Y. Kajiwara, D. Kikuchi, T. Ohtani, S. Geprägs, M. Opel, S. Takahashi, R. Gross, G. E. W. Bauer, S. T. B. Goennenwein, and E. Saitoh, "Spin Hall Magnetoresistance Induced by a Nonequilibrium Proximity Effect", Phys. Rev. Lett. **110**, 206601 (2013) DOI: 10.1103/PhysRevLett.110.206601.

[53] H. Wu, X. Zhang, C. H. Wan, B. S. Tao, L. Huang, W. J. Kong, and X. F. Han, "Hanle magnetoresistance: The role of edge spin accumulation and interfacial spin current", Phys. Rev. B **94**, 174407 (2016) DOI: 10.1103/PhysRevB.94.174407.

[54] K. Ando, S. Takahashi, K. Harii, K. Sasage, J. Ieda, S. Maekawa, and E. Saitoh, "Electric Manipulation of Spin Relaxation Using the Spin Hall Effect", Phys. Rev. Lett. **101**, 036601 (2008) DOI: 10.1103/PhysRevLett.101.036601.

[55] Y. K. Kato, R. C. Myers, A. C. Gossard, and D. D. Awschalom, "Observation of the Spin Hall Effect in Semiconductors", Science **306**, 1910–1913 (2004) DOI: 10.1126/science.1105514.

[56] J. Wunderlich, B. Kaestner, J. Sinova, and T. Jungwirth, "Experimental Observation of the Spin-Hall Effect in a Two-Dimensional Spin-Orbit Coupled Semiconductor System", Phys. Rev. Lett. **94**, 047204 (2005) DOI: 10.1103/PhysRevLett.94.047204.

[57] M.-J. Jin, D.-S. Um, K. Ohnishi, S. Komori, N. Stelmashenko, D. Choe, J.-W. Yoo, and J. W. A. Robinson, "Pure Spin Currents Driven by Colossal Spin–Orbit Coupling on Two-Dimensional Surface Conducting $SrTiO_3$", Nano Lett. **21**, 6511–6517 (2021) DOI: 10.1021/acs.nanolett.1c01607.

[58] K. S. Das, W. Y. Schoemaker, B. J. van Wees, and I. J. Vera-Marun, "Spin injection and detection via the anomalous spin Hall effect of a ferromagnetic metal", Phys. Rev. B **96**, 220408 (2017) DOI: 10.1103/PhysRevB.96.220408.

[59] S. O. Valenzuela and M. Tinkham, "Direct electronic measurement of the spin Hall effect", Nature **442**, 176–179 (2006) DOI: 10.1038/nature04937.

[60] H. Zhao, E. J. Loren, H. M. van Driel, and A. L. Smirl, "Coherence Control of Hall Charge and Spin Currents", Phys. Rev. Lett. **96**, 246601 (2006) DOI: 10.1103/PhysRevLett.96.246601.

[61] E. Saitoh, M. Ueda, H. Miyajima, and G. Tatara, "Conversion of spin current into charge current at room temperature: Inverse spin-Hall effect", Appl. Phys. Lett. **88**, 182509 (2006) DOI: 10.1063/1.2199473.

[62] Z. Diao, Z. Li, S. Wang, Y. Ding, A. Panchula, E. Chen, L.-C. Wang, and Y. Huai, "Spin-transfer torque switching in magnetic tunnel junctions and spin-transfer torque random access memory", J. Phys.: Condens. Matter **19**, 165209 (2007) DOI: 10.1088/0953-8984/19/16/165209.

[63] L. Zhu, D. C. Ralph, and R. A. Buhrman, "Maximizing spin-orbit torque generated by the spin Hall effect of Pt", Appl. Phys. Rev. **8**, 031308 (2021) DOI: 10.1063/5.0059171.

[64] D. Ködderitzsch, K. Chadova, and H. Ebert, "Linear response Kubo-Bastin formalism with application to the anomalous and spin Hall effects: A first-principles approach", Phys. Rev. B **92**, 184415 (2015) DOI: 10.1103/PhysRevB.92.184415.

[65] A. Kosma, P. Rüßmann, S. Blügel, and P. Mavropoulos, "Strong spin-orbit torque effect on magnetic defects due to topological surface state electrons in $Bi_2Te_3$", Phys. Rev. B **102**, 144424 (2020) DOI: 10.1103/PhysRevB.102.144424.

[66] J. Sinova, D. Culcer, Q. Niu, N. A. Sinitsyn, T. Jungwirth, and A. H. MacDonald, "Universal Intrinsic Spin Hall Effect", Phys. Rev. Lett. **92**, 126603 (2004) DOI: 10.1103/PhysRevLett.92.126603.

[67] G. Y. Guo, S. Murakami, T.-W. Chen, and N. Nagaosa, "Intrinsic Spin Hall Effect in Platinum: First-Principles Calculations", Phys. Rev. Lett. **100**, 096401 (2008) DOI: 10.1103/PhysRevLett.100.096401.

[68] S. Murakami, "Dissipationless Quantum Spin Current at Room Temperature", Science **301**, 1348–1351 (2003) DOI: 10.1126/science.1087128.

[69] J. Sinova, S. O. Valenzuela, J. Wunderlich, C. H. Back, and T. Jungwirth, "Spin Hall effects", Rev. Mod. Phys. **87**, 1213–1260 (2015) DOI: 10.1103/RevModPhys.87.1213.

[70] J. Smit, "The spontaneous hall effect in ferromagnetics I", Physica **21**, 877–887 (1955) DOI: 10.1016/S0031-8914(55)92596-9.

[71] J. Smit, "The spontaneous hall effect in ferromagnetics II", Physica **24**, 39–51 (1958) DOI: 10.1016/S0031-8914(58)93541-9.

[72] L. Berger, "Side-Jump Mechanism for the Hall Effect of Ferromagnets", Phys. Rev. B **2**, 4559–4566 (1970) DOI: 10.1103/PhysRevB.2.4559.

[73] R. Karplus and J. M. Luttinger, "Hall Effect in Ferromagnetics", Phys. Rev. **95**, 1154–1160 (1954) DOI: 10.1103/PhysRev.95.1154.

[74] T. Jungwirth, Q. Niu, and A. H. MacDonald, "Anomalous Hall Effect in Ferromagnetic Semiconductors", Phys. Rev. Lett. **88**, 207208 (2002) DOI: 10.1103/PhysRevLett.88.207208.

[75] J. C. Swihart, W. H. Butler, G. M. Stocks, D. M. Nicholson, and R. C. Ward, "First-Principles Calculation of the Residual Electrical Resistivity of Random Alloys", Phys. Rev. Lett. **57**, 1181–1184 (1986) DOI: 10.1103/PhysRevLett.57.1181.

[76] P. Zahn, J. Binder, and I. Mertig, "Impurity scattering and quantum confinement in giant magnetoresistive systems", Phys. Rev. B **68**, 100403 (2003) DOI: 10.1103/PhysRevB.68.100403.

[77] G. Y. Guo, "Ab initio calculation of intrinsic spin Hall conductivity of Pd and Au", J. Appl. Phys. **105**, 07C701 (2009) DOI: 10.1063/1.3054362.

[78] X. Wang, J. R. Yates, I. Souza, and D. Vanderbilt, "*AB INITIO* calculation of the anomalous Hall conductivity by Wannier interpolation", Phys. Rev. B **74**, 195118 (2006) DOI: 10.1103/PhysRevB.74.195118.

[79] Y. Yao, L. Kleinman, A. H. MacDonald, J. Sinova, T. Jungwirth, D.-s. Wang, E. Wang, and Q. Niu, "First Principles Calculation of Anomalous Hall Conductivity in Ferromagnetic bcc Fe", Phys. Rev. Lett. **92**, 037204 (2004) DOI: 10.1103/PhysRevLett.92.037204.

[80] B. K. Nikolić, L. P. Zârbo, and S. Souma, "Mesoscopic spin Hall effect in multiprobe ballistic spin-orbit-coupled semiconductor bridges", Phys. Rev. B **72**, 075361 (2005) DOI: 10.1103/PhysRevB.72.075361.

[81] B. K. Nikolić, L. P. Zârbo, and S. Welack, "Transverse spin-orbit force in the spin Hall effect in ballistic semiconductor wires", Phys. Rev. B **72**, 075335 (2005) DOI: 10.1103/PhysRevB.72.075335.

[82] B. K. Nikolic, L. P. Zarbo, and S. Souma, "Imaging mesoscopic spin Hall flow: Spatial distribution of local spin currents and spin densities in and out of multiterminal spin-orbit coupled semiconductor nanostructures", Phys. Rev. B **73**, 075303 (2006) DOI: 10.1103/PhysRevB.73.075303.

[83] B. K. Nikolić, S. Souma, L. P. Zârbo, and J. Sinova, "Nonequilibrium Spin Hall Accumulation in Ballistic Semiconductor Nanostructures", Phys. Rev. Lett. **95**, 046601 (2005) DOI: 10.1103/PhysRevLett.95.046601.

[84] M. Gradhand, "The Extrinsic Spin Hall Effect", PhD thesis (Martin-Luther-Universität Halle-Wittenberg, 2010).

[85] N. A. Sinitsyn, "Semiclassical theories of the anomalous Hall effect", J. Phys.: Condens. Matter **20**, 023201 (2008) DOI: 10.1088/0953-8984/20/02/023201.

[86] M. Gradhand, D. V. Fedorov, F. Pientka, P. Zahn, I. Mertig, and B. L. Györffy, "First-principle calculations of the Berry curvature of Bloch states for charge and spin transport of electrons", J. Phys. Condens. Matter **24**, 213202 (2012) DOI: 10.1088/0953-8984/24/21/213202.

[87] N. F. Mott, "The scattering of fast electrons by atomic nuclei", Proc. R. Soc. Lond. A **124**, 425–442 (1929) DOI: 10.1098/rspa.1929.0127.

[88] N. F. Mott, "The polarisation of electrons by double scattering", Proc. R. Soc. Lond. A **135**, 429–458 (1932) DOI: 10.1098/rspa.1932.0044.

[89] L. Berger, "Influence of spin-orbit interaction on the transport processes in ferromagnetic nickel alloys, in the presence of a degeneracy of the 3d band", Physica **30**, 1141–1159 (1964) DOI: 10.1016/0031-8914(64)90105-3.

[90] M. Yang, K. Cai, H. Ju, K. W. Edmonds, G. Yang, S. Liu, B. Li, B. Zhang, Y. Sheng, S. Wang, Y. Ji, and K. Wang, "Spin-orbit torque in Pt/CoNiCo/Pt symmetric devices", Sci. Rep. **6**, 20778 (2016) DOI: 10.1038/srep20778.

[91] C. O. Avci, K. Garello, C. Nistor, S. Godey, B. Ballesteros, A. Mugarza, A. Barla, M. Valvidares, E. Pellegrin, A. Ghosh, I. M. Miron, O. Boulle, S. Auffret, G. Gaudin, and P. Gambardella, "Fieldlike and antidamping spin-orbit torques in as-grown and annealed Ta/CoFeB/MgO layers", Phys. Rev. B **89**, 214419 (2014) DOI: 10.1103/PhysRevB.89.214419.

[92] C. Stamm, C. Murer, M. Berritta, J. Feng, M. Gabureac, P. M. Oppeneer, and P. Gambardella, "Magneto-Optical Detection of the Spin Hall Effect in Pt and W Thin Films", Phys. Rev. Lett. **119**, 087203 (2017) DOI: 10.1103/PhysRevLett.119.087203.

[93] S. Zhang, "Spin Hall Effect in the Presence of Spin Diffusion", Phys. Rev. Lett. **85**, 393–396 (2000) DOI: 10.1103/PhysRevLett.85.393.

[94] H. L. Wang, C. H. Du, Y. Pu, R. Adur, P. C. Hammel, and F. Y. Yang, "Scaling of Spin Hall Angle in 3d, 4d, and 5d Metals from $Y_3Fe_5O_{12}$ Metal Spin Pumping", Phys. Rev. Lett. **112**, 197201 (2014) DOI: 10.1103/PhysRevLett.112.197201.

[95] P. Hohenberg and W. Kohn, "Inhomogeneous Electron Gas", Phys. Rev. **136**, B864–B871 (1964) DOI: 10.1103/PhysRev.136.B864.

[96] G. Czycholl, *Theoretische Festkörperphysik. Band 1: Grundlagen: Phononen und Elektronen in Kristallen*, Fourth Edition (Springer Spektrum, Berlin Heidelberg, 2016).

[97] S. H. Vosko, L. Wilk, and M. Nusair, "Accurate spin-dependent electron liquid correlation energies for local spin density calculations: a critical analysis", Can. J. Phys. **58**, 1200–1211 (1980) DOI: 10.1139/p80-159.

[98] J. P. Perdew, K. Burke, and M. Ernzerhof, "Generalized Gradient Approximation Made Simple", Phys. Rev. Lett. **77**, 3865–3868 (1996) DOI: 10.1103/PhysRevLett.77.3865.

[99] L. Hedin, "New Method for Calculating the One-Particle Green's Function with Application to the Electron-Gas Problem", Phys. Rev. **139**, A796–A823 (1965) DOI: 10.1103/PhysRev.139.A796.

[100] C. G. Broyden, "A Class of Methods for Solving Nonlinear Simultaneous Equations", Math. Comp. **19**, 577–593 (1965) DOI: 10.1090/S0025-5718-1965-0198670-6.

[101] C. G. Broyden, "Quasi-Newton Methods and their Application to Function Minimisation", Math. Comp. **21**, 368–381 (1967) DOI: 10.1090/S0025-5718-1967-0224273-2.

[102] D. G. Anderson, "Iterative Procedures for Nonlinear Integral Equations", J. ACM **12**, 547–560 (1965) DOI: 10.1145/321296.321305.

[103] I. Mertig, E. Mrosan, and P. Ziesche, *Multiple Scattering Theory of Point Defects in Metals: Electronic Properties*, First Edition (Teubner, Leipzig, 1987).

[104] C. Heiliger, "Elektronentransport durch planare Tunnelkontakte: Eine ab initio Beschreibung", PhD thesis (Martin-Luther-Universität Halle-Wittenberg, 2007).

[105] J. Zabloudil, ed., *Electron scattering in solid matter: a theoretical and computational treatise*, Springer Series in Solid-State Sciences 147 (Springer, Berlin ; New York, 2005).

[106] B. H. Drittler, "KKR-Greensche Funktionsmethode für das volle Zellpotential", Berichte des Forschungszentrums Jülich (1991).

[107] R. Zeller, P. Lang, B. Drittler, and P. Dederichs, "A Full-Potential KKR-Green's Function Method to Calculate the Electronic Structure of Surfaces", MRS Proc. **253**, 357 (1991) DOI: 10.1557/PROC-253-357.

[108] M. Czerner, "Beiträge zur Theorie des Elektronentransports in Systemen mit nichtkollinearer magnetischer Ordnung", PhD thesis (Martin-Luther-Universität Halle-Wittenberg, 2009).

[109] J. Binder, "Giant Magnetoresistance - eine ab-initio Beschreibung", PhD thesis (Technische Universität Dresden, 2000).

[110] P. Zahn, "Screened Korringa-Kohn-Rostoker Methode für Vielfachschichten", PhD thesis (1998).

[111] H. Ebert, "NMR-Untersuchungen zur elektronischen Struktur metallischer Systeme – Theorie und Experiment", PhD thesis (Ludwig-Maximilian-Universität München, 1985).

[112] R. Zeller, P. H. Dederichs, B. Újfalussy, L. Szunyogh, and P. Weinberger, "Theory and convergence properties of the screened Korringa-Kohn-Rostoker method", Physical Review B **52**, 8807–8812 (1995) DOI: 10.1103/PhysRevB.52.8807.

[113] U. von Barth and L. Hedin, "A local exchange-correlation potential for the spin polarized case: I", J. Phys. C: Solid State Phys. **5**, 1629–1642 (1972) DOI: 10.1088/0022-3719/5/13/012.

[114] R. Niu and W. K. Zhu, "Materials and possible mechanisms of extremely large magnetoresistance: a review", J. Phys.: Condens. Matter **34**, 113001 (2022) DOI: 10.1088/1361-648X/ac3b24.

[115] M. Walter, J. Walowski, V. Zbarsky, M. Münzenberg, M. Schäfers, D. Ebke, G. Reiss, A. Thomas, P. Peretzki, M. Seibt, J. S. Moodera, M. Czerner, M. Bachmann, and C. Heiliger, "Seebeck effect in magnetic tunnel junctions", Nature Materials **10**, 742–746 (2011) DOI: 10.1038/nmat3076.

[116] C. Heiliger and M. D. Stiles, "Ab Initio Studies of the Spin-Transfer Torque in Magnetic Tunnel Junctions", Phys. Rev. Lett. **100**, DOI: 10.1103/PhysRevLett.100.186805 (2008) DOI: 10.1103/PhysRevLett.100.186805.

[117] G. P. Kerker, "Efficient iteration scheme for self-consistent pseudopotential calculations", Phys. Rev. B **23**, 3082–3084 (1981) DOI: 10.1103/PhysRevB.23.3082.

[118] M. Manninen, R. Nieminen, P. Hautojärvi, and J. Arponen, "Electrons and positrons in metal vacancies", Phys. Rev. B **12**, 4012–4022 (1975) DOI: 10.1103/PhysRevB.12.4012.

# List of Own Publications

[A1]  A. Fabian, M. T. Elm, D. M. Hofmann, and P. J. Klar, "Hierarchical structures of magnetic nanoparticles for controlling magnetic interactions on three different length scales", J. Appl. Phys. **121**, 224303 (2017) DOI: 10.1063/1.4983849.

[A2]  A. Fabian, M. Czerner, C. Heiliger, M. T. Elm, D. M. Hofmann, and P. J. Klar, "Domain formation in rectangular magnetic nanoparticle assemblies", Phys. Rev. B **98**, 054401 (2018) DOI: 10.1103/PhysRevB.98.054401.

[A3]  N. Neugebauer, A. Fabian, M. T. Elm, D. M. Hofmann, M. Czerner, C. Heiliger, and P. J. Klar, "Investigation of the dipole interaction in and between ordered arrangements of magnetic nanoparticles", Phys. Rev. B **101**, 104409 (2020) DOI: 10.1103/PhysRevB.101.104409.

[A4]  A. Fabian, M. Czerner, C. Heiliger, H. Rossignol, M.-H. Wu, and M. Gradhand, "Spin accumulation from nonequilibrium first principles methods", Phys. Rev. B **104**, 054402 (2021) DOI: 10.1103/PhysRevB.104.054402.

[A5]  M.-H. Wu, A. Fabian, and M. Gradhand, "Spin accumulation in metallic thin films induced by electronic impurity scattering", Phys. Rev. B **104**, 184421 (2021) DOI: 10.1103/PhysRevB.104.184421.

[A6]  A. Fabian, M. Gradhand, M. Czerner, and C. Heiliger, "First-principles scattering with Büttiker probes: The role of self-energies", Phys. Rev. B **105**, 165106 (2022) DOI: 10.1103/PhysRevB.105.165106.

# Acknowledgements

# Eidesstattliche Erklärung

Gemäß § 17, Absatz 2, Punkt 2 der Promotionsordnung der Naturwissenschaftlichen Fachbereiche der Justus-Liebig-Universität Gießen in der Fassung vom 21.01.2016

Ich erkläre: Ich habe die vorgelegte Dissertation selbstständig und ohne unerlaubte fremde Hilfe und nur mit den Hilfen angefertigt, die ich in der Dissertation angegeben habe. Alle Textstellen, die wörtlich oder sinngemäß aus veröffentlichten Schriften entnommen sind, und alle Angaben, die auf mündlichen Auskünften beruhen, sind als solche kenntlich gemacht. Ich stimme einer evtl. Überprüfung meiner Dissertation durch eine Antiplagiat-Software zu. Bei den von mir durchgeführten und in der Dissertation erwähnten Untersuchungen habe ich die Grundsätze guter wissenschaftlicher Praxis, wie sie in der „Satzung der Justus-Liebig-Universität Gießen zur Sicherung guter wissenschaftlicher Praxis" niedergelegt sind, eingehalten.

I declare that I have completed this dissertation single-handedly without the unauthorized help of a second party and only with the assistance acknowledged therein. I have appropriately acknowledged and cited all text passages that are derived verbatim from or are based on the content of published work of others, and all information relating to verbal communications. I consent to the use of an anti-plagiarism software to check my thesis. I have abided by the principles of good scientific conduct laid down in the charter of the Justus Liebig University Giessen „Satzung der Justus-Liebig-Universität Gießen zur Sicherung guter wissenschaftlicher Praxis" in carrying out the investigations described in the dissertation.

Giessen, den _____

_____

Alexander Fabian